Black-body radiation induced correlated excitation of Potassium Rydberg atoms in tweezer arrays

Lorenzo Festa

München 2021

Black-body radiation induced correlated excitation of Potassium Rydberg atoms in tweezer arrays

Lorenzo Festa

Dissertation
an der Fakultät für Physik
der Ludwig–Maximilians–Universität
München

vorgelegt von
Lorenzo Festa
geboren in Desenzano del Garda

München, 20.12.2021

Zusammenfassung

Im Rahmen dieser Arbeit stellen wir die Realisierung einer neuartigen Plattform zur Quantensimulation mit Kaliumatomen in optischen Pinzetten vor. Wechselwirkungen zwischen den Atomen werden durch die Verwendung von Zuständen mit großen Hauptquantenzahlen, auch bekannt als Rydberg-Zustände, erzeugt. Atome, die zu Rydberg-Zuständen angeregt werden, interagieren durch Dipol-Dipol- oder van-der-Waals-Wechselwirkungen, für die eine große Reichweite charakteristisch ist. Die Wechselwirkung führt zu starken Energieverschiebungen bei typischen Abständen zwischen den gefangenen Atomen.

Wir haben das Experiment für die Erzeugung von Wechselwirkungen durch Off-Resonanz-Dressing eines Rydberg-Zustands geplant. Durch verstimmte Dressing-Wechselwirkung bleibt der Langstreckencharakter des gekoppelten Rydberg-Zustands erhalten. Ein Vorteil von Kalium ist seine Grundzustandsaufspaltung, die eine technisch unkomplizierte Beeinflussung beider Grundzustände ermöglicht, so dass Wechselwirkungen erzeugt werden können, die bisher mit Rydberg-Zuständen nicht realisiert wurden. In dieser Arbeit wird eine Methode zur Erzeugung optischer Pinzetten durch eine holographische Technik vorgestellt und wie man sie mit einzelnen Kaliumatomen präpariert. Die besondere Kombination von Kalium mit 1064 nm-Licht erforderte die Anwendung spezifischer Techniken für die Präparation und Abbildung einzelner Atome. Die Raman-Seitenband-Kühlung wird eingesetzt, um Einschränkungen aufgrund von Inhomogenitäten der Lichtverschiebung zwischen den Fallen abzumildern. Das deterministische Laden einzelner Atome in die optischen Pinzetten hat sich im Falle von 1064 nm-Licht als schwierig erwiesen und erforderte die Verwendung von anderem Fallenlicht.

Ein Einzelphotonenschema wird verwendet, um direkt an Rydberg-Zustände bei einer Wellenlänge von 286 nm zu koppeln. Dabei wird das UV-Licht dazu verwendet, Atome die in einer eindimensionalen Kette angeordnet sind, durch Rydberg Dressing anzuregen und somit durch die Wechselwirkungsverschiebung Korrelationen zu generieren.

Das System ermöglichte die mikroskopische Untersuchung von Avalanche-Verlusten, die experimentell bei der Realisierung des Rydberg-Dressings beobachtet wurden. Die Ursache für diese Verluste wurde auf das Vorhandensein von Verunreinigungen zurückgeführt, in diesem Fall Rydberg-Atome die durch Schwarkörperstrahlung erzeugt wurden und entgegengesetzte Parität zu den durch das UV gekoppelten Atomen besitzen. Solche Verunreinigungen erleichtern die direkte Anregung der Atome aufgrund von Verschiebungen der Dipol-Dipol-Wechselwirkung, wodurch die Lebensdauer des angezogenen Zustands verringert wird. Derselbe Effekt ist in unserem System zu beobachten, wenn die Atome verstimmt an einen Rydberg-Zustand gekoppelt sind. Durch die Möglichkeit Verluste an einzelnen Atomen zu messen, ist es Möglich Paarkorrelationen zu verwenden, um die Erleichterung der Verluste zu bestätigen und die typische Reichweite dazu zu identifizieren. Wir bestätigen die Dipol-Dipol-Skalierung der Erleichterung, die von den durch die Schwarzkörperstrahlung gekoppelten Zuständen erzeugt wird. Wir können auch die Auswirkung der Bewegung der Rydberg-Atome auf diesen Prozess in unserem System identifizieren. Darüber hinaus wird die Signatur des Avalanche-Verlustes bei der Auswertung von Korrelationen höherer Ordnung beobachtet.

Zusammenfassend stellt diese Arbeit eine neue Plattform für die Quantensimulation mit Kaliumatomen in optischen Pinzetten vor. Wir identifizieren die Ursache für einen begrenzenden Faktor der Rydberg-Dressing-Technik bei Raumtemperatur. Wir schlagen Ideen vor, um dieses Problem entweder dynamisch zu lösen, indem wir die Bewegung des Atoms aus der Atomebene heraus erzwingen, oder indem wir die Verunreinigungen durch optisches Pumpen entfernen.

Abstract

In the framework of this thesis, we introduce the realization of a novel platform for quantum simulation with Potassium atoms in optical tweezers. Interactions between the atoms are created by using states with large principal quantum numbers, also known as Rydberg states. Atoms excited to Rydberg states interact through dipole-dipole or van-der-Waals interactions, which have a long range character. The interaction produces strong energy shifts at typical distances between the trapped atoms. We planned the experiment for the generation of interactions through off-resonant dressing of a Rydberg state. The off-resonant dressing conserves the long-range character of the coupled Rydberg state. An advantage of Potassium is its ground state splitting that allows for a technically uncomplicated dressing of both ground states with the capability to engineer interactions not realized before with Rydberg states.

This thesis presents a method to generate optical tweezers through a holographic technique and how to prepare them with single Potassium atoms. The particular combination of Potassium with 1064 nm light required the application of specific techniques for the preparation and imaging of single atoms. Raman sideband cooling is implemented to mitigate limitations from light shifts inhomogeneities between the traps. The deterministic loading of single atoms into the optical tweezers had been proven difficult in the case of 1064 nm light and required the use of different trapping light.

A single-photon scheme is used to directly couple to Rydberg states at a wavelength of 286 nm. The UV light allows us to off-resonantly dress atoms prepared in a one-dimensional chain and the generation of quantum correlations between the atoms thanks to the created interaction shift.

The system enabled the microscopic study of avalanche losses that have been experimentally seen during the realization of Rydberg dressing. The cause of such losses was attributed to the presence of impurities, Rydberg atoms with opposite parity to the coupled by UV light, generated by black-body radiation. Such impurities facilitate the direct excitation of atoms due to dipole-dipole interaction shifts, reducing the dressed state lifetime. This same effect can be seen in our system when the atoms are off-resonantly coupled to a Rydberg state. The capacity to identify single atomic losses allows us to use a two-body correlation to confirm the facilitation character of the loss event and to measure the typical facilitation range. We confirm the dipole-dipole scaling of the facilitation generated by the states coupled by black-body radiation. We can also identify the effect of the Rydberg atom motion on the facilitation process in our system. Furthermore, the signature of the avalanche loss is observed with the evaluation of higher-order correlations.

In summary, this thesis presents a new platform for quantum simulation with Potassium atoms in optical tweezers. We identify the cause of one limiting factor of the Rydberg dressing technique at room temperature. We propose ideas to solve this problem either dynamically, forcing the movement of the atom out of the atomic plane, or by removing the impurities through optical pumping.

Contents

To Dalila

To Dalila

Chapter 1

Introduction

The field of cold atoms has significantly expanded from its inception when the first techniques for slowing and cooling atoms were demonstrated [1, 2]. Over the following decades. The continuous development of atom trapping and cooling techniques led to a milestone achievement: the observation of a Bose-Einstein condensate [3, 4], a theoretically predicted state of matter, using bosonic atoms. This result was possible with the help of techniques, such as evaporative cooling, that allowed reaching record low temperatures. The realization of a degenerate Fermi gas using fermionic atoms followed shortly after [5]. These results allowed for the direct observation of microscopical quantum mechanical effects thanks to the magnification of the quantum mechanical behavior of ultracold atoms [6–10].

Further trapping and manipulation techniques have been developed over the years, enabling the study of new physically rich systems. One of these techniques uses laser light to generate optical lattices for trapping atoms allowing observation of both the superfluid and Mott insulator phases [11]. The new technique expanded the scope of investigations in quantum mechanics with cold atoms and stimulated new metrology techniques, which redefined the frequency standard [12]. Today the combination of ultracold atoms in optical lattices is pushing forward the previously reached measurement limits for atomic clocks [13, 14], making ultra-cold atoms, together with trapped ions, the most precise frequency reference in the world.

In recent years the development of microscopy techniques for imaging atoms in optical lattices opened a new approach to the study of quantum mechanical many-body systems [15–19]. The high optical resolution enabled unprecedented precise manipulation and detection of single atoms in optical lattices. Moreover, the control and accessible time scales make these systems suitable for the simulation of solid-state systems and the engineering of Hamiltonians.

Experiments based on arrays of tightly focused optical traps called optical tweezers to increase in number within the cold atoms community. The advantage in such experimental design is the easy, and fast preparation of single atoms in the traps [20] with a significant reduction of the experiment's duty cycle compared to ultracold atoms ones. The stochastic preparation of single atoms with a probability of 50% was the limiting factor of this technique and was used only for small systems [21, 22]. A turning point came with the introduction of sorting techniques that allow the movement of single or multiple atoms to produce a unitary filled array without defects in a fraction of a second [23–26]. With holographic techniques, it is possible to generate arrays of optical tweezers that can be arranged in arbitrary one-, two- or three-dimensional geometries [27–29].

Optical tweezers can be used for metrological purposes [30–32] to improve the

interrogation duty cycle of atomic clocks.

In optical lattices, one controls the interaction through the tuning of the tunneling between the lattice sites. With optical tweezers, tunneling is much more challenging to realize in the case of a large system. Experiments have demonstrated atoms tunneling between tweezers only in small systems composed of few traps [21, 22, 33, 34] or in combination with an optical lattice [35]. However, interactions between trapped atoms have been created by exploiting the longrage interactions between Rydberg states[36]. Atoms excited to a Rydberg state have large dipole moments that create strong, and long-range interactions [37]. With the appropriate choice of the Rydberg state, the length of such interactions can be of the same length scale as the spacing between the atoms in the tweezer array.

Moreover, physicists have developed several methods to use such interactions [38–40] and have used them to map interesting physics problems such as spin systems [41–45] and the study of topological ordering [46]. In recent years, the high fidelity control over Rydberg excitation and interaction of atoms combined with optical tweezers have made them a good candidate for quantum computing platforms [47–55].

The scheme that interests us the most in our work is called Rydberg dressing. In this approach, a Rydberg state is off-resonantly coupled to a ground state, transferring part of the Rydberg character to the ground state atoms. The admixture allows for long range interactions between the ground state atoms without direct excitation to Rydberg states. This technique allowed for complete control over the generated interaction and the implementation of Hamiltonian engineering [56, 57], the realization of Ising quantum magnets [58–60], and quantum gates [61].

This work continues the description of a new experiment with Potassium39 atoms trapped in optical tweezers from the thesis of Nikolaus Lorenz [62]. Ours is the first experiment realizing the trapping of ultracold Potassium39 atoms in optical tweezers. We designed the experiment for the use of the Rydberg dressing technique for the engineering of long-range interactions. The choice of the atomic species fell onto Potassium due to its accessible laser transitions, proven cooling techniques, and a relatively small hyperfine ground state energy splitting. This feature allows easy implementation of a novel Rydberg dressing scheme called double dressing [63], where we couple two ground states simultaneously to two different Rydberg states.

In this work, we also investigate the uncontrolled decoherence effect that limits the Rydberg dressing technique. Such effect is due to a facilitated excitation mechanism to Rydberg triggered by the combination of off-resonantly excited Rydberg atoms and black-body radiation transfer to opposite parity states.

Outline

The structure of the thesis is the following:

Chapter 2 gives an overview of the experimental apparatus designed and built during the work of this thesis. First, we describe the vacuum system. The details regarding the imaging system follow, with particular attention to the in-vacuum objective. We use the same objective to generate the optical arrays of traps or tweezers in our experiments. The beams' setup and the techniques for the laser cooling are described, showing their arrangement around the vacuum chamber. At last, we describe the system for the generation of UV light and show the optical setup that coveys the UV light to the atoms. We also explain the characterization method for the Rydberg spectroscopy and the coupling to the state that we use in our experiments.

In Chapter 3 we focus on the generation and characterization of the optical tweezers that we use for our experiments. In Section 3.1 we describe the holography method which generates the optical tweezers. We show the technique that we use for the loading of the atoms into the generated traps in Section 3.2, and we characterize our imaging system and method, which is directly related to the loading method. We characterize the tweezers that we generate with measurements on the trapped atoms in Section 3.3 . We also characterize the occupation lifetime of the atoms in the traps in different configurations. In Section 3.4 we show the results for our attempts to increase the loading probability into the traps, which is limited by photo-association losses. We tried to implement optical shielding from the deleterious photo association to load single atoms with a higher probability deterministically.
Finally, in Section 3.5 a brief description of the methods that we have implemented to perform the experiments described in this thesis is given. They entail the preparation of the atoms in a defined state and the driving ground states transition to create superpositions of states, together with the implementation of Raman sideband cooling of the trapped atoms.

In Chapter 4 we describe the interaction schemes that we can produce using Rydberg states together with our investigation of the fast decoherence channel that affects off-resonant coupling to Rydberg states. In Section 4.1 an intuitive view is given about interactions between Rydberg atoms, explaining the different distance dependency provided the parity of the involved Rydberg states. Then we describe the methods that use these interactions. In Section 4.2 we show our first attempt to realize interactions with Rydberg dressing in our system. Finally, in Section 4.3, we report about the black-body induced facilitation mechanism that hinders the coherence of off-resonant coupled Rydberg states, which is critical in the event of interactions generated with the Rydberg dressing technique.

List of publications

The following articles have appeared in the context of this thesis:

Raman Sideband Cooling in Optical Tweezer Arrays for Rydberg Dressing
Nikolaus Lorenz, Lorenzo Festa, Lea-Marina Steinert, Christian Gross
SciPost Phys. 10, 052 (2021)

Black-body radiation induced facilitated excitation of Rydberg atoms in optical tweezers
Lorenzo Festa, Nikolaus Lorenz, Lea-Marina Steinert, Zaijun Chen, Philip Osterholz, Robin Eberhard, Christian Gross
arxiv:2103.14383 (2021)

Part I

Experimental apparatus

Chapter 2

Experimental apparatus

This chapter gives an overview of the experimental apparatus built during the doctoral studies and used for the experiments reported in this thesis. We give a brief description of the vacuum chamber and its characteristics. We focus on the primary imaging system that we use in the experiments, but a more detailed analysis will follow in Section 3.2.3. We briefly mention the laser cooling techniques that we use in the experiments summarized in this thesis. Lastly, we provide a brief description of the generation and handling of the UV light that is necessary for our experiments with Rydberg states.

Full details regarding the laser cooling systems and the design and characterization for the generation of the UV light can be found in the thesis of Marcel Duda [64], Anne-Sophie Walter [65], and Nikolaus Lorenz [62].

2.1 Vacuum chamber

In this section, we are going to describe the built vacuum setup. The experiment with Potassium in the Zwierlein group carried out at MIT [66] inspired the design of our vacuum chamber. The idea was to avoid any transport of the atoms and to perform all the laser cooling, and the experiments in a single chamber. This design allows for a fast duty cycle of the experimental sequence, $\approx 1\,\mathrm{Hz}$, an order of magnitude faster compared to state-of-the-art quantum gas experiments.

2.1.1 Oven section

The oven section is composed of two chambers, as shown in Fig. 2.1. The first chamber presents several elements connected to it: the Potassium oven, an ion pump, and a cold finger made up of a copper shield. The high vapor pressure of Potassium at room temperature and above $> 10^{-8}\,\mathrm{mbar}$ [67] makes necessary to have good differential pumping to ensure a pressure in the main chamber of $< 10^{-11}\,\mathrm{mbar}$. For this reason, we have an intermediate chamber between the main chamber and the one with the Potassium oven. A differential pumping tube and a vacuum valve connect the chambers. The second chamber has connected another ion pump and a mechanical atomic shutter, it is connected to Zeeman slower by a second differential pumping stage and another valve.

A nozzle with a diameter of 3 mm allows a flux of Potassium atoms to come out from the oven. We heat the oven at a temperature of $\approx 80\,^{\circ}\mathrm{C}$, above the melting point of Potassium, and the nozzle at $\approx 90\,^{\circ}\mathrm{C}$, in order to avoid it clogging.

We have installed an ion pump to keep the pressure low. Due to many reports

of ion-pump failure because of high background vapor pressure from Potassium atoms, several actions similar to the ones reported in the reference [66] were implemented. The ion pump is not placed in a direct line of sight to the pumping filaments from the connection flange. A baffle is placed in the conical connection tube between the chamber and the ion pump to block the pump's direct line of sight.

A double copper shield is located in the middle of the chamber, which also has two holes with a diameter of 3 mm along the atomic path. We cool down the whole shield to $-5\,°C$. A high-current copper feed-through permits the cooling and mounting of it, creating a thermal connection to the outside of the vacuum chamber. We use water-cooled Peltier elements attached to the room side of the feed-through to cool it continuously. The double shield can then capture the atoms that cannot go through the first differential pumping stage, effectively reducing the atomic vapor pressure.

The differential pumping is done by a 65 mm long connection tube, with an inner diameter of 3 mm.

After the differential pumping tube the passage of the atoms is permitted or stopped by a mechanical shutter. We have built the shutter with a bellow and a long metal rod. The bellow is pushed by a pneumatic piston, tilting the metal rod and freeing the passage for the atoms. This mechanism has been proven more reliable than in vacuum rotational shutters [66, 68]. However, we did not operate the shutter for the experiments written up in this thesis due to their fast duty cycle .

2.1.2 Zeeman slower

After the oven section, there is a spin-flip Zeeman slower. One can load a magneto-optical trap (MOT) directly from atomic background pressure or a 2D MOT. However, both techniques have the disadvantage of increasing the vacuum pressure in the main chamber, reducing the occupation lifetime of trapped atoms and occupying space that we could use for the optics around the chamber. A Zeeman slower overcomes the problems above by providing differential pumping and a substantial flux of atoms to load the MOT with minimal technical complexity.

The Zeeman slower is uncomplicated in design and alignment, requiring a small amount of optical power. Plus, the spin-flip design ensures a non-zero magnetic field at the end, which makes the slowing laser beam off-resonant for the loaded atoms in the MOT. A detailed description of our Zeeman slower can be found in the thesis of Marcel Duda [64]. The atoms emerge from the oven at a speed of 450 m/s. The field generated by the slower is the largest at the beginning with an amplitude of 320 G, and with a laser detuning of 205 MHz one obtains a capture velocity of ≈ 350 m/s.

We built the Zeeman slower of a hollow rectangular copper tube wound around a non-magnetic stainless steel tube in several layers. All the layers are electrically connected to form a single-coil, and we power them with one power supply.

In the everyday operation of the experiment, we do not use the spin-flip part of the slower. The tail of the magnetic field generated to produce the magneto-optical trap is enough to act as the spin-flip part of the slower.
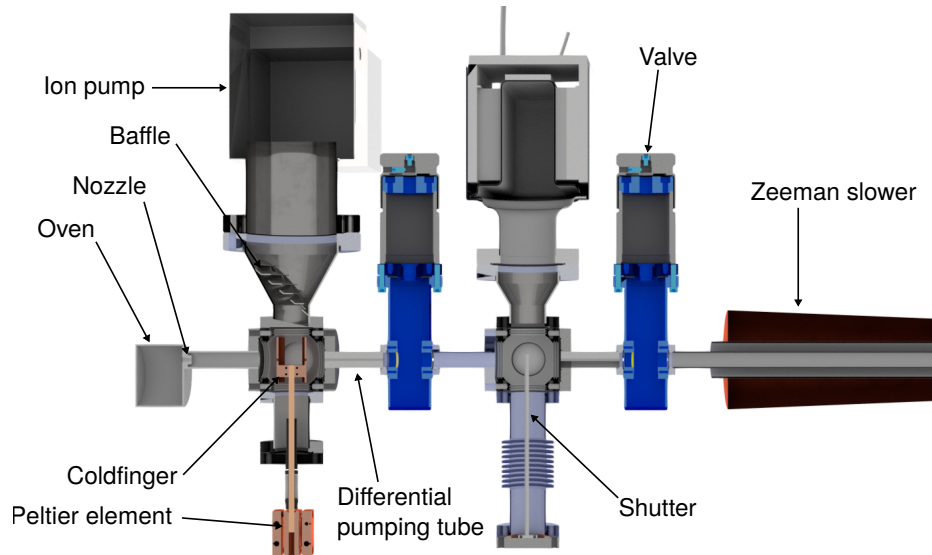
Figure 2.1: Oven section. On the left, the oven is attached to the first chamber. A cold finger composed of a cooled copper shield helps to contain the vapor pressure of Potassium by capturing free-flying atoms, which do not go through the first differential pumping tube. A baffle block is employed to reduce the probability that Potassium atoms reach and damage the ion pump by blocking the direct line of sight with the chamber. A differential pumping tube connects to the second chamber. The second chamber contains a mechanic shutter to stop the atomic flux to the main chamber. A second differential pumping tube connects to the Zeeman slower tube. In-line valves can separate the three parts of our vacuum system in the eventuality of maintenance procedures. Figure from [62].

2.1.3   Main chamber

The main chamber is the core of the experiment and presents many elements directly mounted inside the vacuum, as shown in Fig. 2.2. The choice of using a metal chamber comes from the idea of keeping any possible dielectric surface, which can present patch charges at a significant distance from the atoms. The distance is essential in the case of experiments with Rydberg atoms which are very sensitive to electric fields. Electric fields that change uncontrollably over time are detrimental to the successful realization of experiments.

We have connected using a CF63 flange a pumping chamber next to the Zeeman slower, which arrives with a $\approx 45°$ angle to the main chamber. We have mounted both a titanium sublimation pump onto a CF100 flange and an ion pump onto a CF63 flange on the tube coming from the main chamber in a vertical position.

The high-resolution objective, the high-current coils, and the electrodes are mounted in-vacuum. Also, two small RF antennas and an ion detector are present inside the chamber, for future experiments.

The chamber has 6 CF63 view-ports, two for each main axis. Four CF40 view-ports are also present in the x-z-plane at $45°$ angles with respect to the x-y-plane. All the aforementioned view-ports are anti-reflection coated between 285 nm to

290 nm for single Rydberg transitions, 405 nm and 980 nm for the two-photon inverted scheme Rydberg excitation scheme [69], between 750 nm to 775 nm for the Potassium39 cooling light on the D1 and D2 transitions [70–72] and 1064 nm for dipole traps and optical tweezers.
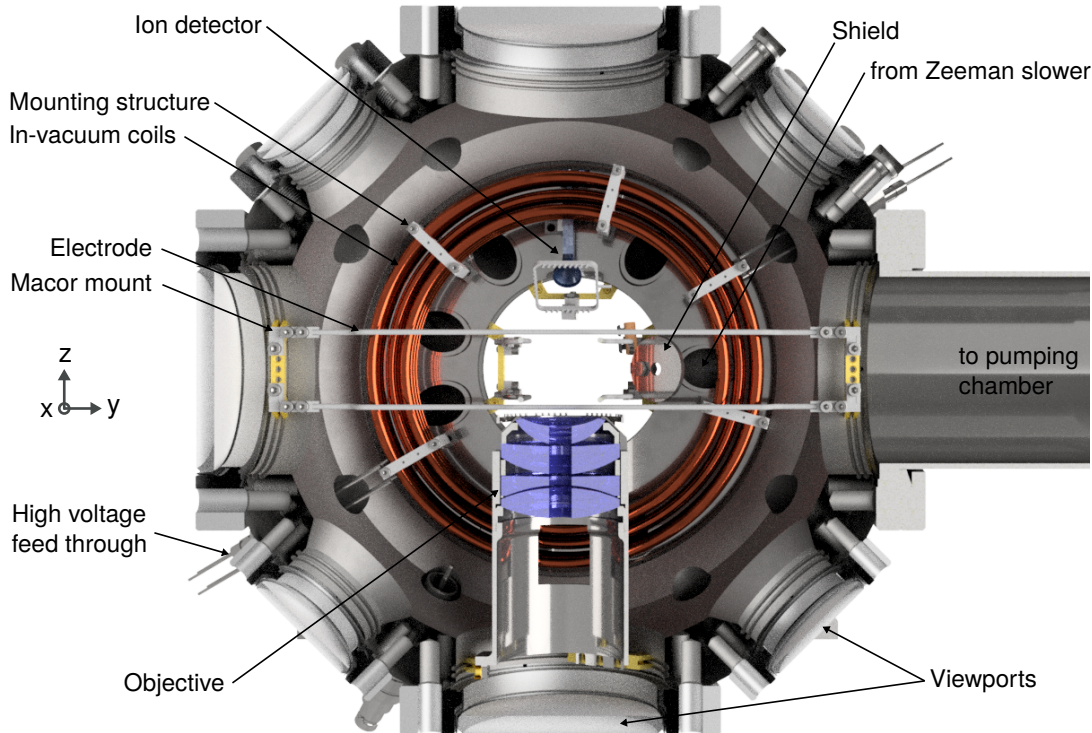
Figure 2.2: Main chamber. Cut through the main chamber, the objective can be seen fixed on the bottom part of the chamber. At the end of the Zeeman slower, a metallic circular shield is visible with a hole to avoid coating the objective. Eight electrodes are present ≈ 2 cm apart and mounted with the groove grabbers of Kimball Physics. The water-cooled in-vacuum coils are mounted onto the two CF160 flanges to produce the magnetic field for the MOT. We have view-ports on all the CF63 and CF40 flanges for optical access, plus 12 CF16 view-ports for additional access from different angles. As shown in the figure, there is also an ion detector mounted in the chamber. We placed a mesh of wires on the objective to shield from possible patch charges present on the coated surface of the objective lens. There is a chamber with ion- and titanium sublimation pumps for the main chamber on the right. Figure from [62].

We use the in-vacuum coils to generate the magnetic field gradient for the MOT. They are in a Helmholtz configuration for the possibility of creating strong magnetic fields by inverting the current flux in one coil.
Even though they are technically more challenging to handle and mount, the coils inside the vacuum have some advantages, especially if one wants to use a metal vacuum chamber. Coils outside the chamber would be much bigger to fulfill the Helmholtz conditions and require more windings or higher currents to produce the same magnetic fields. A high electrical current increases the thermal load produced by the coils. Secondly, we significantly reduce the generation

of eddy currents, and we measure a settling time of 2 ms for a fast current switch from 100 A.

The coils can generate a magnetic field of 215 G with a 200 A current or a gradient of 40 G/cm along the strong axis and 20 G/cm along the weak axis with reversed currents.

The coils are made up of hollow copper tubes to apply water cooling. They are connected outside the chamber using high-voltage hollow copper vacuum feed-throughs. The coils and feed-throughs are soldered together to form a vacuum-tight and electrically conductive connection. The high-voltage feed-throughs are electrically isolated from the chamber by a ceramic connection to the flange.

Compensation coils are mounted on the outside of the main chamber directly onto the CF63 flanges of the view-ports. These are needed to compensate static magnetic fields from the environment or apply a quantization axis during the experiments. At the maximum current of 15 A, they can produce fields up to 22 G. Due to mounting constraints, the coils are not in a Helmholtz configuration, but the inhomogeneity in a 100 μm^3 around the chamber's center is $\approx 1\%$.

Electrodes have been mounted inside the chamber since Rydberg atoms are very sensitive to electric fields. Electrodes are needed to compensate for stray static electric fields or apply definite electric fields. The electrodes are made up of non-magnetic stainless steel rods of 2 mm diameter. We have mounted them with the help of groove grabbers and Macor ceramic mounts for electrical isolation close to the view-ports. We connected the outside of the chamber to the electrodes with copper wires and high voltage feed-throughs. On the outside, we have grounded the electrodes with 50 Ω resistors for the experiments described in this thesis. The calculated electric field inhomogeneity is 2% in a 1 mm^3 region from the position of the atoms.

2.2   Imaging system

The experimental apparatus presents two imaging systems, one for absorption imaging and one for fluorescence imaging. The absorption imaging systems verify the MOT status and position, generally used for testing the system, not for carrying out experiments. We use standard industrial CCD cameras to perform absorption imaging.

2.2.1   In-vacuum objective

Fluorescence imaging is the imaging technique that we use during the experiments. The most important part of the fluorescence imaging system is the in-vacuum objective, which is also used to generate the optical tweezers, as described in Chapter 3. As previously noted and shown in Fig. 2.2, we mounted the objective inside the vacuum chamber. Its numerical aperture is 0.6, with an effective focal length of 33 mm and a working distance measured from the front

surface of the mount of 16.75 mm. Special Optics designed the objective for a diffraction-limited performance at the same working distance for 767 nm and 1064 nm light, as shown in Fig. 2.3, the optical parts have been anti-reflection coated accordingly. The objective has a Strehl ration measured by the manufacturer of 0.69, the ratio measured to reach ideal peak intensity for a diffraction limited spot.

The objective was specifically manufactured to be highly vacuum compatible with the whole mount for the lenses made of non-magnetic stainless steel. The mount also presents openings on the sides and on the top to vent the whole objective and avoid any virtual leak and also allow beams to be shot at $\approx 45°$.
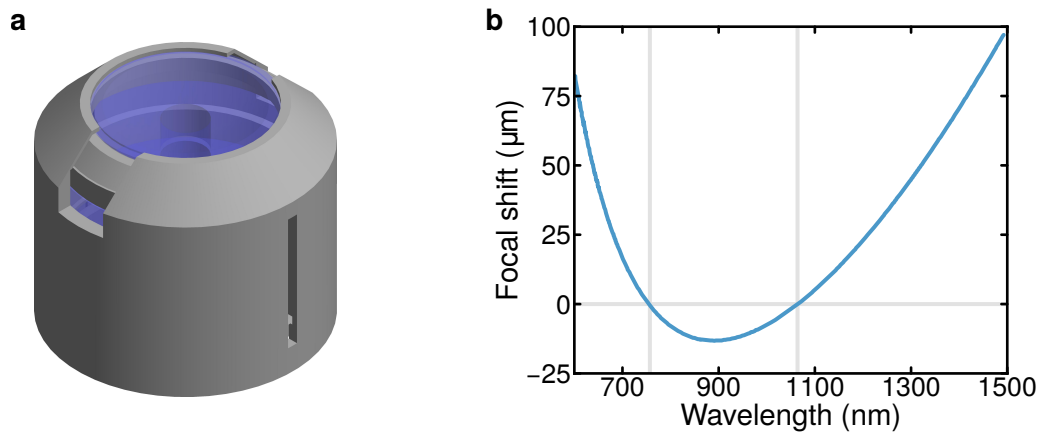

Figure 2.3: In-vacuum objective. In the render of the objective are visible slits on the side for venting the mount and cuts on top for the diagonal passage of laser beams. In the middle a hole that passes through all the optical elements is visible. **Right** Focal point position in function of wavelength. As by design the focal points for 767 nm and 1064 nm light are matched to make easier the generation and the imaging of tweezer traps.

Another feature of our objective is a hole at the center of the objective with 8 mm diameter that passes through all optical elements. We designed the hole to have vertical optical access, and we used it to shoot through the vertical MOT beams. We can also use it to shoot through high-power optical beams to make a dipole trap or a lattice or UV light that can damage the optics at high power.

The hole slightly disturbs the point spread function of a diffraction limited spot, not affecting the imaging resolution. It behaves like a high pass filter in Fourier optics k-space [73] which removes low spatial frequency features that do not affect the resolution of the objective.

Onto the coating of the optical elements of the objective, patch charges can form and create stray electric fields. To prevent uncontrolled electric fields from the surface of the objective facing the atoms we placed a coarse mesh of gold wires on it. The wires forming the mesh have 50 μm diameter, and we wired them on a steel ring that we mounted on top of the objective. A different solution would be to coat the optical element facing the atoms with indium tin oxide (ITO) [74] which is conductive and prevents patch charges formation, with the disadvantage of a reduction of transmission to 90%.
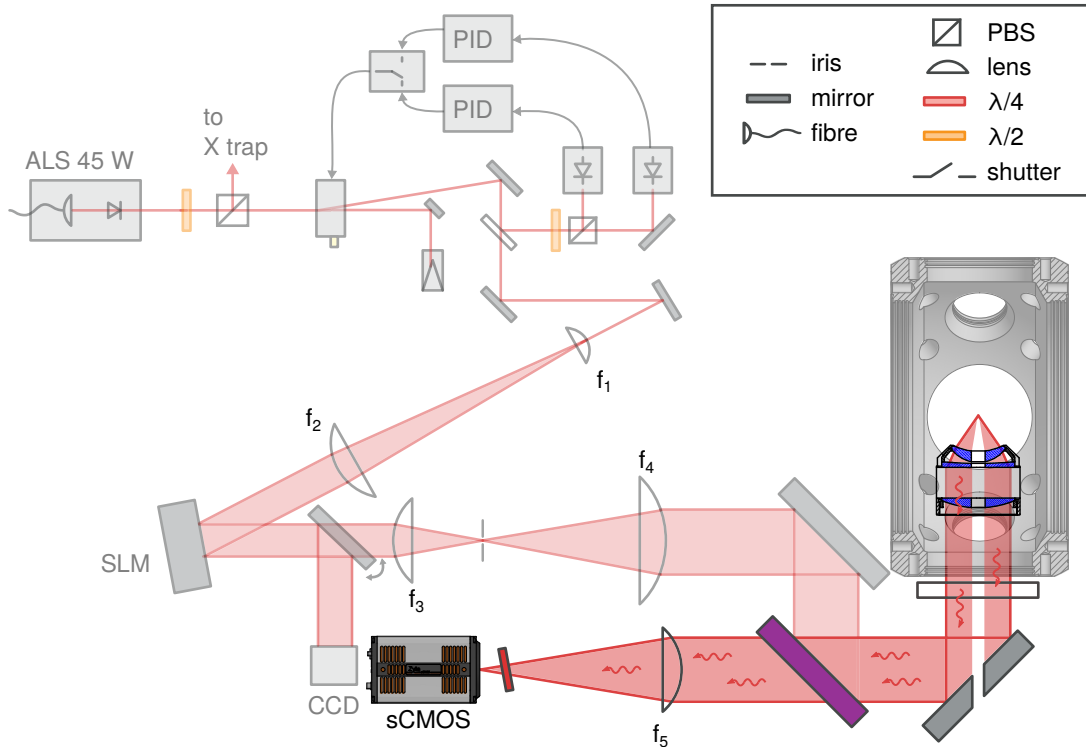
2.2.2 Fluorescence imaging setup

Figure 2.4: Imaging system setup. The collected light from the objective is sent to the imaging camera a Zyla 4.2 sCMOS passing through a dichroic mirror (purple optical element) and is focused on the surface of the camera by a achromatic lens with focal length $f_5 = 250\,mm$. In front of the camera a band pass filter is placed (deep red element) to filter any stray light coming from the trapping light or the environment. Figure adapted from [62].

We show the scheme of the imaging system in Fig. 2.4. The light collected by the objective during one imaging sequence is sent through the view-port of the vacuum chamber, and a mirror with a hole reflects it. The mirror with the hole is coated to be highly reflective between 767 to 770 nm and also 1064 nm to generate the tweezers. The hole in the mirror is to let through the light for the MOT. We placed an inset in the hole of the mirror with a flat round part with a diameter of 13 mm that covers part of the mirror surface. We coated the inset with black nickel to eliminate any light coming from the MOT beams that could reach the camera. We mounted the mirror in a box with two other smaller mirrors. One mirror directs both the cooling and trapping light upwards whereas the other is for UV light, in the event we want to use a beam coming from the bottom of the chamber.

After the mirror, the light passes through a dichroic mirror which is highly reflective for $950 - 1064\,nm$ light and highly transmissive for $670 - 810\,nm$ light. We used the dichroic mirror to superimpose the path of the trapping light and the fluorescence imaging one.

After the dichroic mirror, the light is focused onto the camera, a Zyla 4.2 sCMOS camera produced by Oxford Instruments, through an achromatic lens with a focal length $f_5 = 250\,mm$. The camera and the achromatic lens are mounted on a

blackened aluminum tube to pre-align the camera to the lens. The lens's mount and the tube at its entrance are threaded to regulate the position of the lens. We regulated the lens's position with a reference collimated beam.

Between the lens and the camera chip, we have placed an optical bandpass filter from Semrock, with transmission $> 93\%$ in the 20 nm bandwidth of the filter. The filter is mounted on a lens tube and tilted at a slight angle, enough to avoid any interference effect and let the imaging light pass through.

With the effective focal length of the objective and the focal length of the achromatic lens, we have a magnification of $f_5/f_{obj} \simeq 7.6$ from the position of the atoms. Given the pixel size of 6.5 μm of our camera, we image on one pixel a region of 0.86×0.86 μm in the focal plane of the objective. We chose the magnification value to focus the light scattered by a single tweezer trap, described in Chapter 3 onto a single pixel to maximize the signal to noise ratio.

2.3   Cooling and trapping setup

The optical setup around the chamber for laser cooling will be shown, and we will give some details about the cooling techniques we use during the experiments. we illustrated the level scheme with the indication of the transitions that we use for laser cooling in Fig. 2.5.
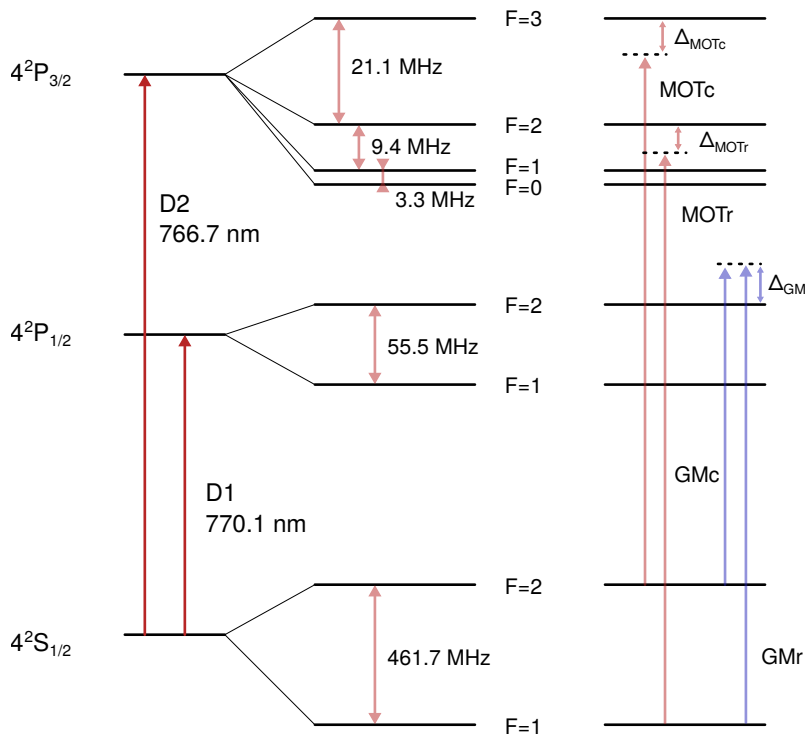

Figure 2.5: Level scheme of Potassium39. Level scheme for the D1 and D2 transitions in Potassium39. Where the red arrows show the MOT cooler and repumper transitions that we use, while the blue arrows show the ones for GM cooling. For the MOT we need 767 nm light, while for the GM we need 770 nm light.

2.3.1 MOT and red molasses cooling

The first cooling stage in our sequence occurs in a magneto-optical trap, which uses light on the D2 transition as shown in Fig. 2.5. We generate a magnetic field gradient with the coils inside the vacuum where laser beams along the main axis enable the laser cooling and the trapping of atoms in a magneto optical trap (MOT) at a temperature of $\approx 1\,\text{mK}$. We load the atoms in the MOT for a few hundreds of milliseconds and we switch off the Zeeman slower magnetic field and laser beam. Follows a compressed MOT stage (cMOT) which further reduces the temperature of the captured atoms down to $\approx 200\,\mu\text{K}$ [72]. The laser light that we call cooling light works on the $4S_{1/2},F = 2$ to $4P_{3/2},F' = 3$ transition, while the repumper light works on the $4S_{1/2},F = 1$ to $4P_{3/2},F' = 2$ transition. We refer the reported detunings for MOT cooler and repumper to these transitions.

On the same transition we perform red molasses cooling [71]. With the red molasses we can cool the atoms below the Doppler limit, reaching a temperature of $\approx 40\,\mu\text{K}$. We use the red molasses technique for the loading and imaging of the atoms in the optical tweezers, we describe the loading technique in Section 3.2. We have a single laser to perform all the cooling techniques on the D2 transition. We stabilize the laser with a modulation transfer spectroscopy technique using a gas cell. We amplify the laser light with a tapered amplifier, and we use two AOMs to bridge the hyperfine splitting of the ground state to provide the cooler and repumper light. Close to the vacuum chamber, the cooler and repumper light overlap involving polarizing beam-splitting cubes and waveplates.

	MOT	cMOT	red molasses
Cooler detuning	-5Γ	-3Γ	-1.5Γ
Cooler intensity (I_{sat})	20	19	6
Repumper detuning	-4Γ	-1.5Γ	0Γ
Repumper intensity (I_{sat})	20	0.4	1

Table 2.1: Experimental parameters for the MOT stage. The detuning of the cooler is referenced to the $4S_{1/2},F = 2$ to $4P_{3/2},F' = 3$ transition, while for the repumper the reference is on the $4S_{1/2},F = 1$ to $4P_{3/2},F' = 2$ transition. Intensity is given per beam in units of the saturation intensity for the D2 transition $I_{sat} = 1.75\,\text{mW}/\text{cm}^2$.

2.3.2 Gray molasses cooling

After the cMOT stage we switch off the magnetic field gradient and we apply gray molasses cooling (GM) [72]. We use the gray molasses technique since it is quite robust against variations in the magnetic field. The magnetic field is not stable due to stray fields generated by the eddy currents induced by the switching. We apply the GM cooling while waiting for the fields to settle. We cannot use the red molasses technique since it is very sensitive to magnetic field variations which compromise the cooling performance.

With gray molasses cooling we can reduce the atoms' temperature to $\approx 30\,\mu\text{K}$, similar to the one reached with the red molasses. The GM cooling operates on

the D1 transition.

In Section 3.4 we will show that we can use gray molasses cooling for loading optical tweezers.

In this case the detunings are references to the $4P_{1/2}, F' = 2$ state, where the cooler light couples from the $4S_{1/2}, F = 2$ grounds state and the repumper light from the $4S_{1/2}, F = 1$ ground state. We keep the cooler and repumper in a Raman configuration with detuning between each other of $\delta = 0$, only the common detuning from the transition Δ_{GM} is changed.

We use a setup similar to the MOT laser to generate the light needed for the gray molasses. However, we do not directly lock the GM laser onto a spectroscopy signal. Instead, we offset lock it to a master laser locked on the D1 transition spectroscopy signal from a glass cell. The offset lock allows to easily change the frequency of the GM laser up to $\approx 1\,\mathrm{GHz}$, limited by the electronics used for the lock.

In the experimental sequence we use a detuning of $\Delta_{GM} = 6\Gamma$ and an intensity of $28\mathrm{I_{sat}}$ for each beam.

2.3.3   Optical setup

Fig. 2.6 illustrates the disposition of the beams around the chamber, where we also define the axis for the experiment. We align the MOT beams along the main axis of the system. The beam along the x-axis is slightly tilted, with an angle of $14.5\,°$. The beam are magnified to a $1/e^2$ diameter of $7\,\mathrm{mm}$ for the x- and y-axis and $3\,\mathrm{mm}$ for the z-axis.

Along the z-axis, the beams pass through the in-vacuum objective. To reduce the amount of scattered light into the imaging path, we used two irises to clip the wings of the beams. We image the irises' apertures to the middle of the mirror with the hole below the chamber.

The light needed for GM cooling is superimposed to the MOT light and injected through the same fibers on the laser table. Since we use the same fibers, the MOT and GM light share the same optical path on the experimental table.

The GM light is also used for state preparation (Section 3.5.1), spectroscopy on the D1 transition (Section 3.3.1) and repumping for Raman sideband cooling (Section 3.5.2). When we apply a state preparation or spectroscopy sequence the shutters shown in Fig. 2.6 are closed to only allow light propagating along the x-axis in one direction.

2.3.4   Dipole trap

We have also built a dipole trap with a single focused beam along the x-axis. We used the trap for characterization measurements, and now it is used as a reference for the alignment of the Raman and UV beams. In order to create the trap, we use $1064\,\mathrm{nm}$ light, which we take from the same laser that we use to make the optical tweezers by splitting off a small fraction of the power, as shown in Fig. 3.2. In this case, we use a shear mode AOM for intensity control and stabilization. The shear mode AOM has smaller bandwidth respect compared to
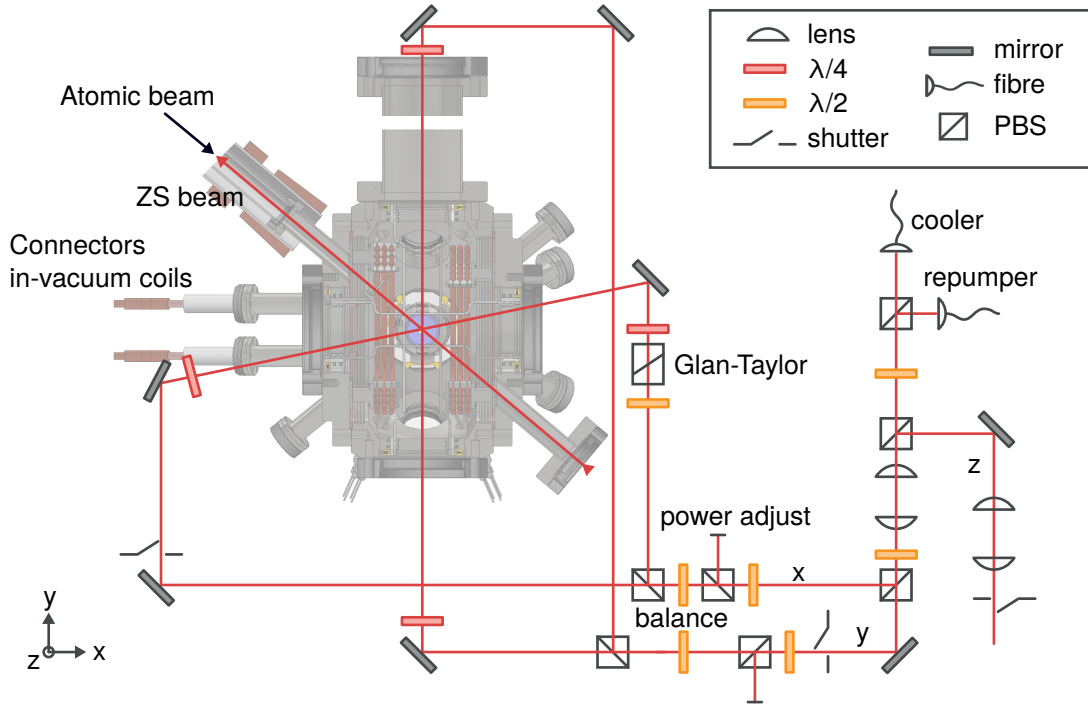
Figure 2.6: Cooling beams disposition. Scheme of the configuration of the beam around the vacuum chamber in the x-y plane. We superimpose both the cooler and the repumper light after the fibers. We divide them into three paths to be used along the axes of the system. For each axis, a power adjustment and balance stage are present. Before entering the chamber, a waveplate adjusts the light polarization to create circularly polarized light. Shutters are present to stop the light along the y- and z-axis while stopping it in only one direction on the x-axis. In the unimpeded direction, a Glan-Taylor polarizer is present for polarization cleaning. Diagonally we show the beam for the Zeeman slower (ZS beam), counter-propagating to the atoms emerging from the oven.

standard AOMs, but it requires low RF power to work, reducing thermal drifts. The beam is imaged in a 4-f configuration from the AOM onto the atoms to reduce drifts further. The trap beam waist at the position of the atoms is of 50 μm, which can produce a trap depth of $\approx 200\,\mu K$ at maximal available power. We load the dipole trap with the application of GM cooling due to its broad working detuning range Δ_{GM} for the GM, cooling atoms outside and inside the trap at the same time.

Apart for alignment and characterization purposes, the dipole trap is also used in this thesis in Section 3.4 to test out deterministic loading for our optical tweezers.

2.4 UV setup

We can follow two paths for the excitation of atoms to Rydberg states a two-photon or a single photon excitation scheme. In our case, we decided to focus on the single photon excitation scheme, which requires a laser in the UV with a

wavelength between 285.5 nm to 288.5 nm, to couple states from $n \approx 20$ to ionization.

We produce the UV light starting with infra-red light and going through two frequency doubling stages. The infra-red seed laser is an external cavity diode laser (ECDL) that works between 1142 nm to 1154 nm. We use a fiber coupled electro-optical modulator (EOM) to create the sidebands at 21.3 MHz for the locking of the laser with the Pound Drever Hall technique. We additionally modulate the light with a frequency between 100 MHz to 700 MHz. We distinguish the sidebands produced by the two modulations calling them small and large sidebands. We stabilize the laser by locking it to a reference cavity made of ultra-low expansion (ULE) glass. The laser is then locked not onto the carrier but to one of the large sidebands. We use the large sidebands to easily tune the laser between the two cavity modes' free spectral range. The large sidebands together with the doubling provide a continuous frequency tuning range up to 2.5 GHz.

The ULE reference cavity is kept under vacuum and is stabilized in temperature to minimize its thermal expansion coefficient. This optimization provides long term stability to the laser with a measured shift of ~ 8.4 kHz/day in the UV.

Before doubling, the seed laser is amplified by a Raman fiber amplifier, which allows reaching powers up to 10 W. The laser then goes through two doubling stages. Each stage is made up of a bow-tie cavity to increase the doubling efficiency. In the first stage, a Lithium Triborate (LBO) crystal is the non-linear medium that produces 575 nm green light from the infrared 1150 nm light.

In the second stage a Cesium Lithium Borate (CLBO) crystal is used to go from the green light 575 nm to the UV light 287 nm. The green light is intensity stabilized before the injection into the doubling cavity.

The first doubling stage is stabilized with a Pound Drever Hall lock using 60 MHz sidebands generated from a resonant EOM before the amplification. We implement a Hänsch-Couillaud lock for the second cavity to avoid using sidebands for the lock. In the case of off-resonant experiments, the modulation applied onto the light to create sidebands can be detrimental, becoming resonant to the transition.

For both cavities, the feedback of the lock is managed by digital FPGA-based PID controllers[1] [75, 76]. The digital controller allows the implementation of an automatic re-lock mechanism for the first doubling cavity if the end of the dynamic range for the feedback is reached. In the case of the second doubling stage, we can lock the cavity only when needed during the experimental sequence to reduce the degradation of the doubling crystal and all the optical elements exposed to UV light.

After the two doubling stages, the UV light follows the path shown in Fig. 2.7. After the last doubling stage, the beam diverges and is collimated and shaped with spherical and cylindrical lenses. We use a single-pass AOM for the intensity control of the light and the generation of fast pulses. We focus the UV beam through a 50 μm pinhole to perform spatial mode cleaning. We use the same

---

[1]Red Pitaya STEMLab 125-14, firmware and interface from Fabian Schmid: https://github.com/schmidf/rp-lockbox
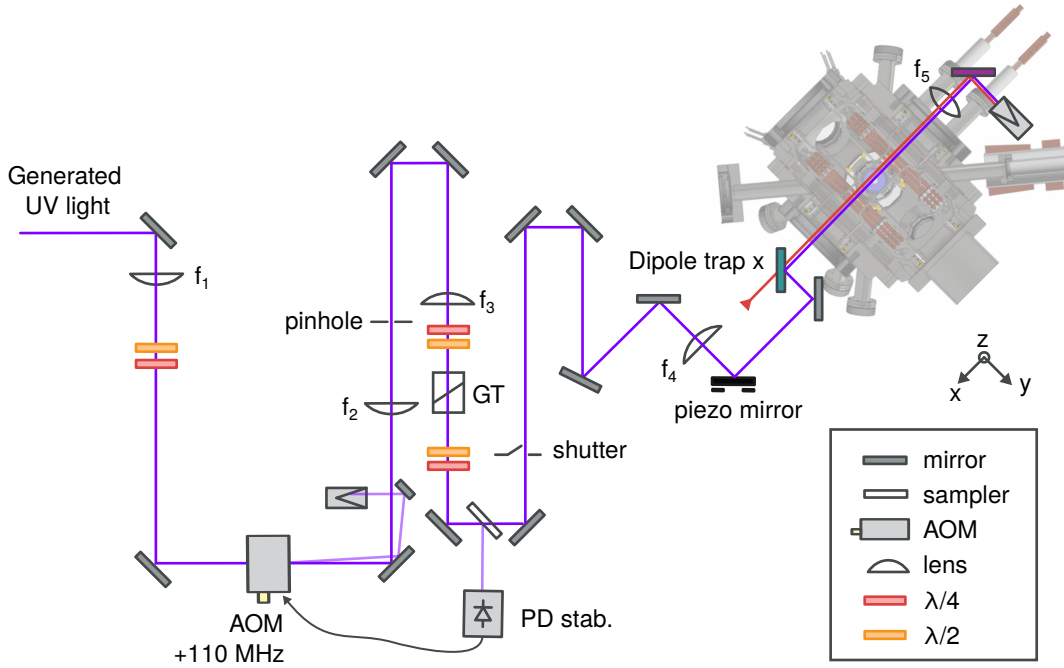
Figure 2.7: Optical setup for the UV light. The divergent beam after the second doubling stage is collimated by f_1. We implement a single-pass AOM for intensity stabilization and pulse production. After the AOM, we focus the beam through a pinhole with lens f_2. We image the pinhole onto the atoms in a 4-f configuration through the lenses f_3 and f_4. We perform polarization cleaning with a Glan Taylor polarizer, where the throughput power is maximized with the waveplates before. We optimize the waveplates after the polarizer to have circular polarization at the atoms' position. A dichroic mirror superimposes the UV light with the imaging light and the light of the dipole trap along the x-axis. Figure adapted from [62].

pinhole as a reference for alignment. The pinhole is imaged and demagnified in a 4-f configuration at the exact position of the atoms, producing a waist of 20 μm. The polarization of the UV light is cleaned with a Glan Taylor polarizer and adjusted to be circular at the position of the atoms. For the precise alignment of the UV beam onto the atoms, a remotely controlled piezo actuated mirror is present close to the vacuum chamber.

In the case of shorter pulses then 20 μs a sample-and-hold stabilization method is used with the AOM, closing the mechanical shutter present after the pin-hole. The setup is planned to have two identical paths and produce two UV beams with a frequency difference of $\sim$ 462 MHz equal to the ground state splitting of Potassium39. The frequency difference is produced using AOMs. This is a simple method to apply Rydberg dressing to both ground states without using a second setup to generate UV light.

We use the dipole trap along the x-axis as a reference for the coarse alignment of the UV light on the atoms. We use a piezo mirror to make the precise alignment of the beam onto the optical tweezers. We use the atomic signal in the tweezers for the alignment.

2.4.1   Rydberg spectroscopy and Rabi frequency calibration

For the measurements reported in Chapter 4 we perform spectroscopy on the Rydberg transition and characterize the coupling by measuring the Rabi frequency at resonance. We perform the measurements with single atoms prepared inside optical tweezers.
We show later in Section 3.5.2 that we can lower the tweezers trap depth to $U = 0.005 \times U_0 = k_B \cdot 3.7\,\mu\text{K}$ from their initial depth U_0, after the application of Raman sideband cooling. We explain how we prepare the atoms in a defined ground state in Section 3.5.1. The sequence comprehends the acquisition of two images, one before and one after the experiment, to identify the lost atoms.

The transition that we want to probe is the one from the $4S_{1/2}, F = 2, m_F = +2$ ground state, and the $62P_{1/2}, m_J = -1/2$ Rydberg state. We apply a magnetic field of $10\,\text{G}$ along the x-axis, parallel to the UV beam, to define the quantization axis and split the m_J levels. The field's orientation makes the polarization of the UV light to be σ^-, driving the desired transition. We illuminate the atoms for $100\,\mu\text{s}$ with a weak UV pulse, and after we measure the number of atoms remaining. We show a result of the measurement in Fig. 2.8 where we can see an absorption line with an FWHM of $112 \pm 9\,\text{kHz}$ averaged over all the optical tweezers used. The natural linewidth that we would expect at room temperature for the Rydberg state is $\Gamma = 2\pi \cdot 1\,\text{kHz}$.
The main contribution to the measured linewidth we attribute to the UV laser linewidth, which we can estimate from the measurement to be $\approx 100\,\text{kHz}$.
A second contribution comes from the Doppler shift of the resonance $\Delta_D = k \cdot v$ with the wave vector $k = 2\pi/\lambda$ and the wavelength λ of the Rydberg excitation laser. The velocity v parallel to the laser beam is calculated by $v = \sqrt{k_B T/m}$ with T the temperature, m the atomic mass and the Boltzmann constant k_B. After Raman sideband cooling and the reduction of the trap depth, we estimate an atomic temperature of $T \approx 200\,\text{nK}$ which produces a Doppler shift of $\Delta_D = 2\pi \times 23\,\text{kHz}$.
The last contribution comes from the variation in the light shift from the traps, which is a factor ten smaller than the measured linewidth.
With this method, we can track the daily shift of the UV laser due to the thermal expansion of the reference cavity. The big sidebands for the lock of the seed laser are changed in frequency accordingly to compensate for the shift.

For the characterization of the coupling, we prepare the atoms in the $4S_{1/2}, F = 2, m_F = +2$ ground state. For the spectroscopy measurement, we set the UV laser power to the maximum. The optical tweezers are in the same configuration as the one for the spectroscopy. We turn the UV light on at resonance for different amounts of time, and the atomic population is measured afterward. We show the results of the measurement in Fig. 2.8. With this measurement, the ground state population oscillates at the frequency of the Rabi coupling. The atoms excited to Rydberg are anti-trapped by the light we use to generate the optical tweezers and are consequently lost. The data is fitted with a damped oscillation function $f(t) = a \cdot \cos(2\pi \cdot \Omega \cdot t) \cdot \exp(-t/\tau) + c$, from which we can extract the Rabi frequency Ω and the decay time τ.

The largest Rabi frequency that we have measured is $\Omega \simeq 2\pi \cdot 400\,\text{kHz}$.

a

Occupation

1

0.8

0.6

0.4

0.2

0

−200 0 200 400
UV frequency (kHz)

b

1

0.8

0.6

0.4

0.2

0

0 5 10
Time (µs)
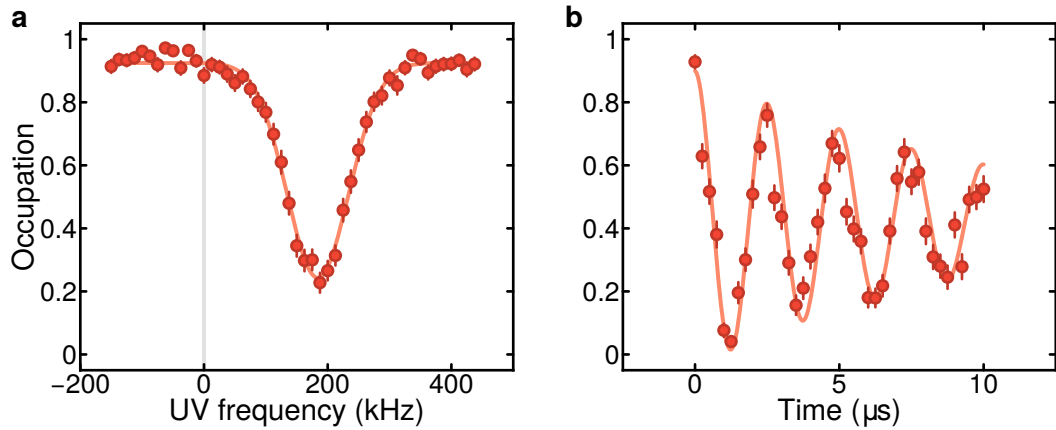
Figure 2.8: Rydberg spectroscopy and Rabi coupling measurements. a Spectroscopy of the $4S_{1/2}.F = 2.m_F = +2$ to $62P_{1/2}, m_J = -1/2$ at a trap depth of $0.005 \times U_0$ after Raman sideband cooling, see Section 3.5.2. The data is the average over individual atoms. The vertical gray line indicates the free space resonance. **b** Rabi oscillation of $\Omega = 2\pi \cdot 400\,\text{kHz}$ of the atoms inside the traps in the same configuration as the spectroscopy. The data is the average of the individual atoms. Figure adapter from [77].

Part II

Tweezers for Potassium Atoms

Chapter 3

Tweezers for Potassium Atoms

This chapter will describe how we generate the arrays of optical micro-traps, the so-called tweezers, that we use for the experiments in this thesis. We start with the description of the holographic setup and the technique that we have implemented for the generation of the optical tweezers in Section 3.1.

Section 3.2 proceeds to describe motivations for the use of 1064 nm light to generate the traps and the technique that we implement for loading them with single atoms. Subsequently, we characterize our imaging fidelity of the trapped atoms. Subsequently, we can characterize the traps, and we check for their homogeneity and measure the occupation lifetime of the trapped atoms in different configurations, as we shall see in Section 3.3.

Then we describe our attempt to improve the traps' loading probability with a deterministic loading technique, in Section 3.4.

Finally, in Section 3.5 we illustrate three techniques that we implement, which are crucial for the realization of the experiments in this thesis. We talk about the Raman sideband cooling technique, the atomic state preparation, and how we drive ground state transitions with a Raman technique.

3.1 Generation of optical tweezers

In recent years optical tweezers have become a prominent platform for few-body [33, 34, 78–81] and many-body experiments, especially due to their fast experimental duty cycle and flexibility. In the first attempts, a single trap was generated by focusing down a Gaussian beam [20, 82] creating a single trap. In order to increase the number of traps, one can use acousto-optic modulators (AOM). By using both zeroth and first deflected order, and two AOMs in succession, a maximum of four traps can be generated [83].

Techniques that largely improved these limitations come from the use of microlens arrays [84], acousto-optic deflectors (AOD), and spatial light modulators (SLM). An SLM imprints a spatial phase onto an impinging light field to create reconfigurable arrays of microtraps [27, 84–86] or to generate a specific intensity pattern to produce trapping potentials both in 2D [87–90] and 3D configuration [28, 29, 91], or uniform light beams [92]. AODs are optimized to have a larger input bandwidth than AOMs and can generate many deflected beams used to generate traps. Using two crossed AODs, one can create 2D patterns. AODs also allow the implementation of the transport of individual atoms in an already generated pattern to completely fill the array in a certain region [23, 24]. A successful attempt for the re-arrangement was also carried out by continuously changing the position of the tweezers by modifying the SLM phase pattern continuously

as in reference [93].

In our experiments, we have chosen to generate the microtraps with an SLM since it is more flexible for creation of arrays with arbitrary geometries, with an additional setup with AODs to implement the sorting of the loaded atoms we are going to add in the future. We show an example result of our implementation in Fig. 3.1, where we can see the generated array from the algorithm and the signal from the trapped atoms in a single experimental realization and by averaging many to see the whole array.

A detailed description of this technique can be found in the master thesis of Philip Osterholz [94].
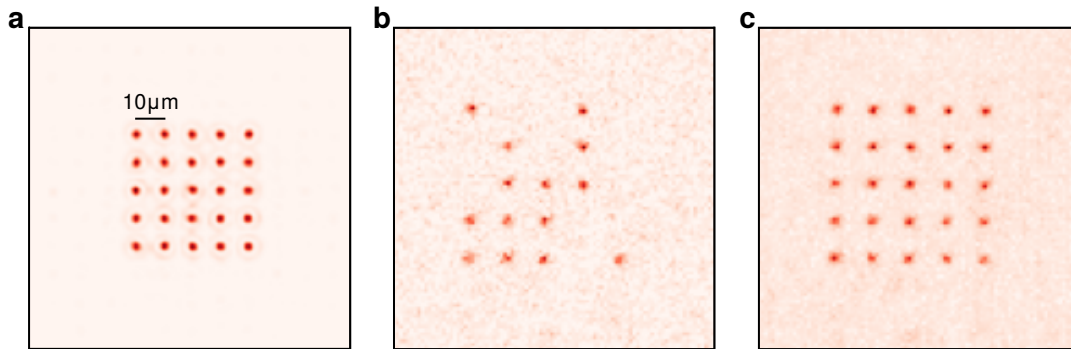

Figure 3.1: Example of a tweezer array. a Calculated intensity pattern of the phase pattern generated for the production of a 5×5 array of traps with $10\,\mu m$ spacing. **b** Fluorescence image of a single experimental realization of single Potassium39 atoms trapped in the array. Not all the traps are filled due to the stochastic loading of the traps. **c** Average image of several experimental realizations of single Potassium39 atoms trapped in the array.

3.1.1 Spatial Light Modulator setup

The light for the generation of the tweezer patterns is produced by a high-power laser system from Azur Light Systems, which can provide a maximum of 40W of power at 1064 nm. We have depicted a schematic of the setup in Fig. 3.2. The light is controlled and stabilized by an acousto-optic modulator (AOM) and a PI loop made with a home-built stabilization circuit. We have implemented two stabilization circuits using two photodiodes and two PI stabilization controllers, one for high power and one for low power. The two circuits have a factor 100 difference in sensitivity. An RF switch allows the passage between the two control loops ensuring a high dynamic range for the power stabilization during the sequence. The beam is then passed through two telescopes to magnify it to a $1/e^2$ diameter of 12mm, matching the SLM chip size. The first telescope is made up of f= 75 mm and f= 150 mm. The second one is composed of an $f_1 = 50$ mm lens and a 2-inch lens with an $f_2 = 300$ mm. Before impinging onto the SLM, the beam passes through a circular aperture made by an iris with a diameter equal to 12mm. After the SLM, a flip mirror allows the path to split, with the possibility of redirecting the light onto a diagnostic path. The main path after the SLM is made up of a telescope in a 4-f configuration. With the telescope,

we image the SLM onto the back focal plane of the objective. The telescope is made up of an initial 2-inch lens with focal length $f_3 = 250\,\text{mm}$ and the second one of a 3-inch lens with focal length $f_4 = 800\,\text{mm}$. This telescope magnifies the beam in the SLM plane to a size of $40\,\text{mm}$ $1/e^2$ diameter, corresponding to the size of the objective entrance. After the first lens, we apply a spatial filter to filter out the zero-order and additional displaced light not used for the tweezers. A dichroic mirror reflective between $950\,\text{nm}$ to $1100\,\text{nm}$ and with a transmissive between $670\,\text{nm}$ to $810\,\text{nm}$ allows the $1064\,\text{nm}$ light to be superimposed with the path used for imaging.
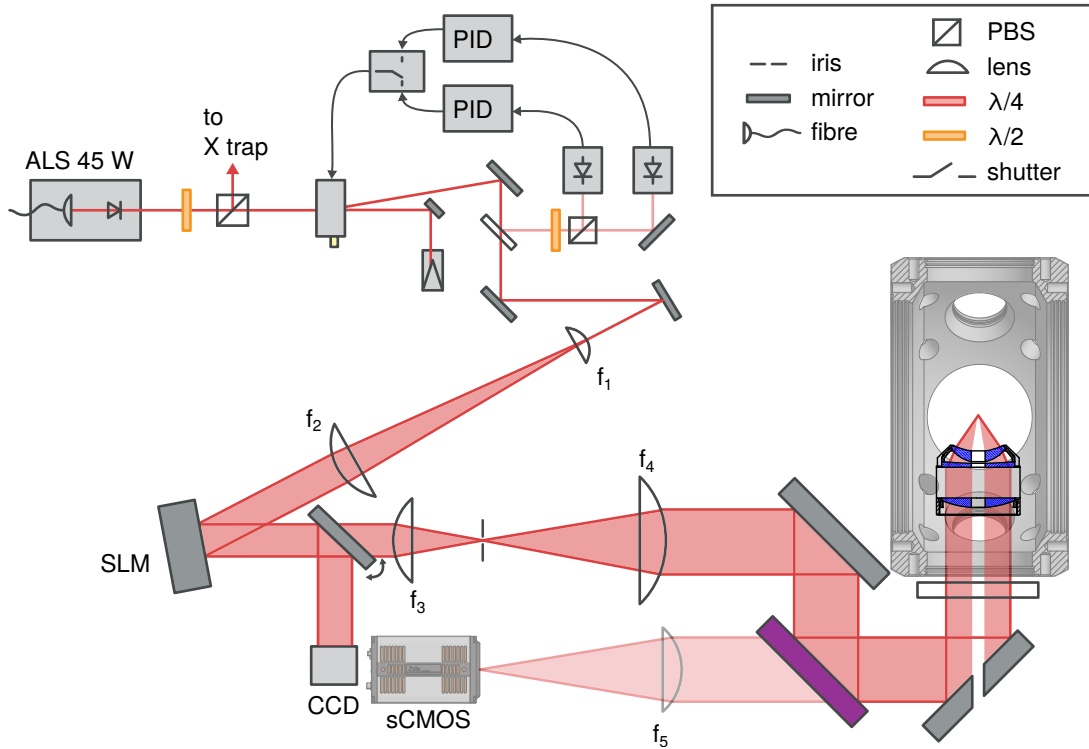
Figure 3.2: Tweezers generation setup. A high-power fiber amplifier laser provides the laser light. The laser power is stabilized and controlled by an AOM. The same AOM modulates the signal, as is explained in Section 3.2. Two intensity stabilization loops provide a high dynamical range to stabilize the laser power down to a few per mill to the maximum. We use a radio-frequency switch to change between the two loops. Two telescopes, which are only represented in the figure by the telescope composed of f_1 and f_2, expand the beam to a $1/e^2$ diameter of $12\,\text{mm}$, to match the smallest dimension of the SLM. The last telescope in the setup, f_3 and f_4, expands the beam and images the SLM plane onto the objective's back focal plane. After the f_3 lens, the traps pattern is reproduced, and we place a spatial filter to block the light not used in the pattern. We superimpose the optical path to generate the traps with the fluorescence imaging path with a dichroic mirror. We use the in-vacuum objective to generate the traps and the imaging of the trapped atoms. Figure adapted from [62].

We generate the tweezers using a holographic technique that will be discussed in Section 3.1.3. The technique involves imprinting a phase pattern onto

the trapping light. The phase pattern modulates the light field to make tightly focused beams once a lens or an objective focuses it down. We can imprint the phase pattern using a spatial light modulator (SLM). To do so, we chose an SLM based on liquid crystals, the water-cooled Hamamatsu X10468-3. We chose this SLM because of its high efficiency in light utilization 97 % and the possibility to use optical powers up to < 250 W for a beam with a $1/e^2$ diameter of 12 mm. All the relevant properties for the SLM that we use can be found in Table 3.1.
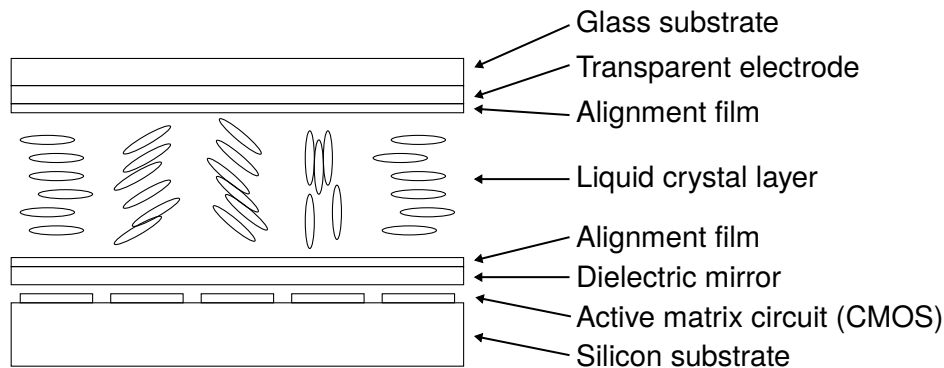

Figure 3.3: Schematic diagram of the liquid crystal spatial light modulator. The impinging linearly polarized light goes through the layers and is reflected by the dielectric mirror. The reflected light is subsequently subjected to a spatially dependent phase modulation caused by the liquid crystal layer. We modulate the phase by regulating the refractive index of the liquid crystal medium, given by the orientation of the crystals. Such orientation is controlled by the active matrix circuit together with the transparent electrode. Figure adapted from [94].

The chip has multiple layers. On the outside, there is a glass substrate followed by a transparent electrode. Two alignment films confine the liquid crystal and ensure the proper orientation of the crystals. In our experiment, the orientation is such that the phase modulation is only possible for linearly polarized light oriented parallel to it, not affecting other polarization components. A dielectric mirror reflects the light. After the mirror, a silicon substrate with an active pixel matrix deposited on top is present. The pixel matrix consist of 792×600 electrodes with a size of 20 μm $\times$ 20 μm, with a CMOS based circuit underneath them. The CMOS structures make it possible to apply individual voltage levels to each pixel. The electric field that forms between the pixel and the common transparent electrode changes the orientation of the liquid crystal. In this way, the refractive index is locally modulated, modifying the optical path length through the pixel. The modulation creates a position-dependent phase shift. The phase can be modulated over the full range of 2π with an 8 bit discretization.

Resolution	792×600
Pixel pitch	$20\,\mu m$
Effective area	$16\,mm \times 12\,mm$
Phase levels	256 (8 bit)
Fill factor	$98\,\%$
Light utilization	$97\,\%$
Refresh rate	$60\,Hz$

Table 3.1: Properties for the Hamamatsu X10468-3 LC-SLM.

3.1.2   Aberration correction

Even with precise alignment along the path, the beam can catch up wavefront distortions that produce aberrations. The distortions affect the quality of the traps that we want to produce. To compensate for these distortions in the path before the SLM and also possible effects from the SLM itself, we apply a technique described in reference [95] to characterize the optical aberrations and produce a compensation pattern. The technique consists in displaying a phase vortex on the SLM. The phase goes from 0 to 2π around the center of the SLM. The vortex produces, in the image plane, a doughnut-shaped mode particularly sensitive to aberrations. Zernike polynomials are used to characterize the errors in wavefronts. They form an orthonormal basis on the unit disk [96]. In the context of aberrations, Zernike polynomials identify individual aberrations and are used to describe typical lens errors and misalignment effects. We superimpose the contribution of the first orders of Zernike polynomials with different coefficients, corresponding to astigmatism, coma, and trefoil, on our SLM's phase pattern. In turn, we tune the coefficients to minimize the asymmetry and distortions of the doughnut mode. The compensation pattern found can then be used generally to compensate for the aberrations.

The diagnostic path shown in Fig. 3.2 is applied by turning the flip mirror after the SLM to direct light onto a CCD camera and perform the characterization of aberrations. Additionally, we sum to the pattern of the doughnut mode a Fresnel lens pattern with a focal length of $3\,m$ to avoid the use of an additional lens that can influence the wavefront after the SLM. The results are shown in Fig. 3.4. We can compensate the aberrations accumulated on the optical path only up to the position immediately after the SLM, at the position of the flip mirror.

Alternatively, we can rely on measurements with atoms trapped in the generated tweezers to correct aberrations further. A similar idea was applied in reference [97] using the signal of a generated array in a camera.

3.1.3   Generation of arbitrary 2D arrays of optical tweezers

Optical tweezers can be thought of as tightly focused dipole traps. To imprint a phase pattern on a light wavefront to produce such a result is not trivial. An algorithmic approach using a version of the Gerchberg-Saxton algorithm [98] can provide an adequate solution to the problem in the case of spatially separated tweezers and has been successfully implemented in the past [27]. The algorithm

a

b

Before Correction   After Correction

c
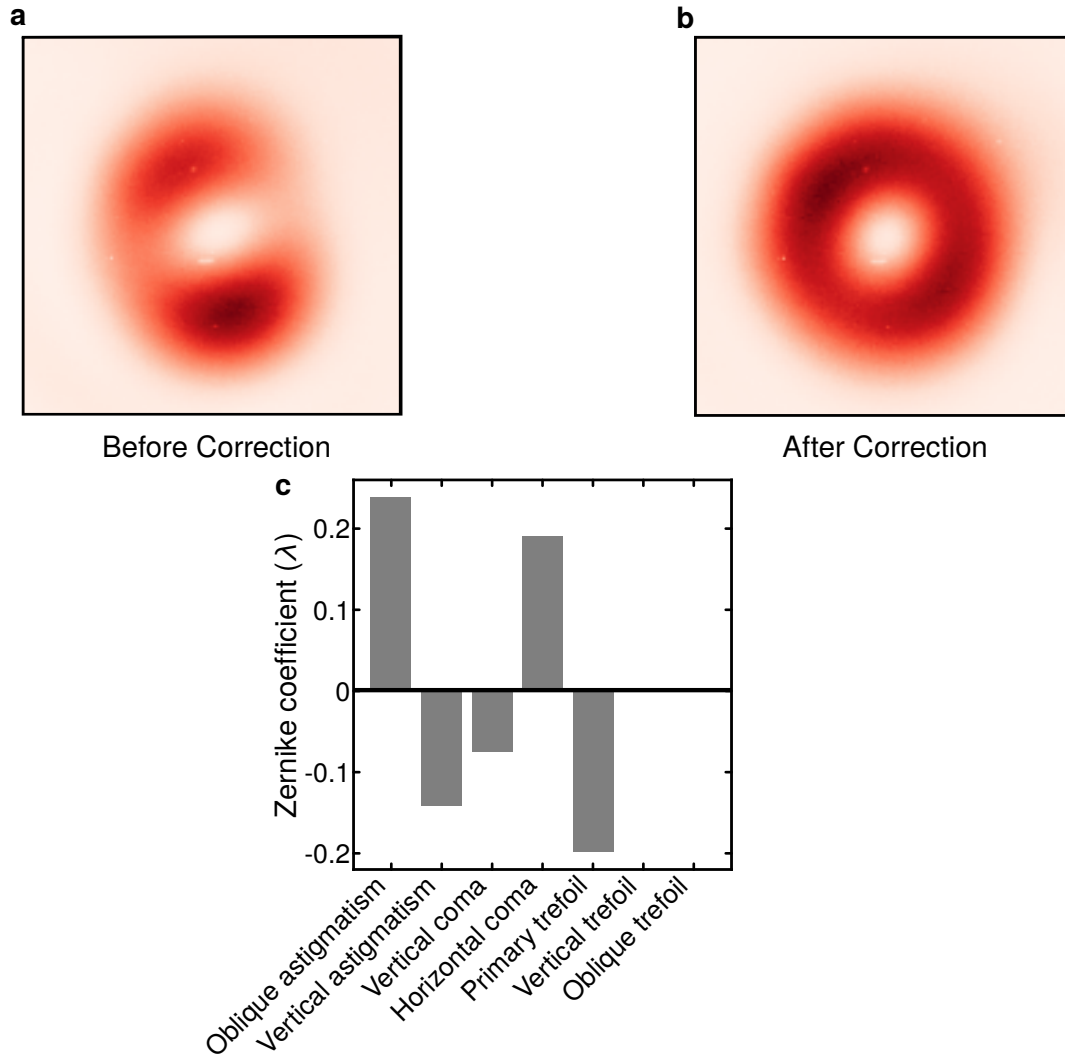
Figure 3.4: Aberration correction with a doughnut mode. **a** Image of the doughnut mode before the application of the compensation pattern onto the SLM. **b** Doughnut mode after the addition of the calculated compensation pattern onto the SLM. **c** The Zernike coefficients that were calculated from the first picture and have been applied to produce the second one. Figure adapted from [94].

relies on the Fast Fourier Transformation as the propagator to go from the SLM plane and the image plane.

The algorithm takes the distribution of the amplitude of the incident beam onto the SLM, referred to as the SLM plane, and the desired amplitude distribution in the image or trap plane. Both distributions are evaluated on a two-dimensional grid with the same dimensions $N_x \times N_y$, interlinked in the length scales by the Fourier transformation. The physical dimension of a unit in the image plane $\hat{\Delta}_x \times \hat{\Delta}_y$ is related to the dimension of a unit in the SLM plane $\Delta_x \times \Delta_y$ by

$$\hat{\Delta}_x \times \hat{\Delta}_y = \frac{\lambda f}{N_x \Delta_x} \times \frac{\lambda f}{N_y \Delta_y} \qquad (3.1)$$

A single iteration of the Gerchberg-Saxton algorithm looks as follows:

step 0: Preparation. In the case of the first iteration step, we combine the amplitude distribution of the incident beam with either a random or initially guessed phase distribution. The incident beam is the initial light field in the SLM plane.

step 1: Propagation to trap plane. The light field with the incident beam profile as amplitude and phase from the previous step is propagated to the trap plane using the Fast Fourier Transformation.

step 2: Manipulation in trap plane. We conserve the calculated phase in the trap plane, but replace the amplitude distribution with the desired amplitude distribution.

step 3: Propagation back to the SLM plane. We propagate the obtained light field back to the SLM plane using an inverse Fast Fourier Transformation.

step 4: Manipulation in the SLM plane. Analogously, we keep the phase information of the calculated light field while we replace the amplitude again with the distribution of the incident beam.

step 5: Repeat and stop. The algorithm is repeated from step 1 for a certain amount of iteration and then stopped. Usually, the algorithm is repeated for a few tens of iterations as the convergence rate of the final result to the desired amplitude distribution in the trap plane significantly reduces.

A graphical schematic of the algorithm is illustrated in Fig. 3.5. We will call cycle 1 the path following switch 1 and cycle 2 the one following the switch 2. For the algorithm described before, we followed cycle 1.

We can use the result of the previous algorithm as a starting point for a second one that helps improve the convergence to the desired amplitude distribution. In the case of the generation of diffraction-limited dipole traps, we can implement specific modifications. The first modification that we do is to take the amplitudes of the traps from the previous algorithm and follow cycle 2 in Fig. 3.5. The procedure requires the previous algorithm to produce spots at the correct positions but with potentially wrong amplitudes. The technique is called weighted Gerchberg-Saxton algorithm (WSG) [99]. We can substitute Step 2 with the following:

step 2′: We extract the amplitudes A_i^n, with n denoting the trap and i indexing the iteration of the algorithm of the traps in the calculated pattern. We keep the phases of the calculated pattern while we replace the amplitudes with a new amplitude distribution where we weight the amplitude of individual tweezers with the following factors

$$g_i^n = \frac{A_{goal}^n}{A_i^n} \cdot g_{i-1}^n \qquad (3.2)$$

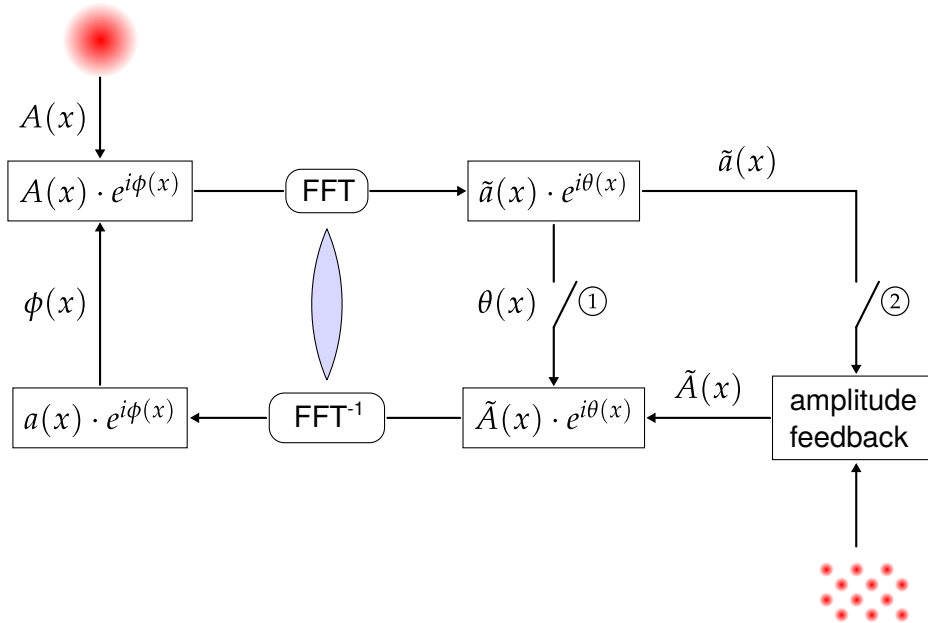where A_{goal}^n is the desired amplitude for the nth trap.

Figure 3.5: Modified Gerchberg-Saxton algorithm. Cycle 1: We follow the path closing switch 1. The operations correspond to the standard Gerchberg-Saxton (GS) algorithm to find the phase pattern. Starting point at the top left, with the initial phase, generated randomly. Cycle 2: Now, we follow the path closing switch 2 and opening 1. **The weighted Gerchberg-Saxton (WGS) algorithm:** The traps are individually attenuated or amplified to improve uniformity. Cycle 1 with fixed phase: We open switch 2 and close again switch 1. **The Gerchberg-Saxton algorithm with fixed phase (FixedPhaseGS):** The phase is fixed and no further change is imposed anymore in the trap plane. We use the phase profile of the first iteration of the cycle. Figure adapted from [94].

We made a second modification along the line of the previous one, with the requirement that cycle 2 produces also trap amplitudes close to the desired ones [100].

step 2'': At this iteration, we follow cycle 1 with a difference, we save the phase distribution of the calculated light field ϕ_1 in the trap plane. Following this iteration, we use the calculated amplitude distribution to calculate the weighting factors as in Eq. (3.2). We replace the amplitude of the light field with the desired amplitude applying the corresponding weight to each trap. Then the phase distribution is replaced by ϕ_1. We refer to this modification as the fixed phase Gerchberg-Saxton algorithm (FixPhaseGS).

We show in Fig. 3.7 the deviation from the desired intensity pattern to the algorithm produced at every cycle. We continue in this way for a target pattern of 5×5 square array of traps. In each iteration, we extract the field amplitude in the same way as for calculating the weighting factors in the implementation of the modified GS algorithm. The result is then squared to retrieve the power distribution among the traps. The evaluation is branched whenever the algorithm
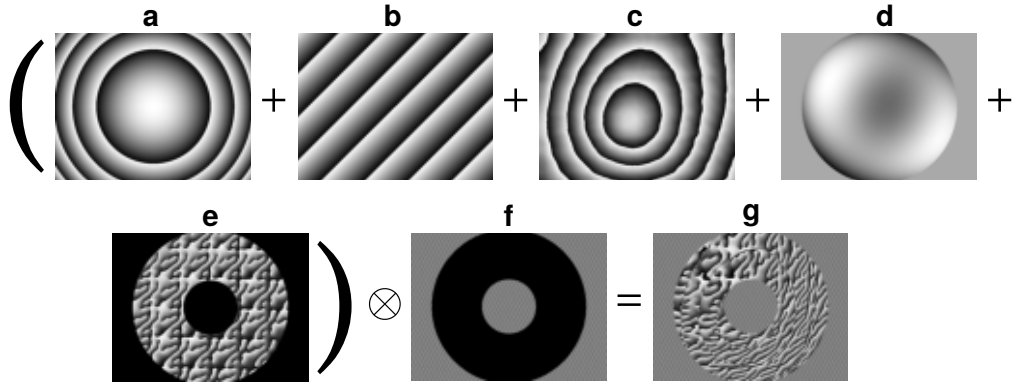
Figure 3.6: Phase pattern construction. We sum up the different parts to make the phase image that we display onto the SLM. **a** the Fresnel lens pattern, **b** a displacement pattern, **c** the surface correction pattern provided by the manufacturer, **d** the aberration correction pattern, and **e** the pattern for the desired trap array. Then **f** a mask is applied to deflect all the beam parts that do not enter the objective. The last image **g** is the combination of all the patterns which we display onto the SLM. Figure adapted from [94].

changes, while the previously used algorithm continues in parallel to compare the different combinations of algorithms used. We can see that theoretically, after every modification, we reduce the deviation from the desired intensity pattern significantly, and each algorithm converge after a certain number of iterations. Note that the intensity pattern used to calculate the deviation is retrieved from the algorithm and does not come from a measurement. In Section 3.3 we characterize the traps that we generate, and we can see that the deviation from the desired intensities is quite significant with respect to the deviation calculated before to check the converge of the algorithms.
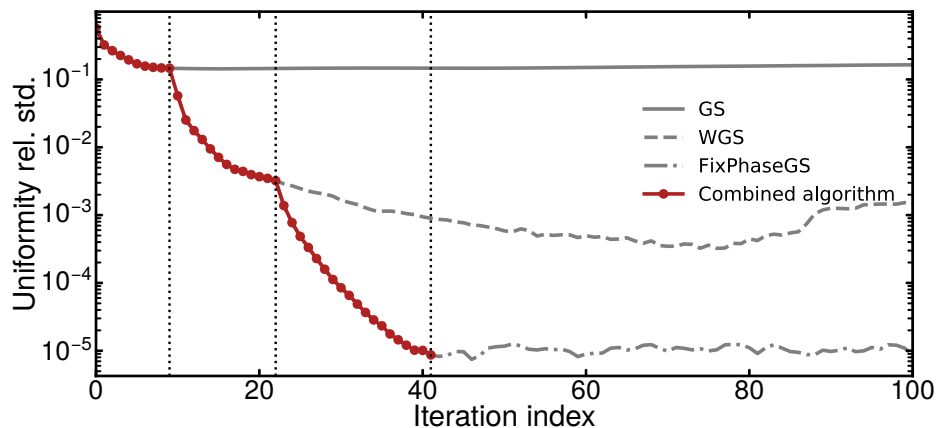

Figure 3.7: Convergence of the algorithms. The deviation from the desired intensity pattern is plotted as a function of the iteration value of the Gerchberg-Saxton algorithm. The vertical line shows when we switch one version of the algorithm, while the grey plot shows the deviation value of the algorithm without changing the used algorithm. Figure adapted from [94].

We show in Fig. 3.14 several patterns that we have generated with our SLM. The arrays are the ones that we use in the experiments shown in this thesis, plus a couple more to show the flexibility to create arbitrary patterns. The images are made by the fluorescence signal of atoms trapped into the generated traps, both from single experimental realizations and by averaging several realizations.

3.2 Loading and imaging of atoms in optical tweezers

Previous experiments with optical tweezers have successfully managed to load Rubidium atoms into the traps directly from a cold atomic gas or background vapor pressure [20, 23]. The polarizabilities do not match in the case of a wavelength that is not magic for the ground and excited states. The atomic transitions are shifted according to their value when free space by a light shift. In the case of Rubidium the most commonly used trapping light is between 800 nm to 850 nm. In this case, the ground state light shift is larger than the excited state one. The small differential light shift together with the large hyperfine structure of Rubidium allows for an efficient cooling both outside and inside the traps, making the loading of Rubidium or also Cesium quite straightforward.

In this section, we will describe the characteristics of the trapping light that we use. We will initially discuss the advantages of using 1064 nm light. Then we will describe the technique that we use for the loading of the atoms into the traps. Finally, we will characterize our imaging technique.

3.2.1 Trapping potential

As mentioned before, we use 1064 nm light to create the traps for the atoms. We chose this wavelength for several reasons. One reason is the low off-resonant scattering rate compared to other experiments, which use wavelengths closer to resonance [23, 24]. 1064 nm light is well detuned from the two possible transitions wavelengths: $\lambda_{1/2}$ at 767 nm for the D1 line $4S_{1/2} \to 4P_{1/2}$ and $\lambda_{3/2}$ at 770 nm for the D2 line $4S_{1/2} \to 4P_{3/2}$. Another important factor is the low effective magnetic field induced by an imperfection in the light polarization or strong light focusing, as discussed in this section. A spatially varying effective magnetic field can induce decoherence effects when we prepare the atom in a definite state of the ground state manifold. Lastly, laser systems are available at this wavelength that can provide high laser power in the order of several tens of Watts.

Now, we discuss the trapping potential that we generate. In the rotating wave approximation, we can write the dipole trapping potential as

$$U_{dip}(\boldsymbol{r}) \simeq \frac{\hbar \Gamma^2}{8 I_{sat}} \frac{I(\boldsymbol{r})}{\Delta_{eff}}, \tag{3.3}$$

where I_{sat} is the saturation intensity for the D1 and D2 transitions, Γ the natural linewidth, $I(\boldsymbol{r})$ the spatial dependent intensity of the trapping laser, and Δ_{eff} is the effective trapping laser detuning from the two atomic resonances D1 and

D2:

$$\frac{1}{\Delta_{eff}} = \frac{1}{3\delta_{1/2}} + \frac{2}{3\delta_{3/2}}, \tag{3.4}$$

with $\delta_{1/2} = \omega_L - \omega_{1/2}$ and $\delta_{3/2} = \omega_L - \omega_{3/2}$. We choose the trapping laser to be red-detuned with regard to the transitions ($\Delta_{eff} < 0$) such that we generate an attractive potential for the atoms towards the laser intensity maximum. In order to trap atoms from the compressed MOT cloud in which we have a temperature of $T_{cMOT} \simeq 100\,\mu K$ we need to have a potential depth $|U_{dip}^{max}|/k_B \simeq 1\,mK$ which is much larger than the motional energy of the atoms.

We can calculate the scattering rate for the atoms in our traps with the following formula

$$\Gamma_{sc} = \frac{I(\boldsymbol{r})}{8 I_{sat}} \Gamma^3 \left(\frac{1}{3\delta_{1/2}^2} + \frac{2}{3\delta_{3/2}^2} \right). \tag{3.5}$$

Using 1064 nm light with an intensity that produces a $k_B \times 1\,mK$ trap depth, focused down to a waist $w_0 = 0.8\,\mu m$ using an objective that provides, the scattering rate is $\Gamma_{sc} = 1.3\,Hz$, completely negligible.

Non-paraxial polarization effect

The case described previously is for linearly polarized laser light, which produces a uniform shift for all the ground state levels. In our case, the linear polarized light is focused down by our objective. The polarization remains transverse to the light ray, which is deflected. In the diffraction-limited volume around the focus, all the deflected rays interfere and can produce elliptically polarized fields [101, 102]. In the case of far detuned light, we can write the formula for the vector light shift for alkali atoms in the ground state as in [102]

$$U_{dip}(\boldsymbol{r}) = U_0(\boldsymbol{r}) \frac{\delta_{3/2} - \delta_{1/2}}{\delta_{3/2} + 2\delta_{1/2}} \boldsymbol{C}(\boldsymbol{r}) \cdot g_F \hat{\boldsymbol{F}}, \tag{3.6}$$

where $U_0(\boldsymbol{r})$ is the scalar dipole trap potential as in Eq. (3.3), $\hat{\boldsymbol{F}}$ is the total angular momentum operator and g_F is the hyperfine Landé g-factor. The vector $\boldsymbol{C}$ quantifies the direction and degree of ellipticity. It has a magnitude of 1 for circularly polarized light and 0 for linearly polarized. The potential is state-dependent and linear to the total angular momentum operator $\hat{\boldsymbol{F}}$, and produces the same energy shifts as a magnetic field. The most important term is then the polarization gradient dC_x/dy in the case of linear polarization aligned along the y-axis. Considering a lens illuminated by a Gaussian beam with $1/e^2$ diameter equal to the lens diameter, the maximum gradient corresponds to

$$dC_x/dy = 2.6\,NA \sin(NA/\lambda). \tag{3.7}$$

For our system the maximum gradient is then $dC_x/dy = 0.065\,1/\mu m$ which corresponds to an effective magnetic field gradient if we use it in Eq. (3.6). This

effect is important because it can bring rapid internal-state decoherence on the time scale of the radial trap oscillation period, as shown in reference [102]. A strong enough magnetic field must be applied to fix the quantization axis.

The value of the effective magnetic field gradient in our case is smaller by a factor $\sim 10 - 100$ compared to previous experiments with Rubidium [102, 103], ensuring negligible internal-state decoherence with the application of a small magnetic field.

3.2.2   Loading of the atoms into the traps

So far, the energy shift exerted on the ground states by the trapping light has been discussed. Now we are going to describe the effect on the excited states in the case of the $4P_{1/2}$ and $4P_{3/2}$ manifolds. The polarizabilities of both excited states α_e do not match the one of the ground state α_g. Subsequently, the cooling into the tweezers is hindered by a series of effects. First, one limit comes from the heating due to fluctuations of dipole forces [104] from jumps in the potential trapping gradient experienced by the atoms. Secondly, cooling is inhibited due to the breakdown of the hyperfine coupling [105, 106], and a spatial variation of detuning, which can induce scattering by near-resonant photons.

This is a severe problem since cooling is needed to load the atoms into the traps and the fluorescence imaging of the trapped atoms. Thus an uncontrolled light shift can hinder the successful operation of the optical tweezers.

Potassium39 experiences strong differential light shifts between the ground state and the excited states in the case of 1064 nm trapping light. This is shown in Fig. 3.8 and has been reported in reference [17]. The difference in light shift is caused by the $4P \leftrightarrow 3D$ transition correspond to a wavelength of 1170 nm from the $4P_{1/2}$ and of 1178 nm from the $4P_{3/2}$.

In the case of the $4P_{1/2}$ states, the light shift experienced by the atoms is the same for all the Zeeman states manifolds. For the $4P_{3/2}$ state, the atoms experience a variety of different light shifts depending on the Zeeman sublevel m_F. If we consider a typical trap depth of $U \approx k_B \times 1\,\text{mK} \approx 2\pi\hbar \cdot 20\,\text{MHz}$ for the ground state, the light shift in the $4P_{3/2}$ manifold goes from a fraction of the trap depth to 8 times the trap depth, comparable to the hyperfine splitting $\approx 2\pi\hbar \cdot 20\,\text{MHz}$ inhibiting the sub-Doppler cooling via red molasses as in reference [71] and with the possibility of heating the atoms by resonant excitation.

To solve the problem of loading and imaging caused by the light shifts, we implemented the same method that was successfully applied for Sodium atoms by the Ni group in reference [104]. The idea takes inspiration from techniques for light-shift-free imaging of optically trapped atoms [107, 108]. The idea is to alternate trapping and cooling lights to avoid having them both on simultaneously. We modulate the intensity of both lasers with square waves at a frequency of 1.4 MHz. The technique works as long as the trap modulation frequency is much greater than twice the trap frequencies to avoid the parametric heating of the atoms in the traps [109]. On the other side, the modulation frequency should be less than the typical decay time of the excited state of the atom $\tau = 26.7\,\text{ns}$, where the atomic natural linewidth is $\Gamma/2\pi = 5.9\,\text{MHz}$, such that
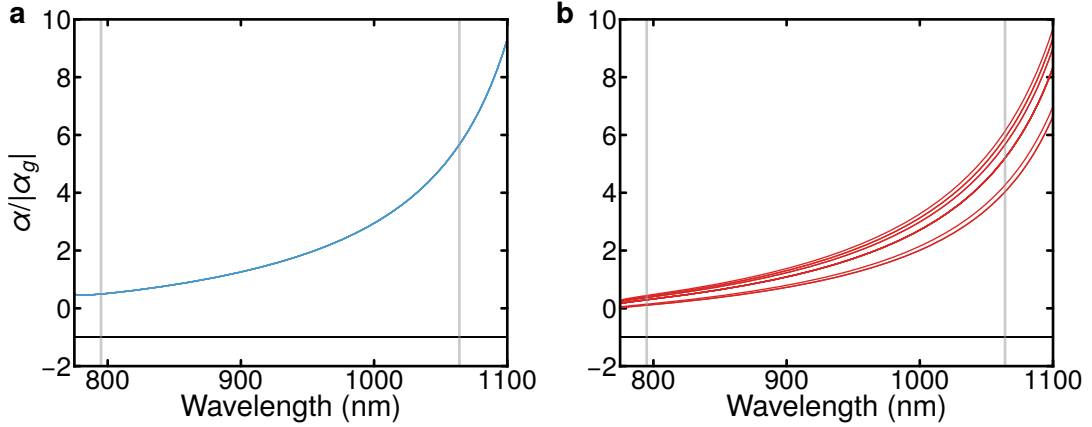
Figure 3.8: Plot of the ground and excited states polarizabilities. a We plot in blue the polarizability for the $4P_{1/2}$ Zeeman sublevels normalized with respect to the absolute value of the ground state $4S_{1/2}$ polarizability α_g, shown in black. The ground state is normalized to its absolute value, indicating only if the potential is attractive or repulsive. **b** We plot in red the normalized polarizability for $4P_{3/2}$ Zeeman sublevels. Several lines are visible showing that the Zeeman states in the hyperfine manifolds present very different polarizabilities especially in the event of 1064 nm light. The grey vertical lines mark 795 nm and 1064 nm light wavelength.

there is enough time for the excited atoms to decay into the ground state before the trapping light is on again.

We implemented the modulation, or chopping, using the already present AOMs in the path of the cooling lasers and the one for the stabilization of the high power 1064 nm ALS laser. We modulate the driving frequency of the AOMs by using RF switches before being transmitted to an amplification stage. The cooling beams have a duty cycle of $\sim 25\%$, while the tweezer light has a duty cycle of $\sim 45\%$ to minimize the overlap between the two. The size of the beams also limits the modulation frequency into their respective AOMs, which were not optimized for fast switching at the time. The 1064 nm is intensity stabilized with a PID circuit, see Fig. 3.2, and the signal from the photodiode to the PID controller is low passed well below the modulation frequency to average over the fast modulation. The averaging increases the peak intensity value set by the PI controller to maintain the set voltage value. The required peak intensity during the modulation limits the number of tweezers that we can operate. The peak power required during the so-called chopping is a factor $\sim 2.3 \times P_0$ higher than the unmodulated one.

The light modulation allowed us to load and image Potassium39 atoms in diffraction-limited tweezers directly from an red molasses cooled cloud at $T \approx 30\,\mu K$.

As we show later on in Section 3.4, we are also able to load the atoms with the use of gray molasses cooling on the D1 transition. The loading is possible thanks to the extensive working range of the gray molasses technique with respect to the detuning from the D1 transition [72]. Also, the Zeeman manifolds of the D1 line are shifted in a scalar fashion by the trapping light, preserving its hyper-
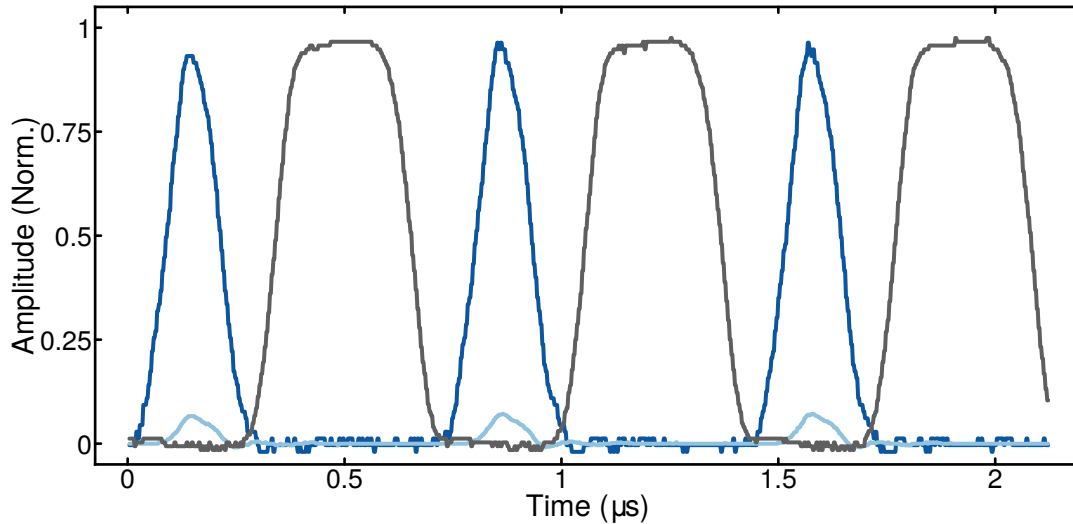
Figure 3.9: Modulated signal of cooling and trapping light. Photodiode signals of the cooling light, with the cooler in dark blue, the repumper in light blue, and the trapping light in black. We normalized the cooler and trap light signals. We keep the ratio of cooler and repumper the same as in the experimental sequence.

fine structure. We are not able to perform imaging with gray molasses cooling since the number of photons scattered is much lower compared to the number of photos scattered with the red optical molasses [110]. A third way to load the atoms is directly from the atoms trapped in a dipole trap. We need to perform pair projection to prepare only one atom per tweezer after loading. We perform the imaging in the same way by chopping both trap and cooling light.

The experimental sequence for the loading of the tweezers is the following. A magneto-optical trap (MOT) is loaded for 200 ms, the atoms have an average temperature of $\sim k_B \times 1\,\mathrm{mK}$. Then, the atoms are cooled with a compressed MOT technique to lower the temperature to $\sim 200\,\mu\mathrm{K}$. We make a further cooling step with gray molasses cooling, which reduces the temperature further to $\sim 40\,\mu\mathrm{K}$. To load the tweezers, we apply the modulation as explained previously with the use of a sub-Doppler laser cooling method similar to the optical molasses described in reference [71]. The loading of the atoms into the traps occurs over 40 ms. After loading, the cooling light is switched off for 20 ms to let the not captured atoms fly away. After that, another pulse of cooling light with the same power and detuning is applied over 10 ms to perform the parity projection and leave only one atom per tweezer with 50 % probability.

Modulation of the MOT mirrors

While measuring the loading probability of each tweezer, we see an effect similar to the one seen in the case of optical lattices by [15, 16, 111]. In the optical lattices cases, the cooling beams were interfering, creating a low and high-intensity landscape that influenced the cooling and photon scattering from the trapped
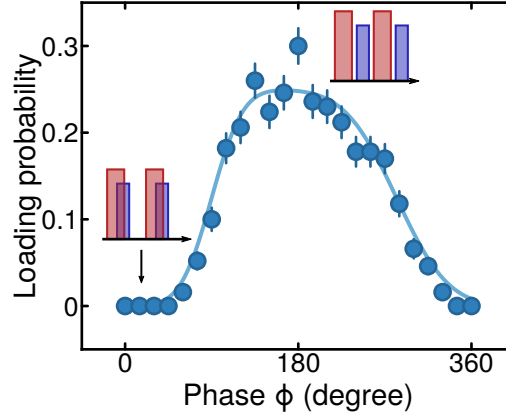
Figure 3.10: Optimization of the modulation. In red, we indicate the trapping light, and in blue, the cooling. We modulate both at the same frequency. The phase between the two signals is indicated by ϕ. We plot the loading probability as a function of the phase ϕ between the cooling and trapping light. The cooling light is kept on for 150 ms to increase the sensitivity of the measurement. The maximal loading probability is limited to 30% due to the length of exposure. The light blue line is a guide for the eye.

atoms. We observe a similar effect with the loading and the imaging of atoms. We modulate one mirror for each direction to average the modulated intensity over the traps to correct it. We implement the mirror modulation by glueing the mirrors to piezoelectric stacks and applying a sinusoidal wave at a frequency of 400 Hz to 500 Hz. The piezoelectrics are driven with a voltage, 50 V_{pp} to attain a movement of 2 µm in the x- and y-axis, and 20 V_{pp} to attain a movement of 3 µm along the z-axis. The modulation frequency needs to be slower than the scattering rate of the atoms $\Gamma/2\pi = 5.9$ MHz, but faster than the imaging time ~ 6 ms. To check if the modulation of the mirrors has an effect on the loading probability, we continuously took data for almost an hour with and without the mirror modulation. We evaluate the loading probability for each tweezer in a 5×5 array with 20 µm spacing. We show the result of the loading probability per tweezer as a function of time in Fig. 3.11.

In the case of no modulation of the MOT mirrors, the loading probability varies in time, going from $\sim 50\%$ to almost zero for some traps. With the modulation of the MOT mirrors, the loading probability becomes uniform over the whole array. The variation in the loading probability for the experiment with mirror modulation is due to the limited averaging of over 50 experimental realizations.

3.2.3   Imaging of single atoms

The method most commonly used to image single atoms is fluorescence imaging. In the event of imaging of single atoms, the technique requires the atoms to scatter light while being cooled simultaneously. Several groups successfully implemented the technique in optical lattices with the use of polarization gradient cooling or sideband cooling, both for alkali [15–17, 19, 105, 112] and alkali-earth atoms [113, 114]. Similar techniques have been implemented with single atoms
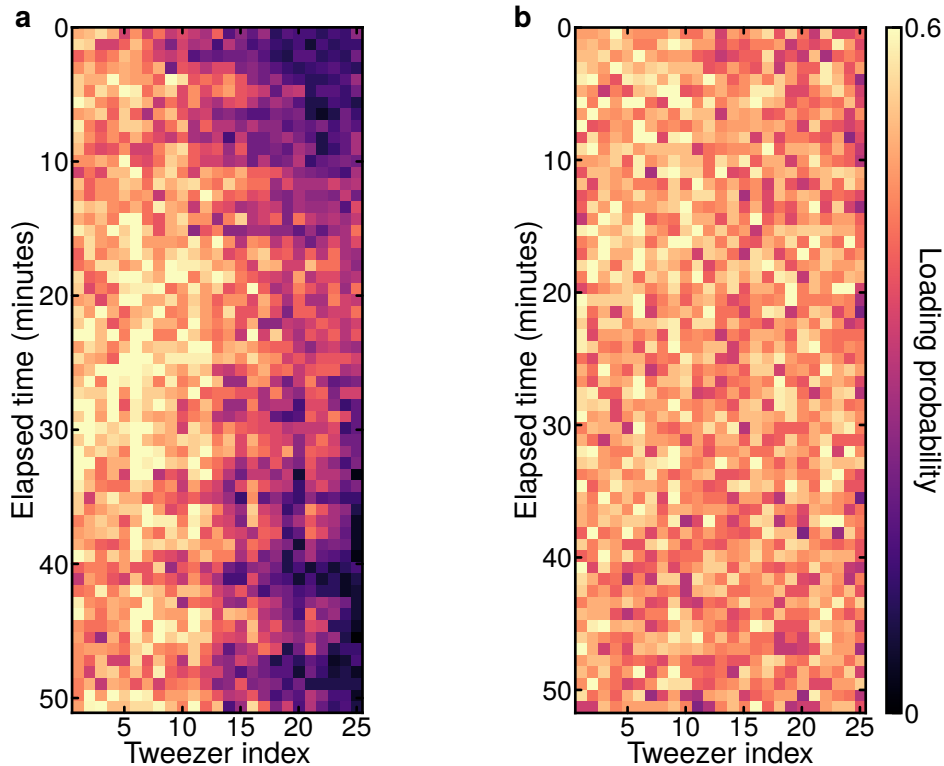
Figure 3.11: Loading probability and mirror modulation. Loading probability as a function of time for each individual tweezer using a 5×5 array with $20\,\mu m$ spacing. The averaging is only done over 50 experimental realizations. **a** MOT mirrors are not modulated. **b** MOT mirrors are modulated.

trapped in tweezers for both alkali [20, 115, 116], alkali-earth atoms [117–120], and also in a 3D configuration [28, 29, 121] and bi-atomic molecules [122]. At this stage, we will show the fidelity of our imaging technique. We are going to comment on the probability of losing an atom after a single imaging process. This probability is important for the experiments that we want to perform and the generation of defect-free arrays by the movement of the atoms in the traps [23, 24, 26]. A low loss is also important with the possibility of reinitializing the atomic array to perform several experiments in series without reloading the array every time [123].

The imaging system is described in Section 2.2. The choice to use a CMOS camera rather than a more commonly used EMCCD camera was due to two reasons. First, the signal-to-noise ratio of a CMOS camera in mid-level photon events, with $> 100\,photons/pixel$, is superior to the EMCCD one, as also seen in Reference [115]. Second, at the time, there was a substantial price difference between the two. Since the SNRs were comparable, we went for the cheaper option.

We determine if an atom is present or not inside a tweezer in a binary way. First, we need to define the position of the tweezers. We take several pictures, and by averaging, we can identify the positions of the point spread functions (PSF) of the light emitted by the atoms. In our case, there cannot be any drift

between the atomic PSF or defocusing since we are using the same objective to generate the traps and collect the fluorescence signal.

Once the positions are known, we can define a region of interest where we sum up all the counts from the pixels in the region. One must carefully tune the size of the region of interest since using an increasingly large image area only results in additional noise to the signal. Another method would be to perform a weighted sum over the pixels. We weight each pixel by the pixel values of the averaged PSF [117, 119]. We use the simple method of summing the pixels' values in a determined region of interest since we do not find it limiting for the experiments.

We have to choose a classification threshold. All the signals below the threshold are classified as non-detected atoms, and the signals above as atom detected.
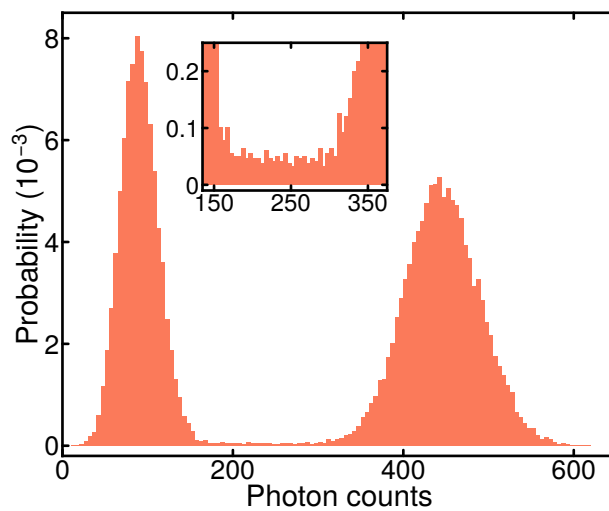
Figure 3.12: Histogram of the camera counts. Typical histogram denoting the signal from the camera for several experimental realizations in a region of interest. In the inset, the region between the two peaks is zoomed in, and the presence of a continuous signal connecting the two peaks are shown, corresponding to the signal of lost atoms during the imaging process.

Imaging fidelity

The fidelity F is the probability of the binary decision being true and corresponds to the accuracy of our binary classification. The statement applies when we start the imaging process since we may lose the trapped atom during this time.

By making many imaging runs and fixing the dimension and positions of the regions of interest, we can produce the signal counts histogram, see Fig. 3.12. The histogram is formed by signals with and without atoms. A way to decide when an atom is present and when it is not is to set a threshold. Below the threshold, we consider the signal as the absence of an atom, and above, as one atom is present.

At this point, we can quantify the fidelity of the process. We have to model the two distributions in the histogram, and the fidelity comes from integrating both distributions up to their respective side of the threshold. As done in references [115, 124], we can model the two contributions to normalized Gaussian func-

tions:

$$P(c) = \frac{p}{\sqrt{2\pi\sigma^2}} \exp\left(-(c-\mu)^2/2\sigma^2\right). \tag{3.8}$$

Where c are the counts from the camera, μ, and σ are the parameters of the Gaussian distribution, and p is the amplitude which will be equal to $1/2$ in the case of 50% loading probability.
We can estimate the fidelity as follow:

$$F = \frac{1}{2}\left(\int_0^{c_t} P_0(c)\,dc + \int_{c_t}^\infty P_1(c)\,dc\right) \tag{3.9}$$

where c_t is the classification threshold with P_0 and P_1 the distribution modeling the zero and one atom signal, should a unique choice for the threshold c_t exist which classifies the signals and maximizes fidelity.
Another way would be to singularly consider the two probabilities to correctly identify the absence or the presence of an atom, given by

$$F_0 = \int_0^{c_t} P_0(c)\,dc \tag{3.10}$$

$$F_1 = \int_{c_t}^\infty P_1(c)\,dc. \tag{3.11}$$

Then one can adjust c_t to favor one or the other beyond the optimal value for its fidelity, should one want to avoid false positives or not care about the potential miss in detecting some atoms (false negatives). The choice is crucial in the event of a loss during the imaging process. One can adjust c_t to minimize the probability of classifying an atom lost during the imaging process as present.
In the event of a loss occurring during the imaging process, we need to add a contribution to $P_1(c)$. The contribution corresponds to the distribution of the number of photons scattered before the atom is lost. To the $P_1(c)$ distribution, we add an exponential decay, with a maximum for the signal value of one scattered photon. The position of the maximum is counterintuitive, but it is most likely to lose an atom with the first scatter, as reported by [124]. The distribution then decreases until it reaches the one atom signal peak, corresponding to the atoms that are not lost. The exponential loss manifests as a signal connecting the two peaks corresponding to zero- and single-atoms. The distribution is modeled as $\exp(-\chi/N)$ with N being the photons scattered and χ being the loss coefficient. When we calculate the fidelity value, the parameter χ is the parameter we use for the fit.

We measure a peak imaging fidelity of $F = 0.9992(5)$, even for an imaging time of 6 ms. Below this time, the two Gaussian distributions start to overlap, reducing the fidelity value significantly. To estimate the fidelity value, we added the contribution for the atom loss to the model.
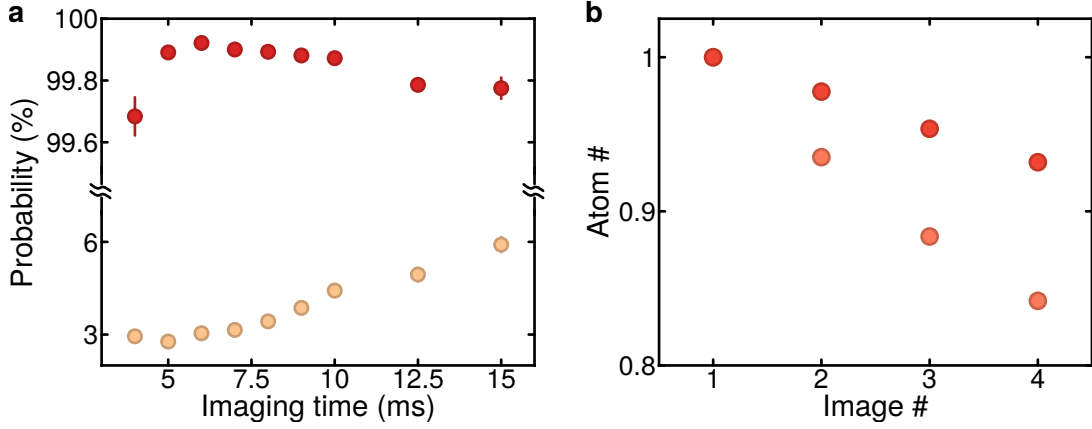
Figure 3.13: Imaging fidelity and loss probability. a Plot of the image fidelity in red and the loss probability in orange, as a function of the imaging time. The binarization threshold is optimized to maximize the image fidelity demonstrating that we can go to an imaging time of 4 ms without significant loss in fidelity. The loss probability is calculated by taking two pictures in sequence and counting the atoms in both. Subsequently, we can identify how many atoms are lost. **b** The number of atoms as a function of the number of pictures taken. We normalize the atom number by counting the atoms present in the first picture.

Survival probability

The loss probability during the imaging process is important for tweezer array platforms. The conservation of the atoms in the traps is critical if one wants to assemble a completely filled system by moving the atoms.

We can define the survival probability S as the probability for an atom present at the start of the imaging process to still be in the trap at the end of the process. The probability can be calculated with direct measurement by taking two consecutive images and checking if the fidelity is $F = 1$. With the images, we can calculate the probability of finding an atom in the second picture on the condition that it is present in the first one.

If the fidelity is $F < 1$, realistically, the evaluated survival probability S_0 from the measurement must be corrected before interpreting it as the actual survival probability. The corrected survival probability can be calculated with the following formula from [124]

$$S = \frac{(F_1 + 1 - F_0)(S_0 + F_0 - 1)}{F_1(F_0 + F_1 - 1)} \tag{3.12}$$

with F_0 and F_1 from Eqs. (3.10) and (3.11). Assuming that both images have the same fidelity.

We calculated the survival probability at different imaging times by taking consecutive images. In Fig. 3.13 we show the estimated loss probability given by $P_{loss} = 1 - S_0$. In this case, we do not apply the correction since our fidelity is approximately equal to one. We observe that the loss probability depends on the imaging time, telling us that we are ejecting the atoms due to the effect of

the imaging light since our occupation lifetime without any cooling light is much longer. As we show in Section 3.3.4, the occupation lifetime of the trapped atoms exposed to our red molasses can explain this loss during the imaging time.

We measure a lower loss probability for the shortest times, with a value of $P_{loss} = 0.027(2)$, with the error given by one standard deviation of the data. After a specific imaging time, we can see that the loss probability increases linearly as a function of time.

3.2.4 Summary and Outlook

We have shown that the use of 1064 nm laser light to produce our traps significantly reduces the effect of vector light shifts in the ground state manifolds generated by the presence of circular polarization coming from the strong focusing of the trapping light. We also see that 1064 nm light produces strong inhomogeneous shifts in the hyperfine states of the $4P_{3/2}$ state manifold. The shifts break down the hyperfine coupling making cooling through red molasses impossible inside the traps. To solve this problem, we apply a modulation technique to chop the trap light and the cooling light, leading to a successful loading and imaging of the trapped atoms. As we demonstrate, our chopped signal is not perfect. This increases the peak intensity needed for the trapping light to have the same average power with regard to the continuous signal by a factor ~ 2.3. The effect limits the number of tweezers that we can generate to 64, given the laser power required for the chopping and the one available.

We can detect trapped atoms with a measured peak fidelity of $F = 0.9992(5)$ for an imaging time of 6 ms. On the other hand, we see that we lose the atoms while imaging with a probability that increases as a function of time. The loss is probably due to imperfections in our cooling technique.

To improve the chopped signal, a Pockels cells solution was tested as described in the master thesis of Robin Eberhard [125]. We can use the Pockels cells to perform the chopping of the MOT light and the trapping light instead of the modulation of the RF power of the arms. The tests have shown that the Pockels cells can be used with different modulation frequencies up to 2 MHz depending on the nonlinear crystal material with a nominal extinction ratio of $> 200 : 1$ and a rising time of a few nanoseconds. The improvement in the chopping can significantly improve the duty cycle for our trapping and cooling light, allowing the peak intensity needed during the chopping to be reduced with a consequent possible increase in the number of the generated tweezers to ~ 100. For this purpose, we will integrate them into the experiment soon.

Regarding the imaging, the problem is the loss present during the imaging time. This parameter is important for the future implementation of rearrangement of the loaded atoms. We need to take an image to find the positions of the loaded atoms before moving them. If we lose atoms in the process, we will not be able to produce a filled array.

A possible solution would be to perform cooling with the Gray molasses tech-

nique while using a single beam on the D2 transition to scatter photons as in reference [110], which yielded very low loss probability during imaging.
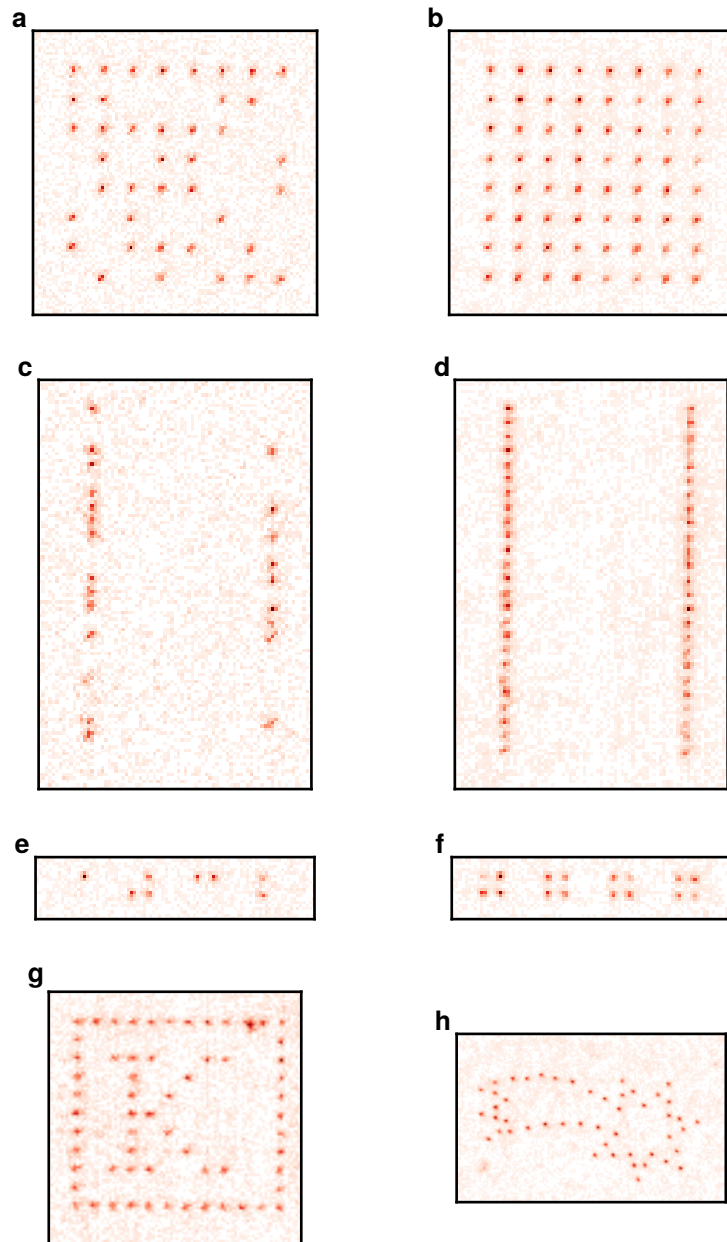
Figure 3.14: Examples of generated arrays. For **a-f**, on the left there is a single fluorescence image, on the right the average of several realizations. **a-b** We can see the 8×8 pattern with $10\,\mu m$ spacing, used in the Raman sideband cooling measurements, see Section 3.5. **c-d** Two columns of 25 traps each, used for the Rydberg dressing experiment, see Section 4.2. **e-f** Four 2×2 blocks, to perform experiments in parallel and increase the statistic per experimental realization. The last two images are averaged fluorescence images of **g** a contoured K, for Potassium39, and **h** a Christmas star, to show the flexibility of the trap generation. Figure adapted from [62].

3.3   Tweezer characterization

We now perform a series of measurements directly with atoms to characterize
our tweezers. The measurements will tell us more about the uniformity of each
trapping potential and their trapping frequencies. From these measurements,
we can infer the dimensions of our traps.

We will show that Talbot-like planes are present even when we generate the traps
with an SLM in the case of packed arrays.

Then we will show measurement for the occupation lifetime of the traps in the
event of only the trap light being present and with the presence of the cooling
light.

3.3.1   Light shift measurement

To measure the light shift between the ground and excited state for each trap,
we chose to probe the transition between the ground state and the D1 transition
since it presents a uniform light shift for all the levels with the linear polarization
of the trapping light. We scan our laser frequency to probe this transition and
compare the in-trap resonance to the free space D1 transition resonance. Experi-
mentally we load our tweezers and then illuminate the atoms with the laser light
coming only from one direction. The light comes from the laser that performs
the gray molasses cooling in free space and is composed of both the cooling and
the repumping light. The atoms are then subjected to strong recoil heating. This
is due to the absorption and emission of resonant light resulting in the escape
of the atoms from the traps. After loading the atoms, we take one picture and
switch the tweezer light from chopping mode to continuous mode. At this point,
we illuminate the atoms for 1 ms using the gray molasses light coming only from
one direction along the x-axis. We chose the illumination time of the gray mo-
lasses light to maximize the contrast. Afterwards, we take a second picture to
check if the atoms survived the push-out. We performed several runs per de-
tuning value to evaluate the probability of keeping the atoms in the tweezers for
varying detuning of the gray molasses laser.

We show the results obtained for single traps in a 5×5 square array with $10\,\mu m$
spacing in Fig. 3.15. We can distinguish the two resolved lines corresponding to
the hyperfine structure of the $4P_{1/2}$ state from the atomic signal. We fit a func-
tion with two Gaussians to the data to infer the resonance frequency for each
tweezer. We justify using a Gaussian function to fit the data by the expected
Doppler broadening and the probing of different light shifts by the position of
the atoms inside the traps. We carry out the analysis for each trap in the array. We
can calculate the light shift from the extracted resonances, knowing how much
the excited state is shifted from the theoretical calculation. The theoretical cal-
culation shows in Fig. 3.8 that the excited state is shifted $U_e = 5.6 \cdot U_g$ compared
to the ground state,

$$\hbar \Delta_{ls} = U_e - U_g = (5.6 + 1)U_g \qquad (3.13)$$

with Δ_{ls} the measured light-shift from the free space resonance. The result
for the mean trap depth is $\overline{U}_0 = 2\pi\hbar \cdot 15.5\,MHz$ with a relative standard devia-

tion of 9% among the tweezers.

Inhomogeneities are probably due to alignment errors of the trapping beam and from aberrations accumulated along the optical path after the SLM and are, therefore, not accounted for in the compensation pattern.
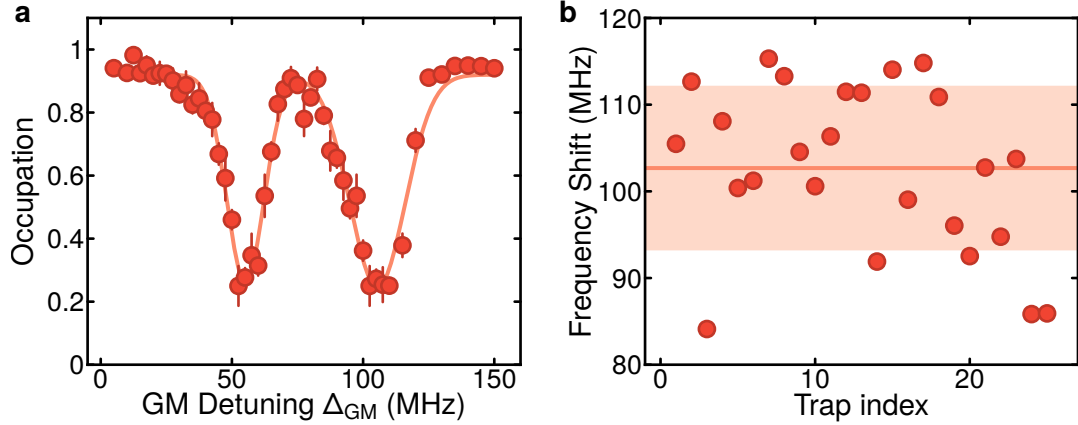

Figure 3.15: D1-line spectroscopy of trapped atoms. a This shows the loss probability of a trapped atom as a function of the detuning of the laser. Two peaks can be resolved corresponding to the transitions to the $4P_{1/2}, F' = 1$ and the $4P_{1/2}, F' = 2$ hyperfine states. The zero in the detuning corresponds to the resonance for the $4P_{1/2}, F' = 2$ state in free space. We fit two Gaussian functions to the data, and the light red line shows the result. We extract the positions of the resonances from the fit. **b** The results from the fit for the $4P_{1/2}, F' = 2$ transition are shown for all the traps in the 5×5 array. The horizontal line is the mean of data, while the shaded region indicates their standard deviation. Errors on the spectroscopy data are given by 1 s.e.m. Errors on the frequency shift are obtained from the fit.

3.3.2 Trap frequency measurement

To measure the trap frequencies of our tweezers, we apply a parametric heating measurement [109]. We implement it by modulating the trap power for different frequencies. When the frequency corresponds to twice the trap frequency, a heating effect occurs, resulting in atoms escaping from the traps. The sequence that we used for the measurements is similar to the one used in the previous subsection, see Section 3.3.1, with the difference being that, instead of using light to push out the atoms, the trap laser power is modulated. We use a function generator to add a sinusoidal modulation to the trap beam intensity using the AOM that stabilizes it. We apply the modulation for 75 ms. Afterwards, we turn off the modulation, and the laser power is abruptly brought down to 7.5% of its original value and ramped up again slowly to 25% in 5 ms. We carry out the operations to increase the contrast of the measurement allowing atoms that have been heated up by the modulation but are still trapped to escape. Then the trap is ramped up again, and a second image is taken.

The results from the measurements are shown in Fig. 3.16. In the vibrational spectrum of a single trap, one can see that two separated peaks are present around the frequency corresponding to the radial direction and are much stronger

than the one for the longitudinal or axial direction. The effect indicates that the tweezers' shape is not perfectly symmetrical. This is probably due to the presence of uncompensated aberrations in our system. We can now compare the theoretical trapping frequencies for a dipole trap with the one we measured. The following formulas give the trap frequencies for the radial and axial trap frequencies

$$\omega_{rad}^{theo} = \sqrt{\frac{4U_0}{mw_0^2}} \quad \text{and} \quad \omega_{ax}^{theo} = \sqrt{\frac{4U_0}{mz_r^2}} \tag{3.14}$$

where w_0 and z_r correspond to the waist and the Rayleigh range of the traps, U_0 is the trap depth, and m is the atomic mass. From the measurements of the trap depth and knowledge of the size of the diffraction-limited spots that should be generated ($w_0 \sim 0.8\,\mu\text{m}$) by our objective, we expect a trapping frequency of

$$\omega_{rad}^{theo} \simeq 2\pi \cdot 160\,\text{kHz} \quad \text{and} \quad \omega_{ax}^{theo} \simeq 2\pi \cdot 68\,\text{kHz}. \tag{3.15}$$

Instead, we measure a mean trapping frequency of

$$\overline{\omega}_{rad} = 2\pi \cdot 141\,\text{kHz} \quad \text{and} \quad \overline{\omega}_{ax} = 2\pi \cdot 19\,\text{kHz}. \tag{3.16}$$

We can now compare the fraction of the theoretically calculated frequencies with the measured mean values

$$\frac{\omega_{ax}^{theo}}{\omega_{rad}^{theo}} = \frac{\lambda}{\pi w_0} \approx 0.42 \qquad \frac{\overline{\omega}_{ax}}{\overline{\omega}_{rad}} = 0.14 \quad . \tag{3.17}$$

The two values differ primarily due to the axial trap frequency, which is a factor three lower than the theoretical value.
From the measurement we can calculate a Rayleigh range of $z_R = 6.8\,\mu\text{m}$ which is a factor three larger than the theoretical one for a perfect Gaussian beam $\pi w_0^2/\lambda = 2\,\mu\text{m}$. The discrepancy was also observed in reference [126], but not in such dramatic proportions. One reason for this difference is the approximation made by considering the optical tweezers as simple Gaussian beams. To calculate an exact profile, one needs to consider the diffraction of the input beam. The second reason is the presence of aberrations. The presence of two resolved peaks in the radial direction also points to the presence of uncompensated aberrations.

3.3.3 Talbot-like traps

A problem with tightly packed tweezer arrays is the control of the intensity pattern away from the trap plane. As observed by Talbot and explained by Rayleigh [127], intensity patterns of spots arranged in regular periodic structures replicate themselves after a propagation distance of $z_T = 2a^2/\lambda$, with a the pattern spacing. The pattern can replicate itself also at intermediate distances but shifted by
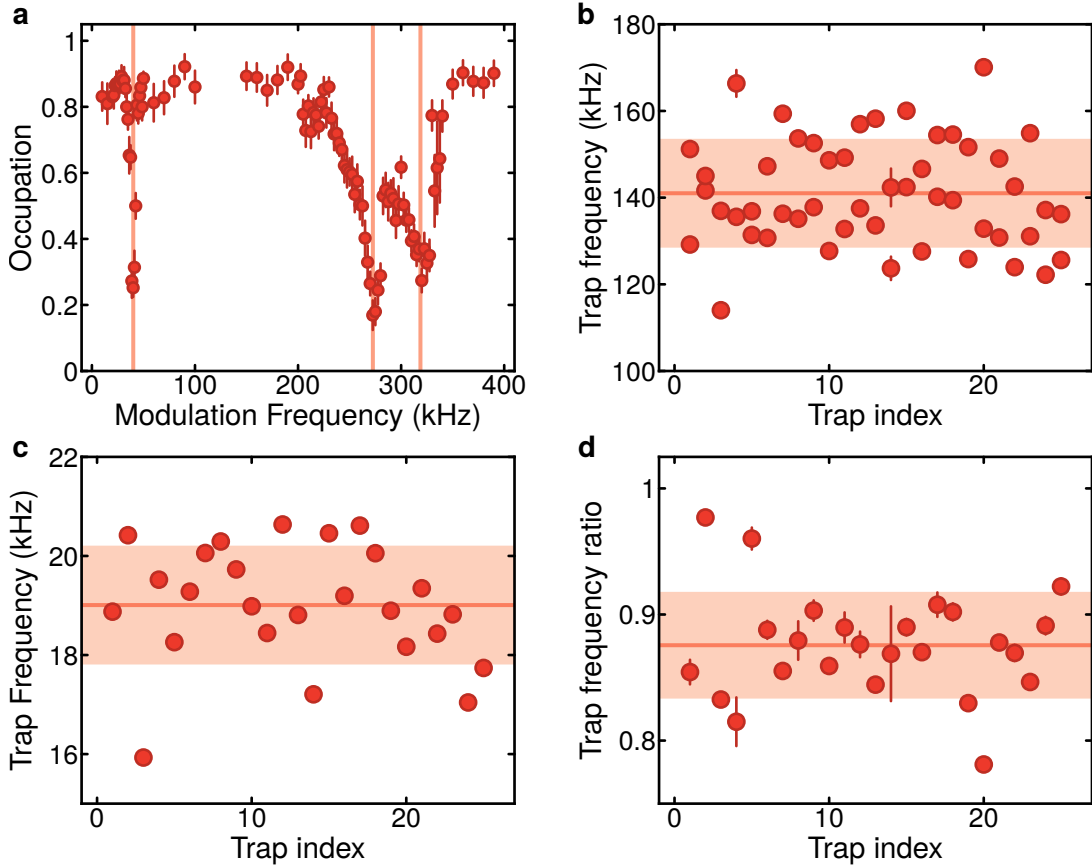
Figure 3.16: Parametric heating measurement. Results for the modulation spectroscopy for 5×5 array with $10\,\mu m$ spacing. **a** Typical parametric heating spectrum for a single trap. We show the probability of finding a trapped atom after the modulation time as a function of the modulation frequency. The resonances are fitted with Gaussian curves to find the resonance, indicated by the light red vertical lines. The lowest dip is for the longitudinal trapping frequency, while the two higher dips are for the radial frequency. **b** The plot of the fitted radial trapping frequencies. The mean of the data is indicated by the horizontal line, while the background indicates their standard deviation. The fact that two resonances are present indicates an asymmetry in the single trap along the radial direction. **c** The plot of the fitted longitudinal trapping frequencies. The mean of the data is indicated by the horizontal line, while the background indicates their standard deviation. **d** We plot the ratio of the two radial trapping frequencies. The mean of the data is indicated by the horizontal line, while the background indicates their standard deviation. We always divide the smaller value by the bigger one, showing the difference between the two.

a fraction of the pattern spacing. The effect was used in reference [128] for the realization of large-scale systems in the context of single atom tweezers.

In our experiment, we do not expect to see an exact Talbot effect due to the relative random phase of the light field that generates the tweezers, which breaks the required periodicity. Nonetheless, we can detect the presence of atoms trapped further away from the trapping plane in the case of dense and tightly spaced arrays $a < 10\,\mu m$. If we use single lines of traps even with close spacing, the effect is not detectable. The atoms trapped outside the imaging plane produce

more background signal around the traps' positions. We apply a Fresnel lens to the SLM pattern to detect the atoms trapped outside the trapping plane through imaging. With the Fresnel lens, we shift the traps' plane in the vertical direction, away from the imaging plane, to check the presence of atoms at this position. In this way, we can take pictures of atoms that are (possibly) trapped outside the trapping plane as in Fig. 3.17. By increasing the distance, the atomic signal from the trapping plane is smeared out, and at the displacement distance of 17 μm, we can see that another clear signal appears. The value corresponds to a fraction three of the Talbot distance of ≈ 50 μm for this pattern. Also, some features suggest the presence of trapped atoms between the two positions but with a lower probability. Signals are detected at a few Rayleigh ranges $z_r \approx 2$ μm away from the tweezers plane, which results in a significant background signal during imaging.
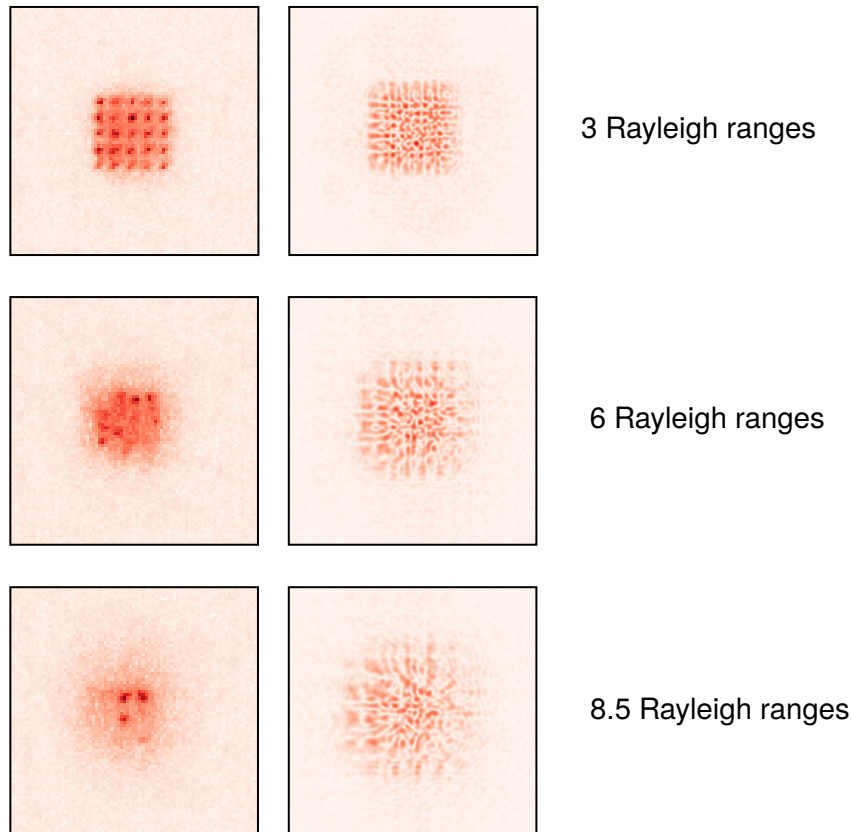
Figure 3.17: Talbot-like effect. Averaged pictures of the atoms trapped outside the trap plane on the left and calculated intensity landscape at the same distance propagating the used phase pattern. We apply a Fresnel lens on the SLM to shift the focus point for the traps, such that there is a shift between the image plane and the trap plane. We can observe a signal for several Rayleigh ranges from the trap plane up to 8.5 Rayleigh ranges.

3.3.4 Lifetime Measurements

An essential parameter for the experiment is the atomic occupation lifetime of our tweezers. The occupation lifetime we refer to here is when no cooling light is applied to the trapped atoms. We calculate the occupation lifetime from the probability of a trapped atom escaping and being lost from a trap. This probability can be defined for a time t as $1 - \exp(-t/\tau)$, where τ corresponds to the occupation lifetime of a single atom. The lifetime value is crucial for all the experiments that will be carried out since it can severely limit the total length of the experimental sequence and the coherence of the processes involved. As previously noted, this lifetime becomes more critical with the increase of the system size and is already limiting current experiments [23, 24].

The measurement of the lifetime τ is as follows. We load one atom per trap, take one image of the trapped atoms, and then the atoms are held in the traps for varying times. In our case, we can measure the lifetime in various conditions. In the case of traps being continuously on the measured lifetime per atom is $\tau_{const} = 80 \pm 8\,\mathrm{s}$. On the other hand we measure a lifetime of $\tau_{chop} = 29 \pm 1.7\,\mathrm{s}$ in the case of continuous chopping of the traps, as we showed in Fig. 3.18. For most of the experiments described in this work, we only need to chop the traps for the loading and the imaging parts of the experimental sequence, which takes $\approx 200\,\mathrm{ms}$ at the beginning of the sequence and $\approx 40\,\mathrm{ms}$ at the end of it, when the second image is taken. These measured lifetimes are higher than the ones seen in previous experiments [23, 24] and come close to the lifetime measured for more recent experiments with alkali-earth atoms [117, 118].

In cold atom experiments, the occupation lifetime is limited by collisions with atoms from the background gas at room temperature present in the vacuum chamber and by the off-resonant scattering of the trapping light. This background gas is mainly made up of hydrogen atoms and molecules. Usually, the collision with hydrogen provides enough energy to an atom for it to escape from the trap [129]. The collision rate of such an event is directly dependent on the residual pressure in the UHV chamber. Our chamber design used several differential pumping stages combined with a Zeeman slower, which allows a clean vacuum in the experimental chamber. Other experiments that load their MOT directly from a background gas of alkali atoms significantly reduce the vacuum quality. The loading from the background pressure is what limits their occupation lifetime to a few seconds. Experiments that present differential pumping stages observed occupation lifetimes of several tens of minutes, agreeing with the estimated loss rates caused by background gas collisions.

To further increase the occupation lifetime by reducing the background collisions requires more complex experimental designs. Using a cryogenic system can significantly increase the occupation lifetime by reducing the background pressure in the UHV chamber by a few orders of magnitude. The trapped ion community has already built experiments at cryogenic temperatures for this reason [130]. Recently one cold atom experiment, see reference [131], reported the first results on the application of this technology, which showed an occupation lifetime for atoms in optical tweezers two orders of magnitude longer than standard experiments.

The trapping light can limit the occupation lifetime from off-resonant scattering of photons and limit any coherent experiment. In the case of off-resonant scattering, the heating rate is given by $dT/dt = 1/3 \cdot T_{recoil} \cdot \Gamma_{scatter}$ [101], where $T_{recoil} = \hbar^2 k^2 / m / k_B$ with $k = 2\pi/\lambda$ and m the atomic mass, $\Gamma_{scatter}$ is the off-resonant scattering rate, the factor $1/3$ comes from the energy redistribution along 3-dimensions. In our case the heating rate is calculated to be $dT/dt = 1.2\,\mu K/s$ with a recoil temperature of $T_{recoil} = 433\,nk$ from a trapping photon and a scattering rate of $\Gamma_{scatter} = 2\pi \cdot 1.3\,Hz$ at a trap depth of $k_B \times 1\,mK$. Given this heating rate, the occupation lifetime for a single atom should amount to 10 minutes, not concurring with our experimental result, thus indicating that we are not limited by the off-resonant scattering.

Parametric heating from the trapping laser is another limiting factor, which occurs when there is intensity noise or modulation at twice the trap frequency. However, this was not measured [109]. We can estimate the parametric heating by characterizing the laser's relative intensity noise (RIN) spectrum. The intensity stabilization loop has a limited bandwidth with a typical cut-off modulation frequency at 100 kHz, close to the trap frequency of our tweezers. We have to rely on the use of intrinsically low-intensity noise sources or use more complex stabilization schemes [132]. In our case, from the measured RIN noise, we estimate a heating rate of 100 nK/s, not limiting the atom lifetime.

Another noise source can be the intensity and pointing noise which the SLM can produce [133].

To conclude, using our estimations, we can state that the occupation lifetime is limited not by the trapping laser but by background gas collisions since the measured loss rate agrees best with this loss mechanism.
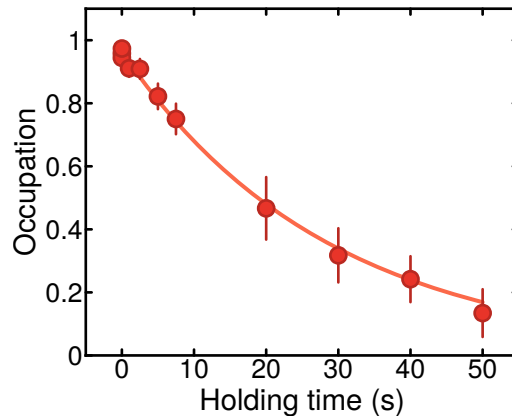
Figure 3.18: Occupation lifetime with chopping. Occupation lifetime of the atoms while the trapping light is continuously being chopped during the holding time. The trap depth is the same as when we do not chop the trapping light. We measure the occupation for different holding times by taking two images, one before the holding and one after, to identify the loaded traps and then count the losses. The exponential fit of the data produces a lifetime of $\tau = 29 \pm 1.7\,s$.

Now we have shown that the occupational lifetime of the atoms inside the traps without any active cooling applied is good enough to perform experiments with a duration of a few hundreds of milliseconds. We can now check the life-
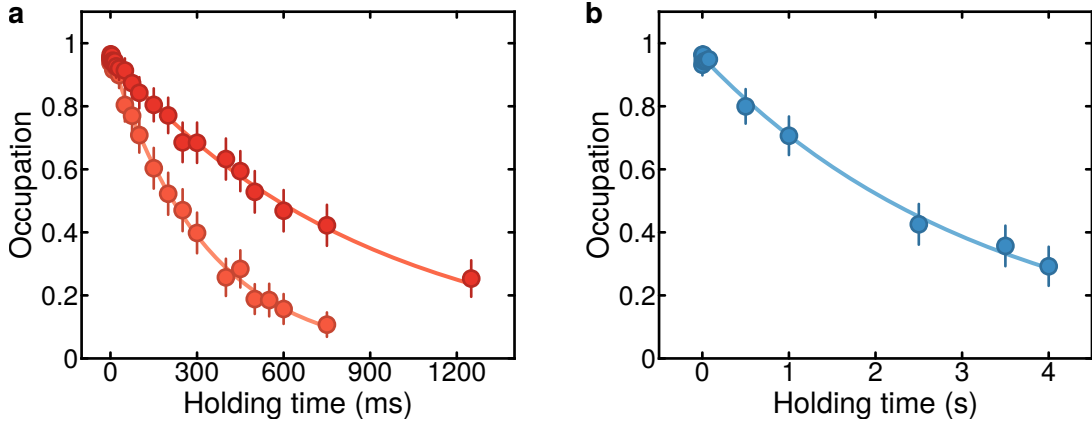
Figure 3.19: Occupation lifetime under different cooling methods. As for the measurement of the chopping lifetime, we take two pictures before and after the holding time. **a** Occupation lifetime with the red-molasses cooling. In light red is the lifetime data with a trap depth of $\approx k_B \times 1\,\text{mK}$, in dark red is the lifetime data with twice the previous trap depth. **b** We show the occupation lifetime in event of the application of gray-molasses cooling at a trap depth of $\approx k_B \times 1\,\text{mK}$. The traps were continuously on.

time when we continuously apply cooling to the trapped atoms. The lifetime under cooling is relevant for the imaging losses that we have seen before in Section 3.2.3 and for the deterministic loading technique that we have attempted to implement reported in Section 3.4.

We measure the occupation lifetime if we apply the red molasses cooling technique or the gray molasses one. We apply red molasses cooling in the same way as in Section 3.2. We measure an occupation lifetime of $\tau_{RM} = 332 \pm 7\,\text{ms}$ in the case of a $k_B \times 1\,\text{mK}$ trap depth. This result is consistent with the losses that we see occurring during the imaging time shown in Section 3.2.3. In the event that we increase the trap depth to $k_B \times 2\,\text{mK}$, the occupation lifetime with red molasses cooling is also doubled to $\tau_{RM} = 895 \pm 19\,\text{ms}$. The data and the fits are shown in Fig. 3.19.

In the event of the gray molasses cooling technique, we observe a lifetime that is an order of magnitude higher than the red molasses cooling in the case of the same trap depth of $k_B \times 1\,\text{mK}$. The measured lifetime is $\tau_{GM} = 3.3 \pm 0.13\,\text{s}$, shown in Fig. 3.19. Even with this difference in lifetime, the gray molasses cooling cannot be used for the imaging. The reason is due to two main differences. The first one is that the gray molasses cooling relies on a dark state that does not scatter light, reducing the number of collected photons. The second one is the difference in the amount of cooling light needed, which influences the background level of the camera. In the case of red molasses, the power level of the cooling light is an order of magnitude lower, making the imaging of trapped atoms possible.

3.3.5   Summary and Outlook

This section shows that the traps are subjected to optical aberrations in the beam path. These aberrations cause inhomogeneities in the trap light shift of up to 10% compared to the mean. In addition, they lead to the formation of slightly elliptical traps in the radial direction. The ellipticity is shown by the measurement of two distinct trap frequencies along the radial direction.

We have also measured the occupation lifetime with and without the presence of cooling light. Without applying cooling light, the traps can hold the atoms for over a minute. This lifetime surpasses the occupation lifetime measured for some tweezers experiments [23, 24] by one order of magnitude.

The limitation to the occupational lifetime is a result of the residual background gas pressure. The number of components and materials that we placed inside the vacuum chamber as shown in Fig. 2.2 can explain the higher residual background pressure.

A new experiment with optical tweezers, operated at cryogenic temperatures to reduce the background vacuum pressure, greatly improved the occupation lifetime compared to current experiments, see reference [131]. The design is similar to previous experiments built for ions [130]. The experiment produced occupation lifetimes two orders of magnitude longer than the standard ones.

We also measured the occupation lifetimes of the trapped atoms while they were illuminated by cooling light. The limited lifetime for the red molasses technique involves imaging and explains the loss events occurring during the imaging process.

To avoid being limited by the strong light-shift inhomogeneity of the array for the Rydberg dressing experiments in Section 4.2.2, we implemented Raman sideband cooling on the trapped atoms. We give a summary of the Raman Sideband Cooling implementation in Section 3.5. After cooling the atoms, we can lower the trap depth U_0 down to $0.005 \cdot U_0$, scaling the relative difference in light-shift between the traps by the same amount.

The presence of Talbot-like traps, as we show, determines the trapping of atoms outside of the imaging plane. The extra atoms can be a problem in the experimental control and detection stage since it can allow the uncontrolled presence of atoms in the interaction range and increase the background level of scattered light, increasing the possibility of false detection of an atom. There are several ways to solve this issue. A solution could be to load the atoms from an elliptical dipole trap which has a waist of $w \sim 3\,\mu m$ along the z-axis, less than the measured Rayleigh length of the traps. Then the atoms are only present in the trap plane and cannot be loaded into the Talbot-like traps.

Another option would be to apply Raman Sideband Cooling to the trapped atoms and then lower the trap depth $U_0 \simeq k_B \times 1\,mK$ down to $0.005 \cdot U_0$. The atoms present outside the traps plane will not be cooled as efficiently, and once we lower the depth of the traps, they will escape leaving only the atoms in the traps plane.

To improve the uniformity of the array, we could use the data acquired by the light shift spectroscopy and trap frequency measurements. This idea was tested in reference [92]. We can generate a pattern and then take the measurements. With the measurements results, we can create a new aberration correction mask or change the individual trap intensities to account for all the imperfections along the optical path. Subsequently, another pattern can be generated. We should repeat this process until the inhomogeneity of the array is below a certain threshold. The process is time-consuming since it requires measurements with atoms before generating a new array, but the whole process could be automatized and run overnight. We have not yet implemented the correction using atomic feedback, but it is included in the plans for future improvements.

3.4 Deterministic loading of Potassium atoms in optical tweezers

The main problem that limited the use of optical tweezers for neutral atoms is the 50% loading probability of a single atom due to parity projection [20, 82], which does not allow unitary filling of the arrays.
A turning point for this problem was reached with the successful reorganization of the atoms in the tweezers with the movement of single atoms and realize completely filled arrays, see references [23, 24, 93, 134]. Even with the rearrangement of the atoms, increased loading probability is essential for scaling up the number of atoms in the array. The sorting of atoms was carried out by moving one atom at a time for a moderately small system of ~ 50 atoms. However, when the number of atoms is increased, we need clever schemes for atom movement. Such a scheme was used recently with the simultaneous movement of several atoms to reduce the sorting time, see reference [92].
Prior to the successful rearrangement attempts, the primary strategy that was explored made use of the same kind of molecular potentials, which caused the parity projection limiting the single atom loading probability. The parity projection was already observed at the beginning of the optical dipole trapping efforts of the cold atom community, see reference [135].
Experiments have managed successfully to exploit the repulsive branch of molecular potentials to reduce the effect of the parity projection loss and even enhance the loading probability of single atoms deterministically. Such experiments were able to reach a loading probability $\approx 90\%$ with Rubidium atoms [83, 136, 137].

3.4.1 Light assisted collisions

The molecular potentials can be described with a repulsive van-der-Waals interaction C_6/d^6 in the event of both atoms being in the S-state, and with a dipolar interaction, C_3/d^3, which can be attractive or repulsive in the case one atom is excited to a P-state [138–140], where d is the inter atomic distance. We explain in Section 4.1 the different interaction behaviors which depends on the parity of the states involved in the context of Rydberg states, which can be generalized for the lower states too. With dipole-dipole interaction it is only possible to couple from the ground states to the combination $|4S_{1/2}, 4P_{1/2}\rangle + |4P_{1/2}, 4S_{1/2}\rangle$ which

is responsible for the repulsive potential. This is true at large distances, but on shorter distances mixing occurs which allows optical coupling to the attractive potential [138].

In the case of 39K atoms, the C_3 and C_6 coefficients have been experimentally determined. In the case of atoms in the S- and P-state, they interact through a dipolar interaction with $C_3 = \pm 2\pi\hbar \cdot 51.68\,\text{kHz}\,\mu\text{m}^3$ [141]. In the case of both atoms in the S-state the interaction is of the van-der-Waals type with $C_6 = 2\pi\hbar \cdot 0.587\,\mu\text{Hz}\,\mu\text{m}^6$ [142].

Given these interactions, there will be a definite distance called Condon radius $R_c = (C_3/\hbar\Delta)^{1/3}$, where the transition is resonant with the driving field. In the case of two atoms close to each other, the detuning to the bare transition to resonantly excite one atom can be quite large.

In the case of red-detuned light, the two atoms are coupled to the attractive branch of the pair-state potential. Then, both are accelerated towards each other by the attractive potential. The atoms can then emit a photon with a slightly lower frequency, bringing both atoms back to the S-state. The whole process provides both atoms with a large amount of kinetic energy and can lose the atoms from the trap during cooling in the collisional blockade regime. This pair-loss effect is what limits the loading efficiency to 50%. This effect is also known as parity projection [111]. A schematic of the process is given in Fig. 3.20.

The attractive molecular potential produces resonances which we do not take into account [143] since we are considering relatively small detunings compared to the binding energy, and we, therefore, consider the density of resonances as a continuum.

With small detunings, the slope of the attractive potential allows for spontaneous emission before the pair gather significant relative acceleration. The energy acquired by the pair in this collision might not be large enough to cause the loss of both atoms. It has been observed that the energy distribution allows the loss of a single atom. The loading probability can reach the value of 60% by cooling with red-detuned light in appropriate conditions as reported by [83, 144, 145].

With blue-detuned light, the atoms are coupled to the repulsive interaction pair-state potential branch. In this configuration, the atoms gain a defined amount of kinetic energy during a collision. The amount is fixed by the detuning of the laser $\hbar\Delta_{blue}$. The blue detuned light provides optical shielding from the detrimental red-detuned events. Knowing the trap depth and the excited state light shift, the detuning of the laser can be set to be equal to the trap depth $\hbar\Delta_{blue} \simeq U_0$. The maximum kinetic energy gained by the atomic pair is then only enough to expel a single atom. A schematic of the process is depicted in Fig. 3.21.

Previous works successfully increased the loading probability by adding a blue detuned beam to the system [83, 136]. As said before, the blue detuned beam couples the repulsive molecular potential and sets the maximum amount of gained kinetic energy to let one atom escape.

The probability of occurring depends on the Landau-Zener transition for an atom to go through the avoided crossing generated by the coupling of the blue light. For the shielding process to occur, we need to care for the following prob-
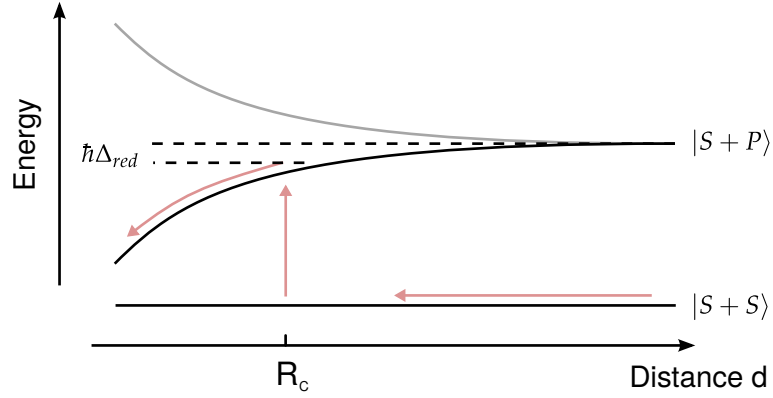
Figure 3.20: Red-detuned light assisted collisions. Schematic model for the red-detuned light-assisted collisions. On the right, the pair states involved are shown. Δ_{red} indicates the detuning of the external laser from the free space transition. At a distance, $d = R_c$ one of the atoms is resonantly excited, and the two-atom system is subjected to the attractive molecular potential curve. The attractive potential accelerates the two atoms until a spontaneous decay event happens, increasing the kinetic energy of the pair.

ability

$$P_{AD} = 1 - P_{LZ} \tag{3.18}$$

which is the probability to adiabatically follow the repulsive potential curve, given the coupling of the beam. Where $P_{LZ} = \exp\left(-4\pi\hbar\Omega^2/2\alpha v\right)$ with Ω the coupling, v the relative center of mass velocity and α the slope of the potential at the Condon point.
The second step requires the atoms to move back on the potential line not to follow the potential line but to go through the avoided crossing. With the crossing and the decay to the ground state, the atoms gain the energy set by the detuning. The probability for the atoms to cross diabatically is given by P_{LZ}. The probability for both processes P_{BS} to happen is given by the multiplication of the probabilities resulting in

$$P_{BS} = P_{LZ}(1 - P_{LZ}). \tag{3.19}$$

The process described before transfers the energy set by the detuning Δ_{blue}. The transferred energy is not the only important factor determining a single atom's escape from the trap. The direction of the two atoms' velocities needs to align along the center of mass axis to maximize the energy transfer. In the event of an unfavorable velocity configuration, the atoms need to be cooled down and undergo another collision event. It is critical that both cooling and shielding work at the same time.

In our case, the extra light shift of the P-states complicates the problem slightly. We implemented the chopping to circumvent it when loading and imaging, as

a

b
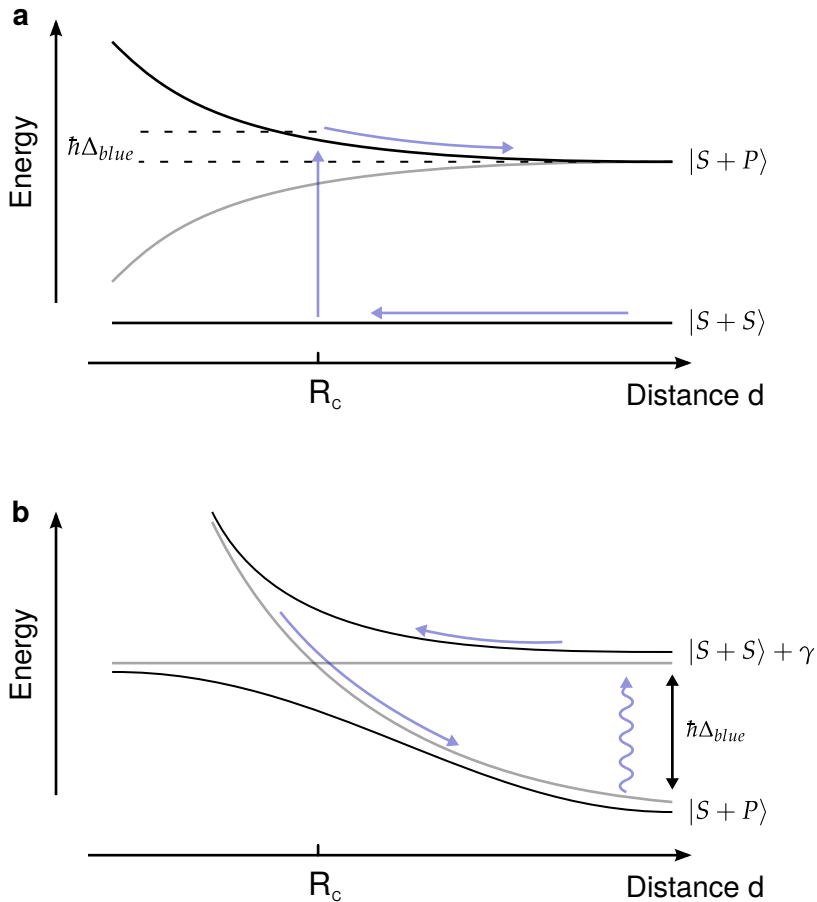
Figure 3.21: Blue-detuned light assisted collisions. In the presence of blue-detuned light, one of the atoms undergoes excitation at a distance $R = R_c$, but in this case, the two atoms are subjected to a repulsive pair potential. The two atoms travel along the curve until the turning point given by their initial kinetic energy. Traveling back, they can pass the Condon point R_c again. They can follow back to the ground state branch adiabatically or diabatically pass the point and remain in the excited state branch. The first process produces a shielding effect, not allowing two atoms to get closer. The second process can be used to transfer a controlled amount of kinetic energy determined by the detuning of the laser $\hbar\Delta_{blue}$. In the lower panel, the process is shown in the dressed picture removing the photon energy.

shown in Section 3.2. By doing so, we set ourselves on a different path, with a method which has been recently demonstrated [137], where only blue detuned light is used for cooling during the loading as well as for the collision process. The blue detuned light is provided using the gray molasses technique for cooling, where all the beams are blue detuned to the addressed transition.

3.4.2   Loading from gray molasses

We have confirmed that we cool atoms by gray molasses light in the traps by measuring the lifetime of the atoms in appropriate cooling conditions with respect to the trap light-shift, see Section 3.3.4. We modified the experimental sequence in

the following way to test loading with gray molasses. During the red molasses cooling phase of our sequence, we change the detuning of the gray molasses light to the value desired for the deterministic loading in about 25 ms. Subsequently, the red molasses light is switched off, and the gray molasses light is switched on again with the trap light for the tweezers. The gray molasses light is kept on for 30 ms to load the atoms in the traps in this configuration. It is possible to efficiently cool atoms on a wide range of detuning values for the gray molasses light as shown in [72]. This feature allows us to perform cooling in free space and inside the tweezers at the same time. After this time, we switch off the blue detuned light.

To remove any possible double-loaded trap, we apply a pulse of red molasses light while chopping the traps to perform parity projection for 10 ms. In the case of working deterministic loading, the pair projection pulse should not have any effect, keeping the loading probability above the pair projection limit.

We simultaneously performed the experiment scanning the trap depth of the tweezers, and the detuning of the gray molasses light Δ_{GM}. We scanned the trap depth from the average value measured in Section 3.3.1 of $U_0 = 2\pi\hbar \cdot 15.5$ MHz to $1.5 \times U_0$, together with the gray molasses detuning Δ_{GM}. The results are shown in Fig. 3.22.

One can distinguish two regions in the scan. The first one is where the detuning is below the trap light shift. The GM cooling does not correctly work on the bottom left, and light can be resonantly scattered, reducing the loading probability. The second region is on the top right, where the cooling of the GM light works, and we can see that we load atoms in the traps. Where the detuning reaches a value such that the gained kinetic energy is more than enough to expel a pair of atoms out of the trap, one reaches the parity projection regime again with a loading probability of $\approx 50\%$. We can see the increase in the loading probability exceeding the pair projection limit between these two regimes. The maximal average loading probability that we have measured is $\approx 60\%$. If we check single tweezers, we reach a peak loading probability of $\approx 70\%$. The difference between the average value and the single tweezer value is expected due to the inequality in trap depth as shown in Section 3.3.1. This difference results in a shift of the loading probability profiles and a blurring in the averaging of them.

3.4.3   Loading from dipole trap

Since the atoms are not confined during the loading, the density of the atomic cloud decreases, which in time can result in a lower loading probability. In the previous sequence, the atoms are only cooled by the red molasses while changing the parameters for the gray molasses light. To verify this, we try to load the atoms in a different configuration that should yield a higher atomic cloud density when loading into the tweezers.

After performing gray molasses cooling, the dipole trap that we have along the x-axis is ramped up and loaded with atoms while the GM light is still on. After this, we switch off all cooling lights, and the parameters for the GM light are changed to perform the deterministic loading. We slowly ramp up the tweezers'
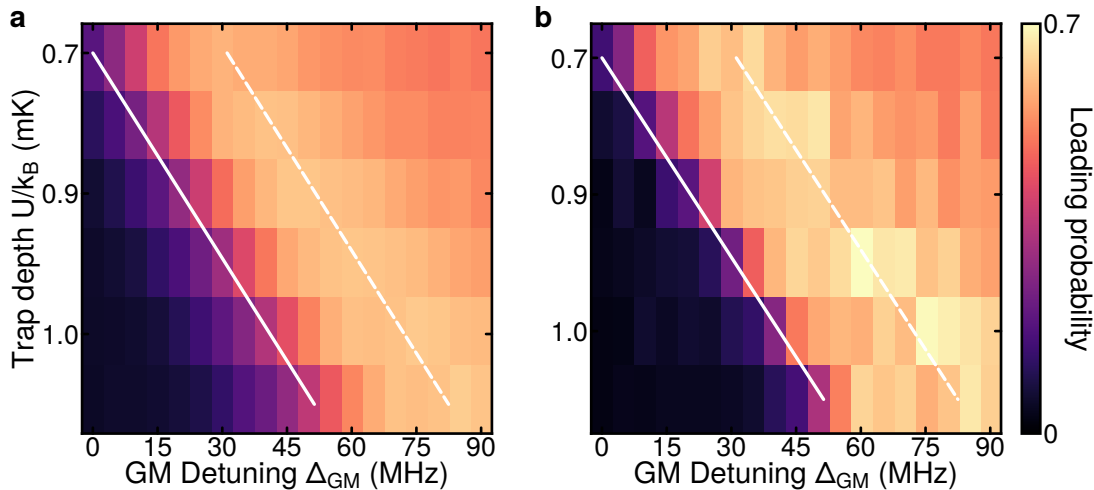
Figure 3.22: Gray-molasses loading. Loading probability with gray-molasses cooling as a function of trap depth and detuning of the gray molasses Δ_{GM}. The solid white line indicates the position of the atomic resonance, the white dashed line indicates the point where the detuning is equal to twice the trap depth $\hbar\Delta_{GM} = 2 \cdot U_0$. **a** Average loading probability over the whole 5×5 array. **b** Loading probability for a single trap, in this case the one that presents the highest value for the loading probability.

power to accommodate the atoms inside. This is possible since we are not limited by the fast reduction of atomic density thanks to the dipole trap. Subsequently, the tweezers should be loaded with one or more atoms. Once we finish ramping up the tweezers, we turn off the dipole trap and let the remaining atoms fly away. After 20 ms, we switch on the GM light to perform the deterministic preparation of one atom per trap.

We perform the same scan as for the previous experiment, scanning both the trap depth of the tweezers U_{trap} and the detuning of the GM light Δ_{GM}. This experiment produces the same results as the previous one showing that the atomic density does not limit us for our deterministic loading, as we can see in Fig. 3.23. We observe an average loading probability of $\approx 62\%$ and a maximal single tweezer loading probability of $\approx 70\%$.

The result tells us that the initial atom cloud density does not limit us, but the deterministic loading mechanism does not work well in these conditions.

3.4.4 Summary and Outlook

We have attempted deterministic loading of optical tweezers in the same configuration as Brown et al. [137]. They use the light from gray molasses cooling to load atoms deterministically into optical tweezers. However, we cannot reach the same value for the loading probability that they can reach with Rubidium. One reason for the lower loading probability is the trapping light. In our experiment, we generated the optical tweezers using 1064 nm laser light due to the availability of high power systems. However, the extra light shift generated in the $4P$ states is a problem for the loading of atoms, making it challenging to
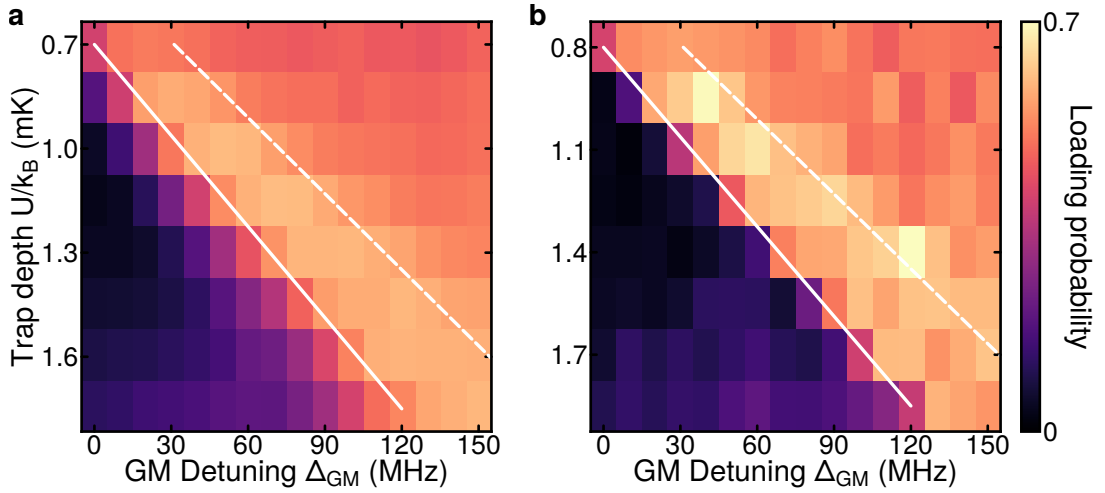
Figure 3.23: Dipole trap loading. The atoms are loaded from the dipole trap along the x-axis without any cooling. We carry out the deterministic preparation of single atoms with the gray molasses light. The measurement is the same as the one in Fig. 3.22. The loading probability as a function of trap depth and detuning of the gray molasses Δ_{GM}. The solid white line indicates the position of the atomic resonance. The white dashed line indicates the point where the detuning is equal to twice the trap depth $\hbar\Delta_{GM} = 2 \cdot U_0$. **a** Average loading probability over the whole 5×5 array. **b** Loading probability for a single trap, the one that presents the highest value for the loading probability.

satisfy conditions for laser cooling in free-space and inside the tweezers simultaneously.

Another factor to consider is the level structure of the atomic species used. A very well resolved hyperfine structure is necessary to isolate one single interaction potential used in the collisional process. In the previous attempts, Rubidium atoms were predominantly used. They present a well-isolated hyperfine structure that minimizes the probability of off-resonant red-detuned, far blue-detuned, or spin-changing light-assisted collisions, resulting in the loss of both atoms. The same is more challenging to apply in the case of Potassium39 since its hyperfine structure is not as well isolated.

Unfortunately, the extra light shift is probably the main cause of the insignificant increase in loading probability. The atoms explore different positions in the trap, broadening the detuning where the collisions occur. The shift on the $4S_{1/2}$ states is maximally $\sim 18\,\text{MHz}$, which results in a shift in the $4P_{1/2}$ of $\sim 100\,\text{MHz}$. The total light-shift can strongly vary depending on the atoms' position given the $\alpha_e / |\alpha_g| = 5.6$ factor of the excited state light-shift with respect to the ground state one. That is different from previous attempts with Rubidium, [83, 137, 146], where they use light closer to resonance, between 810 nm to 850 nm, which produce a shift for the P states that is a fraction of the ground state one.

In Brown et al. [137], they successfully increased the loading probability for Rubidium atoms into optical tweezers using gray molasses to induce deterministic loading. They note that it is critical to have a significant increase in loading probability to define precisely the energy transmitted to the pair of atoms

$\hbar \left(\Delta_{blue} - \delta_0 \right) / U_0 < 2$, with δ_0 the maximal light shift on the ground state from the trap. In our experiment, we can easily exceed this limit with atomic motion in the trap due to the strong light-shift in the excited states.

Recently, another experiment that uses Potassium39 atoms with optical tweezers successfully increased the loading probability into the tweezers up to 76%, see Angonga et al. [110]. They applied the same method we used - loading with the gray molasses light. The main difference is the use of 780 nm light to generate the traps. At this wavelength the light shift exerted on the $4P_{1/2}$ manifold is only $\alpha_e / |\alpha_g| \sim 0.45$ compared to the ground state. The inferior excited state light-shift reduces by a factor ~ 5 the variation of $\hbar \Delta_{blue}$ from the atomic motion inside the tweezer. They also managed to have an occupational lifetime under GM cooling of ~ 120 s, a value much larger than the one that we note in Section 3.3.4. Their result shows that a smaller differential light shift between a ground and excited state better controls the energy transmitted by the gray molasses light to load single atoms deterministically.

We can try two possible approaches that should lead to higher loading probabilities:

- We are already preparing a setup for the movement of single atoms between traps to produce filled arrays. The setup is composed of two crossed AODs and uses 795 nm light to make the trap that moves the atoms. The design of the setup can be found in the thesis of Robin Eberhard [125]. We can also create a static square array with the same setup and use it to initially load the atoms. In this way the excited-state light shift is reduced to a fraction of the ground state one $\alpha_e / |\alpha_g| \sim 0.5$, compared to the factor $\alpha_e / |\alpha_g| = 5.6$ with 1064 nm light, as shown in Fig. 3.8. After the loading, we can transfer the atoms to the traps generated by the SLM. It has been shown that the inhomogeneity in trap depth can be reduced with an AOD [117] down to a few percent, and the transfer from two sets of traps can result in negligible losses [32].

- Another approach would be to use a magic wavelength for the $S_{1/2}$ and $P_{1/2}$ transition for the trapping, zeroing the differential light shift between the two states. Allyu et al. [147] have already tried this idea using Sodium atoms with the same deterministic loading technique. They also reach a loading probability of $\sim 80\%$.

  To use it in our experiment, we could exploit the $4S_{1/2}$ to $5P_{1/2}$ transition, which presents a magic wavelength at ~ 1054 nm as shown in [148]. To do so, we need to change the seed laser for our ALS amplifier and implement GM cooling over this transition with a 405 nm laser, where cooling techniques had already been tested [149].

3.5 Raman sideband cooling and atom interferometry

Now that we have shown how to load and image atoms in our tweezers, we need to introduce the three techniques we have implemented to perform experiments. First, we need to prepare the atoms in a defined ground state and transfer the atoms between two ground states coherently. These two techniques will allow us to perform interferometric experiments, with the interaction between the atoms provided by Rydberg dressing as in references [58–61]. We will show an example in Section 4.2.2.

Moreover, the experiments we want to perform need to keep the atoms trapped, and the inhomogeneity of the traps can be a fundamental problem in the realization of experiments. We subsequently implemented Raman Sideband Cooling to cool down the trapped atoms to their motional ground state. We could then reduce the trap power by a factor of 200, reducing the difference in light-shift between the traps by the same factor.

For details about the laser setups and characterizations, see the thesis of Nikolaus Lorenz [62].

3.5.1 State preparation

We will prepare the atoms trapped in our tweezers in a well-defined Zeeman m_F sub-state that we can use to perform Raman Sideband Cooling, as described in the following Section 3.5.2 or also as one of the states for a qubit. The states that are usually used are the following: stretched states $F = 2, m_F = \pm 2$ with the $F = 1, m_F = \pm 1$ or the states with $m_F = 0$ which present a much lower sensitivity to magnetic fields as in reference [54]. We decided to prepare the atoms in the stretched states. The reason behind the choice is the maximization of the coupling to Rydberg states. The $m_F = \pm 2$ states have a projection of the total angular quantum number of $m_J = \pm 1/2$, the same basis used to define the Rydberg states.

The scheme used is shown in Fig. 3.24 for the $m_F = +2$ state, similar to references [150, 151], it can be easily used also for the $m_F = -2$ state by rotating the quantization field by 180°. A laser field is applied to couple the ground state $F = 2$ manifold to the $F' = 2$ with only σ^+ transitions. The atoms are then subjected to a cycle of excitation and decay that brings them to the dark state $F = 2, m_F = +2$. The atoms that decay into the $F = 1$ manifold are repumped by resonant light to the $F' = 2$ also by driving σ^+ transitions.

We use the GM light with the D1 transition to perform this optical pumping, which we tune to resonance through the beat lock frequency. We define a quantization axis with the application of a 1.5 G field along the beam axis, which is tilted 14.5° from the experiment defined as the x-axis. The beams from all the other directions and the counter-propagating beam on the x-axis are blocked using mechanical shutters. In the same way as before, to avoid the trap light shift, we perform the state preparation chopped, for a total duration of 300 µs with intensities of 0.3 I_{sat}.
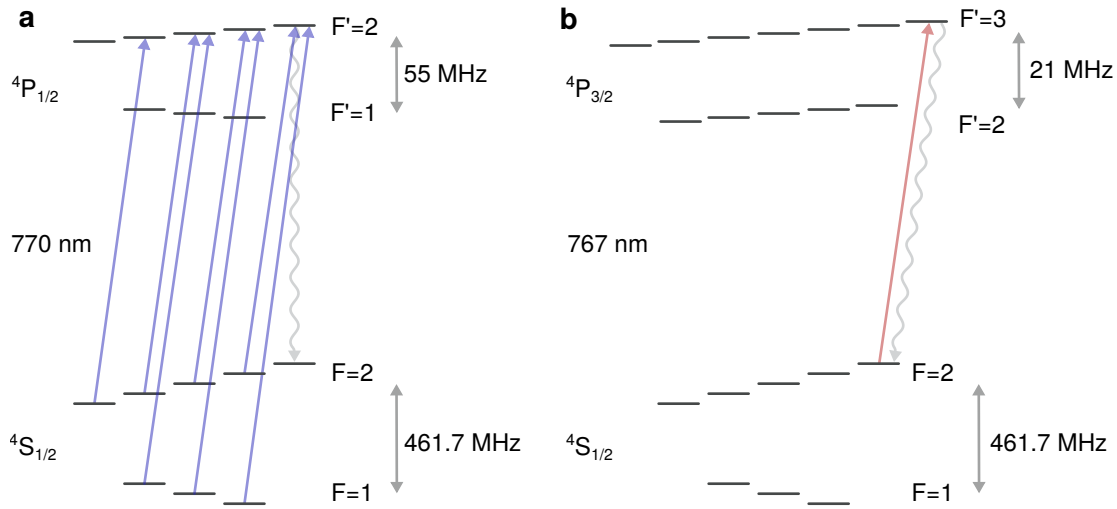
Figure 3.24: Scheme for the state preparation and selective state detection. a Level scheme for the preparation in the $F = 2, m_F = 2$ state. Circularly polarized light σ^+ optically pumps the atoms to the $F = 2, m_F = 2$ state. The atoms scatter and decay until they reach the $F = 2, m_F = 2$ state, which is dark to the pumping light. The number of scattering events is low enough not to produce a loss from the trap. Repumping light is also needed in case the atoms decay into the $F = 1$ manifold. A magnetic field of $1.5\,\mathrm{G}$ defines the quantization axis. **b** Level scheme for the measurement of a single state with the removal of the atoms in the second populated state. Only the atoms in the $F = 2, m_F = +2$ state are removed by selectively heating them out of the traps. The atoms scatter on the closed transition between the $F = 2, m_F = +2$ state and the $F' = 3, m_F = +3$ state, and effectively heats the trapped atoms to make them escape from the traps. Figure adapted from [62].

To estimate the preparation efficiency, the optical pumping time τ_{OP} and the depumping time τ_{DP} are measured, as shown in Fig. 3.25. After the state preparation pulse, the light driving the $F = 2$ to $F' = 2$ is switched on again for varying amounts of time. Before taking the last image, we remove the atoms in the $F = 2, m_F = 2$ state. With the second image, we measure the remaining atoms, which are transferred to the $F = 1$ manifold. The measurement takes into account imperfections in the pumping light that can drive σ^- or π transition, depopulating the stretched state by uncontrolled spontaneous decay into the $F = 1$ manifold. To remove only the atoms in the $F = 2, m_F = 2$ state, we drive the closed transition to $F' = 3, m_F = +3$ state of the D2 line with a resonant pulse. This pulse only heats the atoms in the $F = 2, m_F = +2$ state, making them escape from the trap.
With a second fluorescence picture, we can determine the depumping time τ_{DP} by measuring the atoms in the $F = 1$ manifold.
The operation is performed a second time with a $45°$ rotation of the quantization field, mixing all polarizations and allowing to extract the optical pumping time τ_{OP}. Comparing the two measurements, we can evaluate how well we suppress unwanted scattering events. We are able to estimate a state preparation efficiency

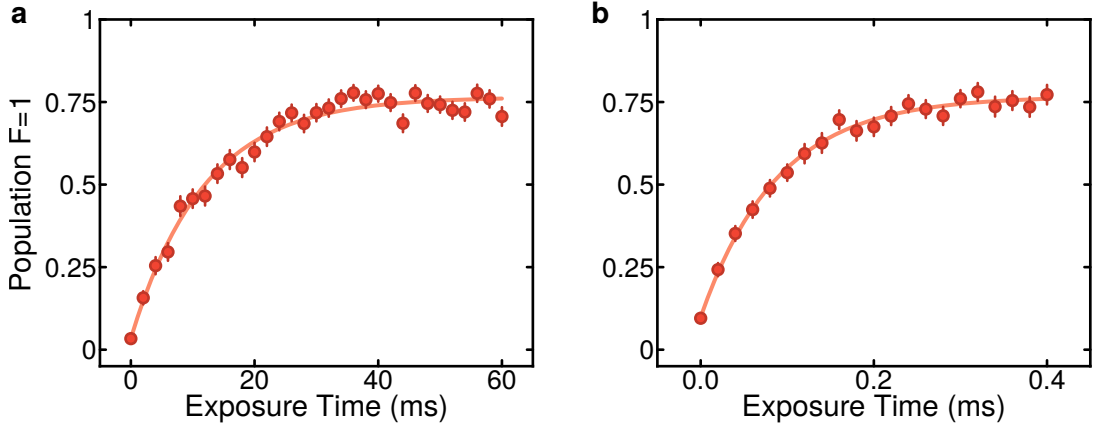of $P(F = 2, m_F = +2) = 1 - \tau_{OP}/\tau_{DP} = 99.25 \pm 0.06\%$ [151].

Figure 3.25: Characterization of the state preparation fidelity. Measurements of the depumping time after preparing the atoms in the $F = 2, m_F = 2$ state and exposing the atoms to resonant light on the $F = 2$ to $F' = 2$ transition. A push out pulse is applied to measure only the atoms depumped into the $F = 1$ manifold. **a** The magnetic field is aligned parallel to the pumping beam. The exponential fit from the data show a time constant of $\tau_{DP} = 11.8 \pm 0.7$ ms. **b** The magnetic field is tilted with respect to the depumping beam to create a mix of polarization for the depumping light. The exponential fit shows a time constant of $\tau_{OP} = 88 \pm 4$ µs.

3.5.2 Raman sideband cooling

The atoms loaded into the tweezers with the use of either red or gray molasses cooling are sufficient to perform experiments with Rydberg states as the references show [41, 152]. However, the atoms are still in a thermal state, which can be limiting if we want to perform more refined Rydberg dressing experiments. The limiting factors, in this case, can be several: the Doppler shift due to the thermal velocity distribution, broadening due to the different positions explored, and the trap depths' inhomogeneity. These limitations pointed us to perform another cooling stage to bring the atoms to their vibrational ground state in the traps.

We use Raman sideband cooling (RSC) [153–155], to efficiently cool atoms to their vibrational ground state in tight optical traps. Recently several experiments have already implemented this cooling technique in optical tweezers both with alkali [102, 103, 156] and alkaline-earth atoms [32]. In the following, we show the implementation of Raman sideband cooling in the event of an array of 64 traps with Potassium39 atoms, as in our publication [77].

The Raman laser is blue detuned $\Delta_R = 2\pi \cdot 40$ GHz from the $4S_{1/2}$ to $4P_{1/2}$ transition. All the beams have linear polarization aligned in-plane or parallel to the quantization axis to prevent vector light shifts. They have a beam size of $\omega_0 = 250$ µm which produce a coupling of $\Omega_R = 2\pi \cdot 43$ kHz driv-

ing the $F = 2, m_F = +2$ to $F = 1, m_F = +1$ ground state transition. We use the state preparation beams to perform the repumping, but are blue detuned $\Delta_{OP} = 2\pi \cdot 80 \pm 30$ MHz from the in-trap $4S_{1/2}$ to $4P_{1/2}$ resonance to prevent heating. The error denotes the standard deviation from the average of the measurement of 64 individual tweezers. It comes from the inhomogeneity of the array. The repumper beams have an intensity of 4 mW/cm^2 each.

We perform Raman sideband cooling after loading and imaging the atoms. At this point, we switch off the chopping of the traps that we need for the loading. We raise the trap depth to $U \simeq k_B \times 1.7$ mK to increase the trapping frequencies by a factor of 1.5. Then cooling cycles are performed both in the radial and axial directions. In each cycle, we chirp the laser over 120 kHz to take into account the inhomogeneities of the traps. Then a subcycle is applied to cool the last four sidebands. The process takes 150 ms. During all the repumping cycles, the repumping beams are kept on.
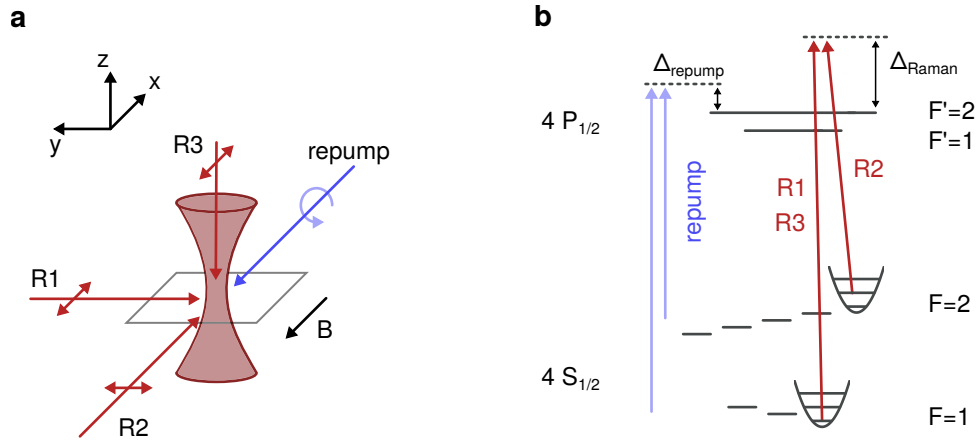
Figure 3.26: Beams dispositions and level diagram for Raman sideband cooling. a Schematic of the Raman beams with respect to the traps. We apply a quantization field of 1.5 G along the x-axis. The repumpers are circularly polarized to drive σ^+ transitions. All the Raman beams are linearly polarized to prevent the generation of vector light shifts. R1 and R2 lie on the x-y plane and only couple radial sidebands. R3 is aligned along the z-axis and, together with R2, addresses the axial sidebands. **b** Level scheme for the Raman sideband cooling. The Raman laser drives transitions between the $F = 2, m_F = +2, n$ and the $F = 1, m_F = +1, n - \Delta n$ states. The Raman laser is blue detuned by 40 GHz with respect to the D1 line. The repumper light is detuned $\approx 2\pi \cdot 80$ MHz from the D1 line to reduce the heating from the anti-trapped excited states. Figure from [62].

We perform sideband spectroscopy to quantify the cooling efficiency. After cooling, we apply a pulse to transfer atoms from the $F = 2, m_F = +2$ to the $F = 1, m_F = +1$ state, using the same conditions as for the cooling. Afterwards, we ramp down the traps to 20% of their power, and remove the $F = 2, m_F = +2$ population in the same way as in the state preparation, see Section 3.5.1, using

resonant D2 light. In the event of radial spectroscopy, we apply a $\approx \pi/2$ pulse on the carrier, while for the axial one, a $\approx \pi$ pulse is applied. In the two cases, the pulse length corresponds to less than $\approx \pi/2$ pulse on the respective sidebands. We can now estimate from the result of the sideband spectroscopy (Fig. 3.27) the mean vibrational quantum number. We extract from the spectroscopy the strength of the blue and red sideband $I_{blue/red}$ to calculate the mean vibrational quantum number $\bar{n}/(\bar{n}+1) = I_{blue}/I_{red}$.

The best cooling results for a single tweezer are $\langle \bar{n}_{rad} \rangle = 0.13$ and $\langle \bar{n}_{ax} \rangle = 0.23$ corresponding to a ground state probability of 69%. The cooling was optimized to have the best average performance over the whole array.
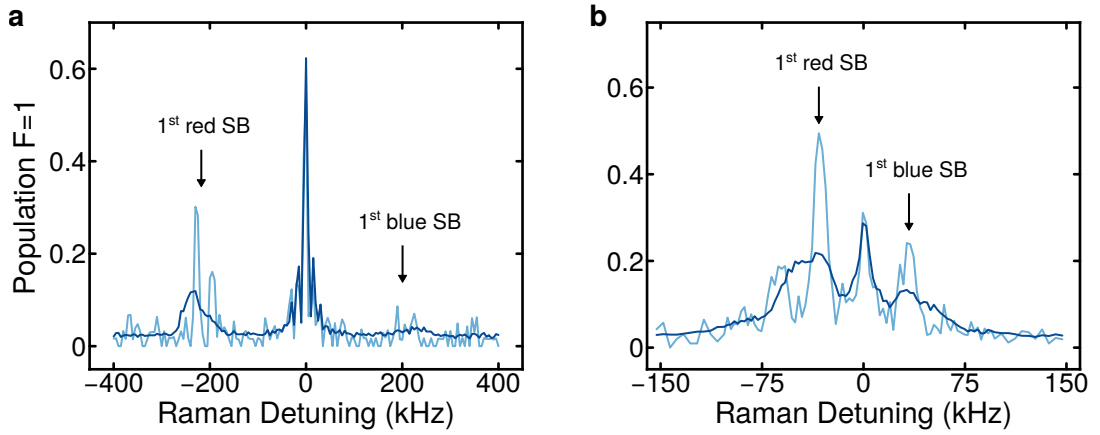

Figure 3.27: Sideband spectroscopy. a Radial sideband spectroscopy for a single tweezer in the array (blue) and the averaged signal over all the tweezers (dark-blue). We see the first vibrational sideband on the left. The presence of two peaks is due to a slight ellipticity of the tweezer, as already shown in Section 3.3.2. **b** Axial sideband spectroscopy for a single tweezer in the array (blue) and the averaged signal over all the tweezers (dark-blue). In the single tweezer case, we can resolve higher sidebands. Figure adapted from [77].

After applying Raman sideband cooling, we can check the lowest value of trap depth at which we can hold the atoms. This value is important in the case of Rydberg dressing, which is performed by keeping the atoms trapped. There are several advantages of lowering the trap depth. If the trap depth U is lowered adiabatically, the atomic thermal distribution follows as $T \propto \sqrt{U}$. The atoms are adiabatically cooled as explained in reference [157]. Secondly, we linearly decrease the difference in light shifts between the traps due to inhomogeneities. We lower the trap power in 50 ms. Subsequently, we hold the atoms in the traps for another 50 ms before ramping up the power. Then we take a second picture. We use a dual stabilization loop to increase the dynamic range of the power stabilization as described in Fig. 3.2.

To satisfy the adiabaticity condition, the change in trap frequency $d\omega/dt$ must be much larger than ω^2 [158]. The condition is also fulfilled for the lowest axial trap frequency at low powers, which is on the order of 1 kHz.

We show the results for the ramping down of the trap power in Fig. 3.28. Without the application of Raman sideband cooling, the loss of atoms starts as
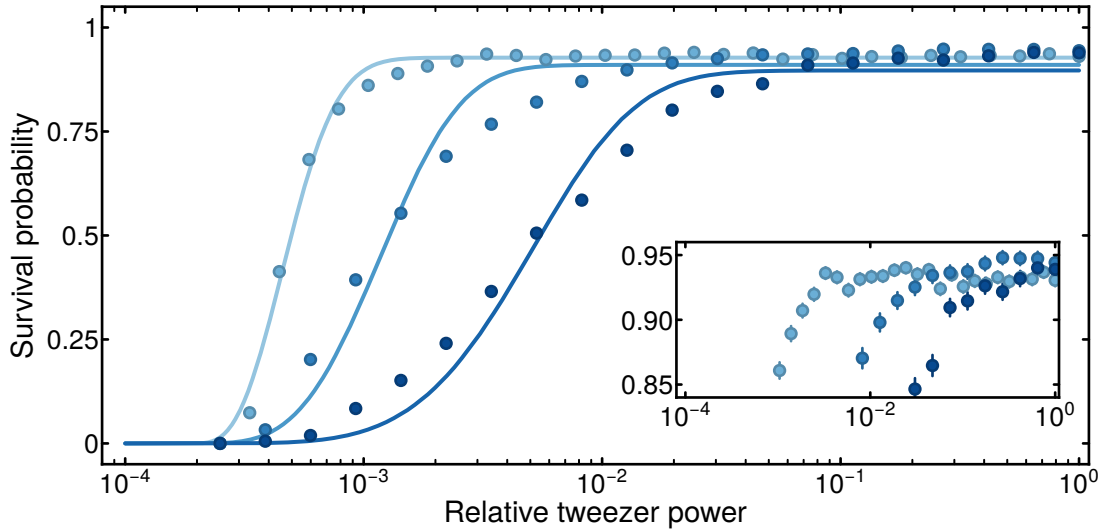
Figure 3.28: Survival probability as a function of the ramped down tweezer power. The tweezer power is expressed relative to the power we usually use to load the atoms into the tweezers. The data is generated by averaging all 64 tweezers. Going from light to dark blue, RSC overall directions, RSC only along the radial axis, and no RSC performed. The solid lines are fits using a Boltzmann distribution and taking into account the effect of gravity. We can not lower the traps' power below $2 \cdot 10^{-4}$ due to gravity, which opens the trap, and removes the confinement along the axial direction. The inset shows a magnified part. Figure adapted from [77].

soon as the trap power is lowered to 10% of its initial value, corresponding to a trap depth of $\approx k_B \times 100\,\mu\mathrm{K}$. With Raman sideband cooling, we can significantly reduce the power of the traps and still hold the atoms. With all axes cooling, we can lower the trap depth to $\approx 0.005 \cdot U_0$ of the initial value, with a final trap depth of $k_B \times 3.7\,\mu\mathrm{K}$. Gravity, which is along the weak axis of the traps, limits the reduction of power to a value of $2 \cdot 10^{-4}$ of the initial power since we can no longer keep the atoms confined in the axial direction. An additional dipole trap or a vertical lattice [32] can be used to overcome this limitation. Better confinement along the weak axis of the tweezers can help to improve the RSC efficiency, with better resolution of the sidebands. With extra vertical confinement, we can further reduce the tweezers' power, compensating for the effect of gravity in the vertical direction.

3.5.3 Driving of ground state transitions

The last tool that we need to introduce in our system is the one that enables coherent ground state manipulation of the trapped atoms. The standard method in the cold atom community is to use microwave radiation coupled to the atoms via a horn or an antenna to drive the ground state transitions directly. An alternative would be to use two Raman beams to drive the ground-state transitions. Co-propagating beams are typically used to avoid the breaking of the Raman condition due to the Doppler shifts induced by the atomic motion. We implemented the configuration with two co-propagating beams. In this way, we avoided us-

ing microwave sources that can influence the electronics of our high power laser. The observation of this problem was reported in the Ph.D. Thesis of Cesar Cabrera [159].

We offset lock a laser to the Raman cooling laser to drive this transition, which in turn is locked to a ULE reference cavity. We use two AOMs in double pass configuration to bridge the ground-state hyperfine splitting. We use the same RF generator to drive them. This configuration makes the whole setup inherently phase stable. The beams are sent to the atoms from the y-axis with orthogonal linear polarization to prevent the effect of vector light shifts. The quantization axis is set along the x-axis to allow the driving of σ^+ and σ^- transitions with $m_F = \pm 1$. We use this configuration for the experiments shown in this thesis. We shaped the beam to be elliptical in order to improve the homogeneity over the whole array of traps with a horizontal $1/e^2$ diameter of 1 mm.

We characterize the coherent ground state control for a Raman detuning of $\Delta_R = 16.5$ GHz, with a 9×5 array with 15 μm spacing. Then we prepare the atoms in the $F = 2, m_F = +2$ state and subsequently drive the transition to the $F = 1, m_F = +1$ state. As we have done before for the state preparation and the Raman sideband cooling, we will detect the population in the $F = 1, m_F = +1$ state since we can easily remove the population in the $F = 2, m_F = +2$ state. Firstly, we characterize the Rabi frequency that we can obtain by applying a rectangular pulse measuring a frequency of $2\pi \cdot 96$ kHz (Fig. 3.29). We estimate the homogeneity of the beam along the x-axis by measuring the variation in Rabi frequency of single rows in an array see Fig. 3.29. We see that the maximum variation in coupling over a distance of 120 μm is 2.8% . To characterize the dephasing and decay time, a Ramsey measurement was employed. For the dephasing, we set a 30 kHz detuning to the Raman resonance for the two beams and apply two $\pi/2$ pulses varying the free evolution time between the pulses. We observe oscillations at this detuning with a Gaussian decay of 98 ± 4 μs, as shown in Fig. 3.29. With the measurement obtained, we can evaluate the effect of shot-to-shot changes in the magnetic field. The extent of the change can be estimated considering a central frequency of $2\pi \cdot 30$ kHz with a standard deviation of $2\pi \cdot 2.5$ kHz that brings the dephasing time to be ≈ 100 μs. The value corresponds to a root mean square magnetic field noise of 1 mG considering the magnetic field sensitivity of the states being driving. By applying a spin-echo π pulse in between the two $\pi/2$ pulses, we can increase the coherence time, canceling the shot-to-shot noise. All the pulses satisfy the Raman resonance, and the phase of the last $\pi/2$ pulse is changed by 180° with respect to the other pulses. As shown in Fig. 3.29, the echo pulse increases the decay time to 1 ms, improving it by one order of magnitude compared to the Ramsey measurement. We can repeat several echo sequences to increase the coherent time accordingly. Future improvements would be to synchronize the Ramsey sequence with the 50 Hz mains oscillation, to remove shot-to-shot variations.
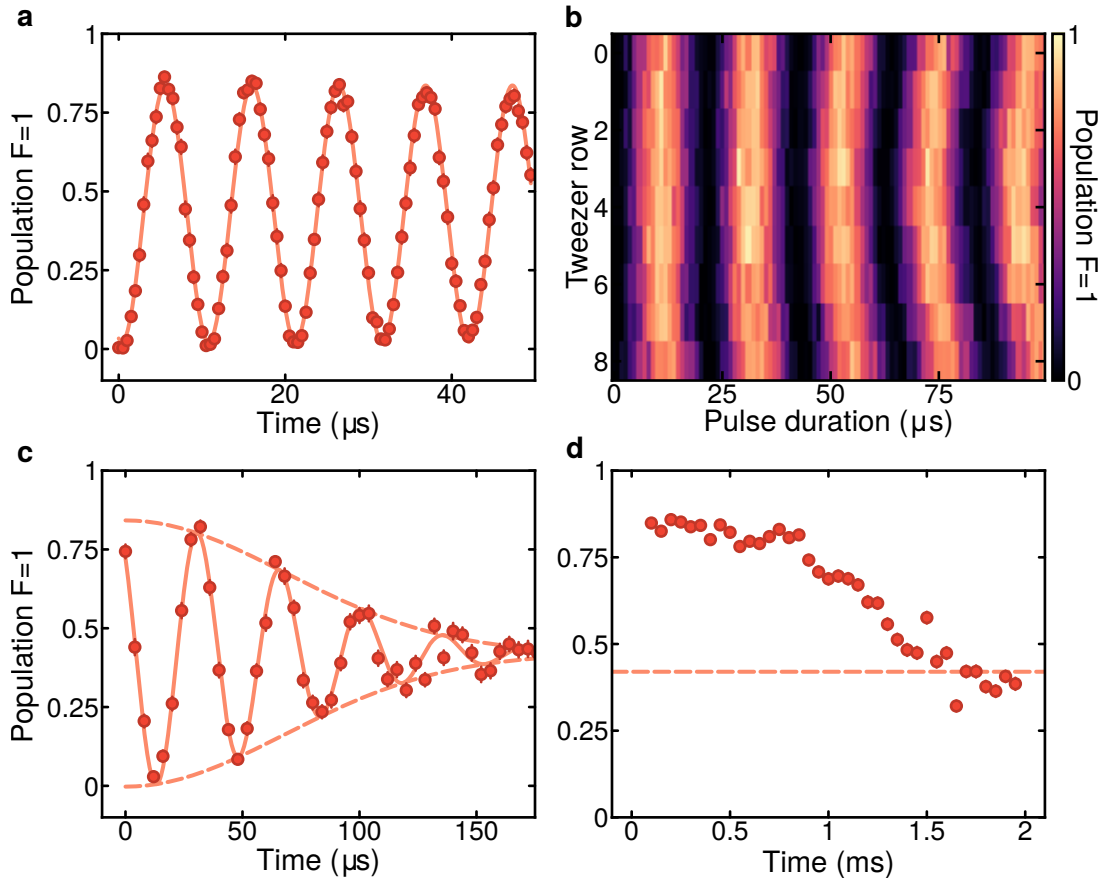
Figure 3.29: Rabi frequency, dephasing and decay time Ramsey sequence characterization. **a** Ground state Rabi oscillation in a 9×5 array between $F = 2, m_F = +2$ and $F = 1, m_F = +1$, the fit gives a Rabi frequency of $2\pi \cdot 96$ kHz. **b** Rabi oscillation with each row of tweezers averaged. The intensity profile of the Raman beam, aligned on the center of the array, is made visible by the slightly different Rabi frequency. **c** Ramsey oscillations for a detuning of 30 kHz from resonance. The fitted data shows an oscillation at a frequency of 30 kHz as expected, with a Gaussian decay of 98 ± 4 µs, due to the magnetic field noise. **d** Spin echo signal with one echo pulse. The phase of the last $\pi/2$ pulse is changed by $180°$, resulting in a full population inversion in the event of no decoherence. The signal shows a decay on a time scale of ≈ 1 ms. Figure adapted from [77]

Part III

Black-body Radiation Induced Facilitated Excitations

Chapter 4

Black-body Radiation Induced Facilitated Excitations

In this chapter, we are going to introduce interactions between atoms coupled to a Rydberg state. First, in Section 4.1 we give an idea of the spatial dependence of the interactions in regard to the Rydberg states involved. Then we will give some examples of how we can use these interactions to produce interesting physical effects. Next, in Section 4.2 we are going to show a tentative realization of the Rydberg dressing technique with our system. Lastly, we are going to report the results of our experiments regarding the lifetime reduction due to black-body radiation induced facilitation in arrays of atoms [160].

4.1 Rydberg Interactions

Thanks to their strong polarizability [36], Rydberg atoms interact between each other with long-range interactions. If we consider the case of two atoms separated by a distance d much larger than the size of the electronic wavefunction, the interaction potentials are given by the multipole expansion, dominated in this case by the dipole-dipole interaction [37]

$$U_{ddi}(d) = \frac{1}{4\pi\epsilon_0} \frac{\mathbf{d}_1 \cdot \mathbf{d}_2 - 3(\mathbf{d}_1 \cdot \mathbf{u})(\mathbf{d}_2 \cdot \mathbf{u})}{d^3} \tag{4.1}$$

where $\mathbf{u} = \mathbf{R}/d$ is the unitary vector pointing between the two atoms considering $\mathbf{R} = \mathbf{R}_2 - \mathbf{R}_1$ the separation of the atoms with positions $\mathbf{R}_1$ and $\mathbf{R}_2$ and distance calculated $d = |\mathbf{R}|$. The symbol $\mathbf{d}_i$ correspond to the electric dipole operator for an atom i.
If we consider two eigenstates for a single atom $|r'\rangle$ and $|r''\rangle$ with eigenenergies $E_{r'}$ and $E_{r''}$, in the event of no interactions present, the eigenstate for a two-atom system is the pair-state $|r'r''\rangle = |r'\rangle \otimes |r''\rangle$ with eigenenergy $E_{r'r''} = E_{r'} + E_{r''}$.

Consider two atoms prepared in the same state $|r\rangle$. Suppose the pair-state $|rr\rangle$ that they form is not degenerate with any other pair-state. In that case, we can apply perturbation theory to calculate the interaction potential as a function of the distance. In the first order of perturbation, the energy shift is equal to zero due to the parity of the $\mathbf{d}_i$ dipole operator, which is odd. The average value of the dipole-dipole potential U_{ddi} then vanishes since the atomic state $|r\rangle$ has a defined parity. The second order provides the energy shift by summing up all

the dipole coupled states

$$\Delta E_{rr} = \sum_{r'r''} \frac{|\langle rr| U_{ddi} |r'r''\rangle|^2}{E_{rr} - E_{r'r''}}. \tag{4.2}$$

Since the energy shift comes from the second order in U_{ddi}, the shift scales as $1/d^6$ corresponding to the van-der-Waals interaction, and we can express it as

$$\Delta E_{rr} = \frac{C_6}{d^6}. \tag{4.3}$$

The scaling dependence on the principal quantum number n is given by the numerator of Eq. (4.2), which scales as a dipole moment to the fourth power $\propto n^8$, while the denominator scales as $\propto 1/n^3$ being the difference in energy of close by pair-states. These contributions lead to a scaling of the C_6 coefficient as $\propto n^{11}$.

In the case that two atoms are prepared in different states $|r'\rangle$ and $|r''\rangle$ which have different parity, for example one nS and one $n'P$ states, with $n \simeq n'$. Then there are two possible degenerate pair-states $|r'r''\rangle$ and $|r'', r'\rangle$. In this case the dipole-dipole interaction can be expressed in the two possible pair-states basis and reduced to

$$U_{ddi} = \frac{C_3}{d^3} (|r'r''\rangle \langle r''r'| + |r''r'\rangle \langle r'r''|) \tag{4.4}$$

where the C_3 coefficient comes from the product of two matrix elements of the dipole operator between $|r'r''\rangle$ and $|r''r'\rangle$, scaling with $\propto n^4$.

4.1.1 Rydberg Blockade

The interactions illustrated before can produce strong energy shifts. Such an effect can be used in different ways. One way is the so-called Rydberg blockade [38–40, 50, 161], where the presence of an atom in a Rydberg state suppress excitations close to it.

The physics behind the blockade effect is quite interesting and can be used in the case of quantum information processing for the creation of fast two-qubit gates [37, 47, 48, 50, 51]. Also, the Rydberg blockade can be used in the creation of collective excitation of entangled states [162, 163] and also spatial correlations of excitations [164].

In a system composed of two atoms separated by a distance d, we can describe it in the following pair-states basis, $|g,g\rangle$, $|r,g\rangle$, $|g,r\rangle$ and $|r,r\rangle$, with $|g\rangle$ the ground state and $|r\rangle$ the Rydberg state. Considering a van-der-Waals interaction, the pair-state $|r,r\rangle$ will undergo a shift in energy given by U_{ddi}, with a negligible shift for the other states. Below a certain distance, the interaction will shift the driving laser out of resonance, otherwise on resonance for large distances. The

Rydberg blockade is defined as the excitation of one atom to a Rydberg state, precluding the excitation of nearby atoms. A schematic of the effect is given in Fig. 4.1.

The result of driving the Rydberg transition is a superposition of states [165]

$$|\psi_+\rangle = \frac{1}{\sqrt{2}}(|r,g\rangle + |g,r\rangle). \tag{4.5}$$

The system undergoes a Rabi oscillation with an enhanced frequency of $\sqrt{2}\Omega$, between the ground state $|g,g\rangle$ and the $|\psi_+\rangle$ state, with Ω is the resonant Rabi frequency ($\Delta = 0$) in the case of a single isolated atom.

The characteristic distance at which the resonant excitation can occur is the blockade radius defined as

$$r_b = \sqrt[6]{\frac{C_6}{\hbar\Omega}} \tag{4.6}$$

it defines the cut-off distance after which another atom can be excited to a Rydberg state.

Extending the treatment to the case of N atoms within the blockade radius, the system then oscillates between the ground state $|g,g,...,g\rangle$ and the collective excited state

$$|\psi_c\rangle = \frac{1}{\sqrt{N}} \sum_{i=1}^{N} |g,g,..,r_i,..,g\rangle \tag{4.7}$$

at the frequency $\Omega_c = \sqrt{N}\Omega$.

4.1.2 Anti-blockade and Facilitation

We speak of the anti-blockade effect [166] when the sign of the laser detuning Δ is the same as the energy shift given by the pair-interaction, this makes the opposite effect to the Rydberg blockade. Instead, we speak of facilitation when the excitation to Rydberg of an atom is triggered by the presence of a previously excited Rydberg atom. In both cases, the interaction makes the energy shift coincide with the detuning of the driving laser $\Delta = U_{ddi}(d)$, where $U_{ddi}(d)$ can be of the van-der-Waals or dipole-dipole kind.

Generally, the anti-blockade entails two atoms excited to the same Rydberg state, making its spatial dependence follow a van-der-Waals interaction. The level structure is illustrated in Fig. 4.2. Instead, with facilitation, we have two Rydberg states with opposite parity, following a dipole-dipole interaction. Theoretical proposals also made another scheme for the facilitation, where the system starts in a blockade regime and the movement of the initially excited atoms triggers further excitations, see reference [167]. The distances at which atoms are
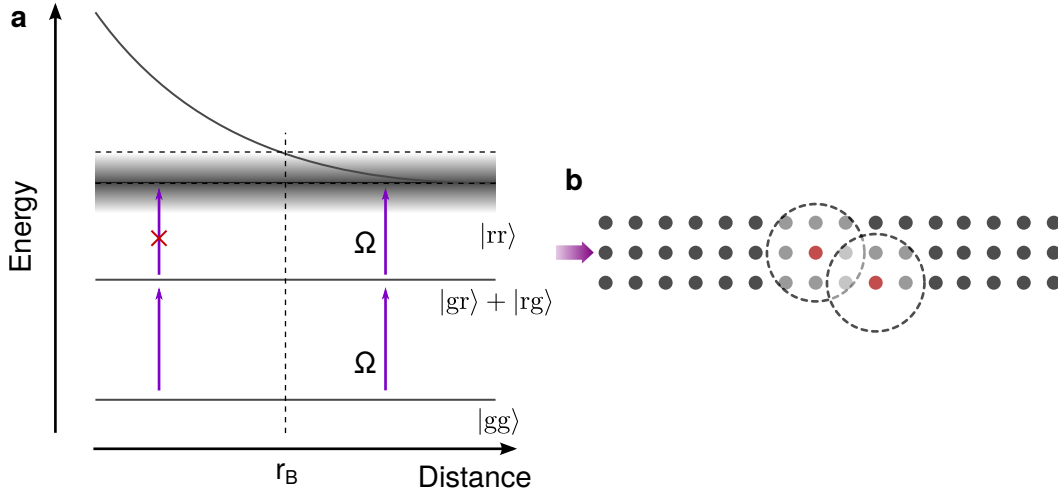
Figure 4.1: Rydberg blockade. In the case of resonant excitation, the long-range power-law of the interaction potential leads to the Rydberg blockade. **a** Pair states potentials, with large distances, two atoms can simultaneously be excited. While below the critical distance r_b, the doubly excited state is shifted off-resonant, blocking more than one atom's excitation at a time. The blockade radius r_b is determined by the interaction and the coupling Ω. **b** Sketch of the Rydberg blockade effect in a 3×16 array of atoms. The dashed line denotes the volume in which only a single excitation can be present.

resonantly excited in the two cases are given by the following formulas

$$r_{ab} = \left(\frac{C_6}{\hbar |\Delta|} \right)^{1/6} \quad \text{and} \quad r_f = \left(\frac{C_3}{\hbar |\Delta|} \right)^{1/3} \tag{4.8}$$

where r_{ab} is the anti-blockade radius and r_f is the facilitation radius as a function of the interaction coefficients C_6 and C_3 and the laser detuning Δ. Experiments and proposals based on Rydberg facilitation have been made which involved the dynamical creation of Rydberg aggregates [168–170], optical bistability [171–174] and the observation of kinetic constraints [175, 176].

4.1.3 Dressed Rydberg interactions

Another way to exploit the long-range nature of the interaction between Rydberg atoms is the Rydberg dressing technique. Rydberg dressing allows to engineer long-range interactions by admixing Rydberg state population to a ground state. Detailed derivations can be found in references [165, 177, 178]. Many proposals have been put forward about Rydberg dressing with the possibility of engineering new strongly correlated phases [63, 179–183]or applications for quantum annealing [53].

We assume a laser that couples the ground state $|g\rangle$ and a Rydberg state $|r\rangle$ of an atom with a coupling Ω and detuning Δ. When two Rydberg atoms are placed at a distance d, and they have the same state parity, they interact via the
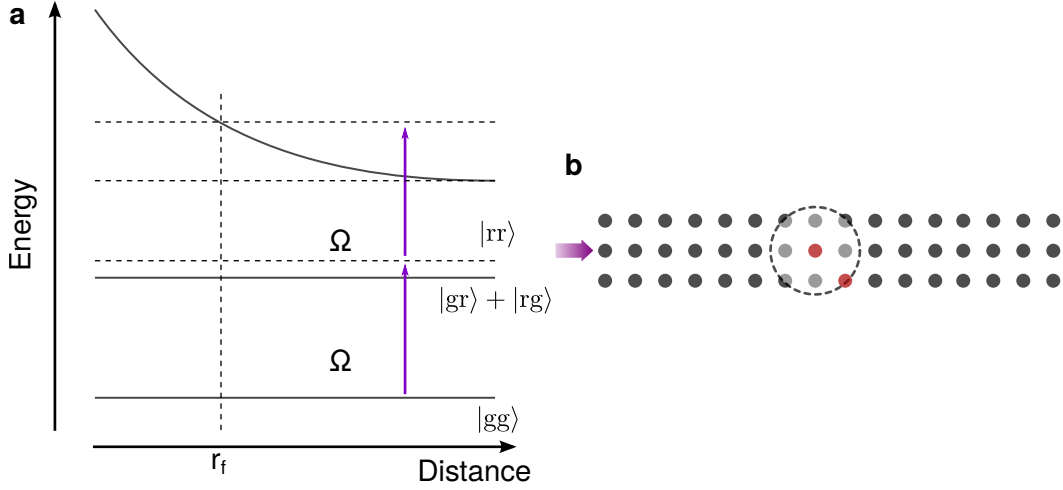
Figure 4.2: Rydberg anti-blockade and facilitation. In the event a detuning Δ from resonant is present, the excitation dynamic can undergo an anti-blockade or a facilitation effect, if the sign of the interaction is the same as the sign of the detuning. **a** Pair states level scheme, where an off-resonantly excited Rydberg seed, or impurity as we will call it later, triggers a resonant excitation for atoms at a distance r, close to the facilitation radius r_f. At the distance r_f the detuning Δ compensates for the shift from the interaction. **b** Sketch of the Rydberg anti-blockade and facilitation effect in a 3×16 array of atoms. The dashed line denotes the radius at which another atom is excited.

van-der-Waals potential $U_{vdW}(d) = C_6/r^6$ with C_6 a coefficient, which is characteristic of the van-der-Waals interaction as shown before.

We can calculate the interaction considering a coupling Ω and a detuning Δ from resonance. Where the sign of the detuning is opposite to the sign of the interaction. We can then consider the two atom basis made up of the ground state pair-state $|gg\rangle$, the excited state pair-state $|rr\rangle$ when both atoms are excited to the Rydberg state and the states $|+\rangle = 1/\sqrt{2}(|gr\rangle + |rg\rangle)$, $|-\rangle = 1/\sqrt{2}(|gr\rangle - rg)$ when only one atom is excited to the coupled Rydberg state. The state $|-\rangle$ can be eliminated from the calculation since it is a dark state. Now we can be in two regimes, either strong dressing regime when $\Delta \leq \Omega$ [61, 184] or in the weak dressing regime where $\Delta > \Omega$. In our case, we are interested in the latter, so we will not describe the strong regime case. Now we can find the eigenstates for the Hamiltonian described by the pair-states that we have defined

$$H(t) = \frac{\hbar}{2} \begin{array}{c} |gg\rangle \\ |+\rangle \\ |rr\rangle \end{array} \begin{pmatrix} \overset{\langle gg|}{0} & \overset{\langle +|}{\sqrt{2}\Omega} & \overset{\langle rr|}{0} \\ \sqrt{2}\Omega & -2\Delta & \sqrt{2}\Omega \\ 0 & \sqrt{2}\Omega & -4\Delta + 2U_{vdW}(d)/\hbar \end{pmatrix} \qquad (4.9)$$

We are interested in the energy shift that is exerted on the ground pair-state $|gg\rangle$. In the case of large distances $d \to \infty$ the ground state shift is produced only
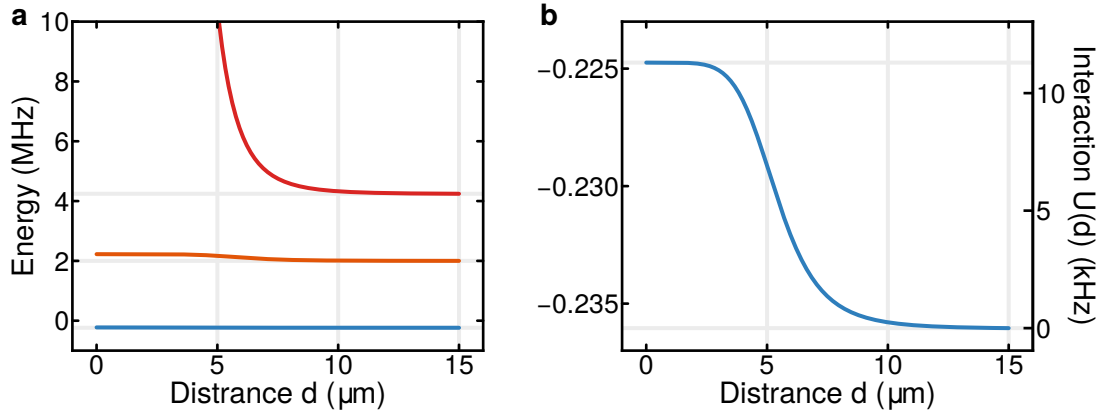
Figure 4.3: Rydberg dressing interaction. a Eigenenergies for the pair-state forming the base for the interaction Hamiltonian as a function of the inter atomic distance. The blue line shows the eigenenergies for $|gg\rangle$, orange for $|+\rangle$ and red for $|rr\rangle$. Establishing a realistic value for the coupling $\Omega = 2\pi \cdot 1\,\text{MHz}$ and detuning $\Delta = -2\pi \cdot 2\,\text{MHz}$, we will consider an interaction strength of $C_6 = 100\,\text{GHz}\,\mu\text{m}^6$. **b** Zoom on the resulting shift for the ground pair-state $|gg\rangle$ showing the characteristic soft core potential with a soft core radius $r_c = 5.4\,\mu\text{m}$. The overall shift to negative eigenenergies is given by the AC stark shift δ_{AC}.

by the driving laser AC stark shift δ_{AC} with

$$\delta_{AC} = -2 \times \frac{\hbar}{2}\left(\Delta \times \sqrt{\Omega^2 + \Delta^2}\right) \approx 2 \times \hbar\frac{\Omega}{4\Delta} \tag{4.10}$$

With shorter distances, the pair-state $|gg\rangle$ is shifted by an additional interaction V given by the admixture to the Rydberg state. The interaction V is given by

$$V(d) = \frac{V_0}{1 + (d/r_0)^6}, \tag{4.11}$$

$$r_0 = \left|\frac{C_6}{2\hbar\Delta}\right|^{1/6}, \tag{4.12}$$

$$V_0 = \frac{\hbar\Omega^4}{8\Delta^3}, \tag{4.13}$$

where V_0 defines the interaction strength and r_0 the softcore radius. With Rydberg dressing, we can transfer the long-range character of the Rydberg state to the ground pair-state $|gg\rangle$. An important characteristic of this scheme is the lifetime of the dressed state. The dressed state lifetime is given by the amount of Rydberg character mixed to the ground state. We define the admixture β as

$$\beta = \frac{\Omega}{2\Delta} \tag{4.14}$$

We can calculate the probability of an atom being in the Rydberg state by the square of the admixture β^2. The admixture limits the effective lifetime of the dressed state to

$$\tau_{eff} = \frac{\tau_r}{\beta^2} \qquad (4.15)$$

where τ_r is the electronic lifetime of the addressed Rydberg state.
Given this lifetime, we can estimate how many coherent cycles we can expect by taking the ratio between the interaction scale and the dissipation rate due to the limited Rydberg state lifetime. The rate is then

$$R = \frac{\Omega^2 \tau_r}{2\Delta} = \beta(\Omega \tau_r) \qquad (4.16)$$

In principle this is limited only by the maximum achievable coupling Ω. If we take reasonable values for the coupling $\Omega = 2\pi \cdot 1\,\text{MHz}$, with a detuning $\Delta = 2\pi \cdot 3\,\text{MHz}$ and we consider a Rydberg state lifetime of $\tau_r = 160\,\mu\text{s}$, in the case of the $62P$ state, we have a theoretical coherence ratio of $R \approx 25$.

4.2 Experimental realization of Rydberg dressing

In recent years several experiments have managed to implement Rydberg dressing as proposed in reference [185]. Successful experiments managed to entangle two atoms trapped in tweezers [61], implement transverse-field Ising dynamics with an atom gas cloud [60] and also observe coherent evolution of a few tens of atoms in a quantum gas microscope [58, 59, 186]. We will now present a preliminary experimental realization of Rydberg dressing made with our apparatus. Realizations of the Rydberg blockade with our apparatus can be found in the thesis of Nikolaus Lorenz [62] together with more details regarding the Rydberg dressing experiment. We start by discussing the effect of the laser phase noise over the dressed state lifetime and then show the two-body correlations that are generated by the dressing dynamics as in [58].

4.2.1 Effect of laser phase noise

The UV light that we use to couple the ground states with the $62P$ Rydberg state, which we are going to use for the experiments in this chapter, is at a wavelength of $\lambda_{UV} = 285.88\,\text{nm}$. We produce it as explained in Section 2.4 from an infrared seed laser that we amplify and frequency doubling twice to get the UV light. The seed laser is an ECDL laser. Its spectral profile can be approximated by the combination of a Gaussian and Lorentzian line-shape, the Voigt profile [187, 188]. In Rydberg dressing with $\Delta \gg \Omega$, the relative part that can influence the dressed state lifetime is the laser phase noise.
Then we can calculate the dressed state lifetime by combining the natural line shape of the atomic transition with the line shape of the laser. The convolution

of the two line shapes gives the result. It presents Lorentzian wings with an effective width of $\Gamma_{eff} = \Gamma_r + \Gamma_L$ where $\Gamma_r = 1/\tau_r$ the natural linewidth of the transition and Γ_L is the Lorentzian width corresponding to the phase noise of the laser. The effect can significantly reduce the theoretical dressed state lifetime.

We can estimate the difference between the theoretical admixture and the experimentally obtained for the laser from the measured occupation lifetime. The reason why we can use the occupation lifetime to measure the dressed state lifetime of the atoms is due to the ponderomotive force exerted from the trap to an atom which is excited to Rydberg [28]. The ponderomotive force is used in Rydberg blockade experiments to detect the excitations since they result in losses thanks to the repulsive character of the force.

To be able to perform the experiment, we need to prepare the atom in a defined state as we explain in Section 3.5.2. After the preparation, we lower the trap power and illuminate the sample with a UV pulse that couples to the Rydberg state $\left|62P_{1/2}, m_J = -1/2\right\rangle$ for different pulse lengths. This procedure is repeated during several different detunings Δ. Then we can compare the experimental result with the theoretical one by calculating $\alpha(\Delta) = \tau_{id}/\tau_{exp}$ as a function of Δ as shown in Fig. 4.4, where τ_{id} corresponds to the theoretical lifetime defined in Eq. (4.15).

We observe a reduction of the dressed lifetime up to 20 times to the theoretical one for close detunings while the reduction decreases for large detunings where the lifetime converges to the theoretical one.

The data shows that not only a broadening due to the laser phase noise is present, but we can see from Fig. 4.4 a modulation with periodically spaced peaks. The transfer of power from the carrier to the phase noise part of the laser spectrum due to the frequency doubling stages, as described in references [189–192], does not completely explain what we see. We are going to perform further investigations to understand where this effect is coming from.

In a future upgrade, we will filter the seed laser, as in reference [54], to reduce the phase noise or change the seed laser for one with much better phase noise characteristics.

4.2.2 Experimental results

We implemented the Rydberg dressing scheme with the atoms trapped in our tweezers. This experiment was performed at an earlier stage before we further optimized the Raman Sideband Cooling, so we lowered the trap depth to only 5% of the initial value of $\approx 1\,\text{mK}$. As for the lifetime measurement, we prepared the atoms in the ground state $\left|4S, F = 2, m_F = +2\right\rangle$ that we coupled to the Rydberg state $\left|62P_{1/2}, m_J = -1/2\right\rangle$. The atoms are arranged on a single line with 25 sites aligned parallel to the UV beam with a spacing of 4 μm. The coupling produced by the UV light is $\Omega = 2\pi \cdot 320\,\text{kHz}$ and the detuning was set to $\Delta = 6\Omega = 2\pi \cdot 1.9\,\text{MHz}$.

We measured the single atom AC Stark shift δ_{AC} with a Ramsey sequence composed of two $\pi/2$ pulses at the beginning and the end and a π pulse in between for rephasing. This was done with the method explained in Section 3.5.3 between
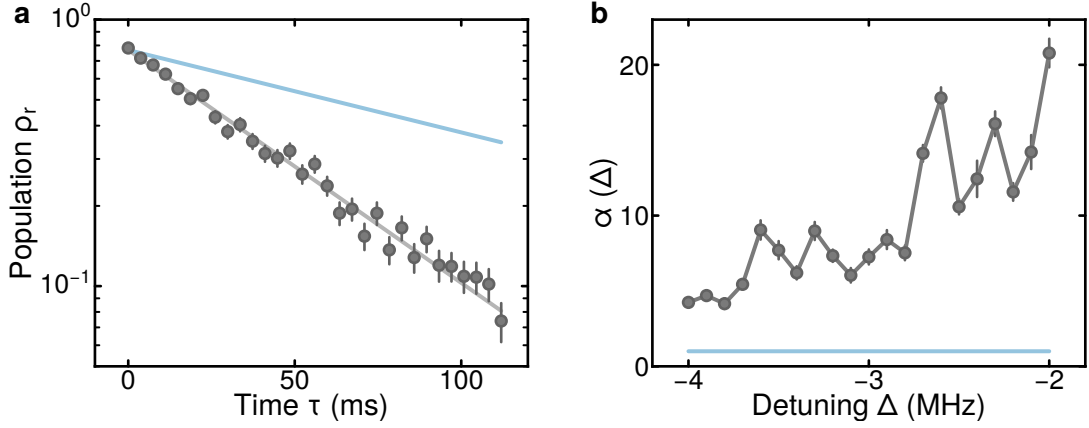
Figure 4.4: Single atom Rydberg dressed lifetime. a Lifetime of single dressed atoms in an array spaced 30 µm for $\Omega = 2\pi \cdot 270\,\text{kHz}$ and $\Delta = -2\pi \cdot 4\,\text{MHz}$. Where the grey line is the exponential fit to the data from which we extract a lifetime of $\tau = 49.3 \pm 1.1\,\text{ms}$, resulting in a factor $\alpha = 2.9$. The blue line marks the theoretical lifetime. **b** Reduction $\alpha(\Delta)$ of the single atom dressed lifetime as function detuning. The blue line on the bottom marks the ideal value where $\alpha(\Delta) = 1$ when the theoretical and experimental dressed lifetimes are the same.

the ground state $|4S, F = 2, m_F = 2\rangle$ and the ground state $|4S, F = 1, m_F = 1\rangle$. After the last $\pi/2$ pulse, we removed the atoms in the $|4S, F = 2, m_F = 2\rangle$ state with the technique exposed in Section 3.5.1. We applied the UV light in between the first $\pi/2$ and the π pulse. We show a scheme of the pulses in Fig. 4.5. The UV generates a shift on the $|4S, F = 2, m_F = 2\rangle$ state causing an oscillation of the measured Ramsey signal. The measured oscillation frequency is $2\pi \cdot 11\,\text{kHz}$, close to the theoretical prediction of $2\pi \cdot 13\,\text{kHz}$. The deviation to the theory is probably given by the inhomogeneities of the traps' light shifts because the expected interaction shift V_0 is an order of magnitude smaller than the deviation. To measure the interactions from the Rydberg dressing we perform the same Ramsey measurement as we did before but placing a second UV pulse between the π pulse and the last $\pi/2$ pulse, as shown in Figure Fig. 4.5, as in references [60, 162]. The estimated nearest neighbor interaction strength with our defined spacing correspond to $V(d = 4\,\mu\text{m}) = 2\pi \cdot 168\,\text{Hz}$, with a peak interaction strength of $V_0 = 2\pi \cdot 185\,\text{Hz}$ and soft core radius of $r_0 = 5.86\,\mu\text{m}$. With this interaction we expect a correlated phase shift of $\phi = V \cdot t = 36$ degrees.

In the experimental sequence, the atoms are placed in a superposition of the states $|4S, F = 2, m_F = 2\rangle$ and $|4S, F = 1, m_F = 1\rangle$ by the first $\pi/2$ pulse, which corresponds in the Bloch sphere picture in placing the atomic Block vectors on the equator. The π pulse applied 350 µs later is used to rotate the Bloch vectors by 180 degrees to rephase them and cancel any single atom light shift by holding them for another 350 µs. Then the phase of the last $\pi/2$ pulse is shifted by 180 degrees compared to the other pulses. This pulse maps the atom Block vectors to the $|4S, F = 1, m_F = 1\rangle$ state. We apply a pulse to remove atoms in the $|4S, F = 2, m_F = 2\rangle$ state and detect only atoms in the $|4S, F = 1, m_F = 1\rangle$ state. Interactions induce correlated phase shifts between two atoms, collectively rotat-
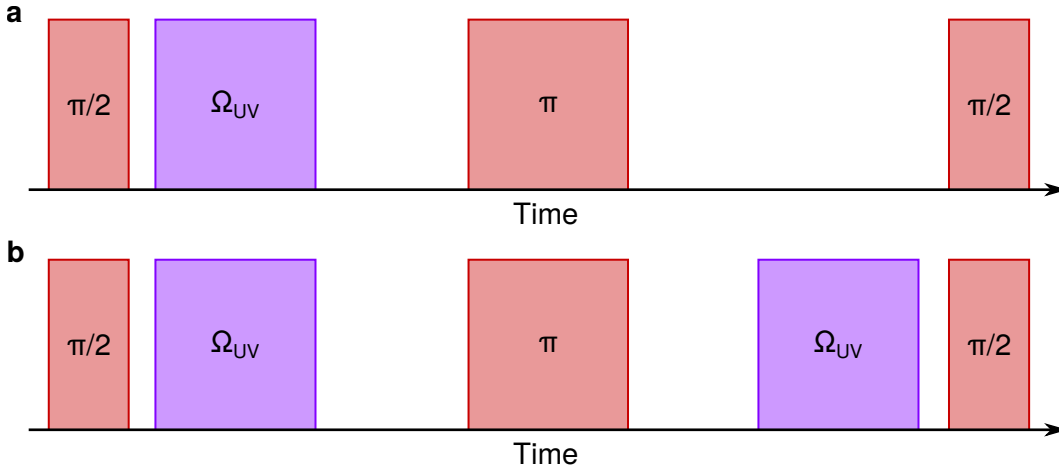
Figure 4.5: Experimental sequence for the Rydberg dressing. The pulses that drive the ground state transition are shown in red, while the purple ones represent the UV light for the dressing. **a** Ramsey sequence for the measurement of the AC Stark shift δ_{AC} from the dressing laser. **b** Ramsey sequence for the dressing experiment. The pulse length of the two UV pulses was changed, and the pulses were kept symmetric in position with respect to the beginning and end of the sequence.

ing the atomic Bloch vectors of the two atoms out of the plane of the Bloch sphere. Such a shift is not canceled by the rephasing induced by the π pulse. The correlated phase shift is detected with the application of the second $\pi/2$ pulse and the elimination of the $|4S, F = 2, m_F = 2\rangle$ state population. One way to visualize the correlated atom losses is to calculate two-body correlations $g^{(2)}(d)$, which produce the result shown in Fig. 4.6. We calculate the two-body correlations with the following formula, which is generalized for the 2D case too

$$g^{(2)}(d) = \langle (n_r - \langle n_r \rangle)(n_{r+d} - \langle n_{r+d} \rangle) \rangle \tag{4.17}$$

where $d = (d_x, d_y)$ is the distance vector connecting the positions between two tweezers, $n_r = \pm 1$ encodes the occupation of the trap at position r and the averaging is made over the experimental realizations and all distances.
With this experiment, we use a chain of traps, so the only distance relevant in this case is d_x.

4.2.3　Experimental imperfections

The result that we have shown before presents the formation of two-body correlations between the atoms, but there are several imperfections to take into account:

- **Array filling:** We have not implemented any reorganization of the atoms, which we have in plan for a future upgrade. The array filling is limited by the loading probability of the tweezers, which is $\sim 50\,\%$. We cannot expect
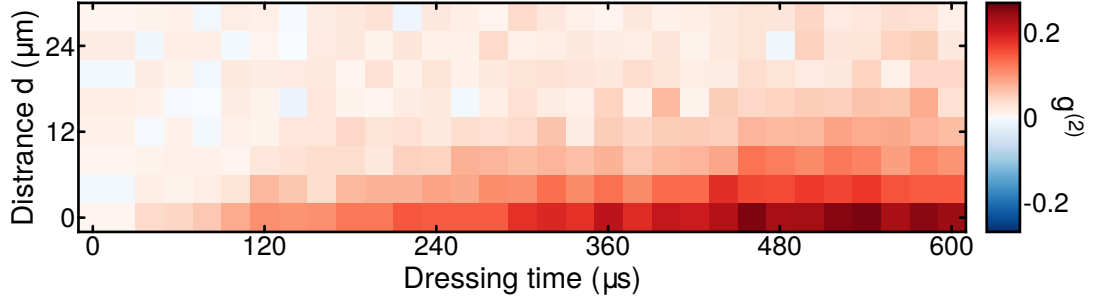
Figure 4.6: Signature of two-body correlations generated by Rydberg dressing.
Calculation of the two body correlation $g^{(2)}(d)$ as a function of the distance d at different dressing times. At $t = 0$ the system does not show the presence of correlations, while with the increase of the dressing time correlations start to build up. Figure adapted from [62].

to observe coherent interactions from the not completely filled chain, but only a first signal of correlation.

- **Rydberg dressed lifetime:** We have measured the lifetime for Rydberg dressed states, and we have seen a significant reduction to the expected theoretical value for the laser parameters used. The reduction of the lifetime by a factor 20, see Fig. 4.4, limits the coherence ratio R to a value below 1 from Eq. (4.16). We attribute this to the phase noise of the laser. We have planned future upgrades to the seed laser to address the problem.
  In Section 4.3 we will show that there is also another factor to take into account. A facilitation process that further reduces the lifetime.

- **Array inhomogeneities:** We performed the measurement at $5\% \cdot U_0$ of the initial trap depth of $U_0 = 2\pi\hbar \cdot 16\,\text{MHz}$. We had not fully optimized the parameters for the Raman sideband cooling, so we can not reduce further the trap depth. We show in Section 3.3.1 that we have on average a $\sim 10\%$ light shift inhomogeneities between the tweezers. We can see the inhomogeneities as a variation of the dressing detuning Δ. If we calculate the interaction strength V_0 from Eq. (4.13) considering the detuning variations, we estimate a difference in the interaction strength of $\sim 50\%$ over the atomic chain. The differences in interaction strength can be reduced to $\sim 4\%$ by lowering the trap depth to $0.005 \cdot U_0$, which is now possible after the optimization of the cooling, see Section 3.5.2.

Given these limitations, we do not expect to see the theoretical time and spatial dependence of the two-body correlations $g^{(2)}(\boldsymbol{d})$. We only show the formation of such correlations thanks to the generated interaction. Moreover, previously mentioned facilitated losses cannot be distinguished in the correlation signal, adding themselves to it and changing its time and spatial behavior. We will analyze in the next section the facilitation effect, with two-body correlations, uncovering the mechanism responsible for it.

4.3 Correlated Losses

In the past, successful realizations of Rydberg dressing were only achieved with small systems [58, 59, 61, 186] or for relatively short evolution times [60]. However, experiments performed in large atomic systems were unsuccessful in observing signs of Rydberg dressed interactions. After analysis, the reason behind failure was attributed to an anomalous induced broadening [193–197] which is caused by a facilitation mechanism. A scaling analysis [193] and a dynamic experiment [198] lead to identify the cause of the broadening to black-body radiation induced impurities, which trigger the facilitate excitation mechanism. The black-body radiation transfer the off-resonantly excited Rydberg state to a Rydberg state close by in energy with opposite parity. Then dipolar interactions cause an energy shift such that the off-resonant laser becomes resonant. A schematic is shown in Fig. 4.7.
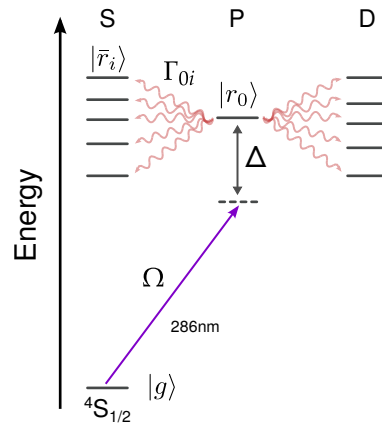
Figure 4.7: Level scheme off-resonant coupling and black-body radiation transfer. The atomic ground state $|g\rangle = |4S_{1/2}, m_F = +2\rangle$ and is coupled to the Rydberg state $|r_0\rangle = |62P_{1/2}, m_J = -1/2\rangle$ with Rabi coupling Ω and detuning Δ. Off-resonantly excited atoms to $|r_0\rangle$ are transferred by Black-body radiation to nearby Rydberg states with opposite parity $|\bar{r}_i\rangle$ at a rate Γ_{0i}.

The facilitated excitations quickly raise the population in the addressed Rydberg state, increasing the probability of another black-body-induced state change. The facilitation works as positive feedback leading to an avalanche excitation process.
Mean-field models employed to explain it show deviation from the experimental data, and further theoretical analysis pointed to the importance of correlations between the excited Rydberg atoms [199].

In our system, in the case of closely packed atoms, we are also able to observe a reduction of the dressed lifetime, compared to the previously reported one in Fig. 4.4. We show a lifetime measurement in Fig. 4.8, with also a picture of the array that we are using. The array is composed of 3×16 traps with a spacing of $5\,\mu m$. We can see from the measurement that the lifetime is reduced compared to the case of isolated atoms.

Our experiment, where we can resolve single trapped atoms, allows us to investigate the effect of black-body radiation induced facilitation by evaluating correlations between the lost atoms.

Figure 4.8: Reduced lifetime from facilitation. a Single fluorescence image of the 3×16 array with $5\,\mu m$ spacing. The gray arrow shows the magnetic field direction and the purple arrow the UV l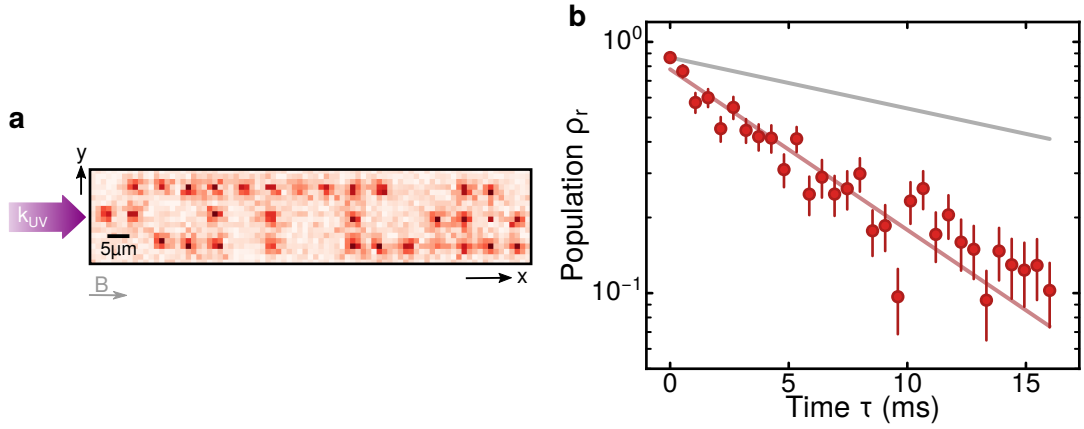ight direction. The magnetic field that we apply for the experiments will be of $10\,G$. **b** Measurement of the occupation lifetime under exposure of the UV light at $\Delta = -2\pi \cdot 4\,MHz$ and $\Omega = 2\pi \cdot 430\,kHz$. The dark-red line shows the exponential fit to the data, which reveal a lifetime of $6.8 \pm 0.4\,ms$, which is much shorter then the one limited by the laser phase noise of $21.4 \pm 1.3\,ms$ measured for individual atoms, shown by the gray line. Error bars denote 1 s.e.m.

4.3.1 Rydberg state lifetime

This section shows how the electronic lifetime of a Rydberg state is affected by black-body radiation to help us understand how impurities emerge in the system. We follow reference [200] for the calculation of effective lifetimes of Rydberg atoms from black-body induced depopulation.

The reduction of the Rydberg atom lifetime due to black-body radiation was shown for the first time in reference [201]. The depopulation rates were also experimentally measured in reference [202] where, with the help of a cryostat, they were able to show the temperature dependence of the black-body radiation induced transfers. Gallagher and Cooke [203] developed a theoretical model for the calculation of the effective lifetimes.

To calculate the effective lifetime of Rydberg states, one needs to take into account the spontaneous emission rates between the Rydberg states $|n,L\rangle$ and $|n',L'\rangle$ given by the Einstein coefficients

$$A(|n,L\rangle \to |n',L'\rangle) = \frac{4\omega_{nn'}^3}{3c^3}\frac{L_{max}}{2L+1}R^2(|n,L\rangle \to |n',L'\rangle), \qquad (4.18)$$

where L_{max} is the largest angular momentum value, $R(|n,L\rangle \to |n',L'\rangle)$ is the radial matrix element of the electric dipole transition and $\omega_{nn'} = |E_{|n,L\rangle} - E_{|n',L'\rangle}|$ is the transition frequency given by the difference in energy of the two states.

Subsequently the depopulation rate can be estimated considering the effective number of black-body photons per mode $\bar{n}_\omega$, given the Planck distribution at the environment temperature T,

$$\bar{n}_\omega = \frac{1}{\exp(\omega_{nn'}/k_B T) - 1}, \tag{4.19}$$

with k_B the Boltzmann constant. From the combination of the Einstein coefficients and the Planck distribution, the depopulation rate W can be calculated to every coupled Rydberg state

$$W(|n,L\rangle \to |n',L'\rangle) = A(|n,L\rangle \to |n',L'\rangle)\bar{n}_\omega. \tag{4.20}$$

One can now derive the total depopulation rate induced by black body radiation by taking into account all possible state transitions:

$$\Gamma_{BBR} = \sum_{n',L'} A(|n,L\rangle \to |n',L'\rangle)\frac{1}{\exp(\omega_{nn'}/k_B T) - 1}, \tag{4.21}$$

while the radiative lifetime τ_0 for a Rydberg state is determined only on the spontaneous transition rate to lower-lying states with $E_{|n,L\rangle} > E'_{|n',L'\rangle}$:

$$\frac{1}{\tau_0} = \Gamma_0 = \sum_{E > E'} A(|n,L\rangle \to |n',L'\rangle). \tag{4.22}$$

The effective lifetime of a the $|n,L\rangle$ Rydberg state is given then by the sum of the two rates Γ_0 and Γ_{BBR}:

$$\frac{1}{\tau_r} = \Gamma_0 + \Gamma_{BBR} = \frac{1}{\tau_0} + \frac{1}{\tau_{BBR}}. \tag{4.23}$$

The precision estimation of the effective lifetime is based on the calculation of the radial matrix elements $R(|n,L\rangle \to |n',L'\rangle)$.
We use the ARC Rydberg software [204] for the calculation of the black-body induced depopulation rates. The program also provides the branching information indicating which states the Rydberg atom is likely to be transferred or decay. In Fig. 4.9 we show the calculated rates for black-body radiation induced transitions at room temperature $T = 300\,\text{K}$ and at $T = 4\,\text{K}$. The calculation is done showing in both cases all the decay channels and their rates.
Moreover, we show the black-body radiation induced depopulation rate as a function of the principal quantum number for P states of Potassium39 in the case of both environment temperatures. The figure shows the contribution of the black-body radiation decay channel to the overall electronic lifetime. We can see that at $T = 4\,\text{K}$, which can be achieved with a cryostat, the contribution of the black-body radiation channel to the whole electronic lifetime is an order of magnitude lower than at room temperature.
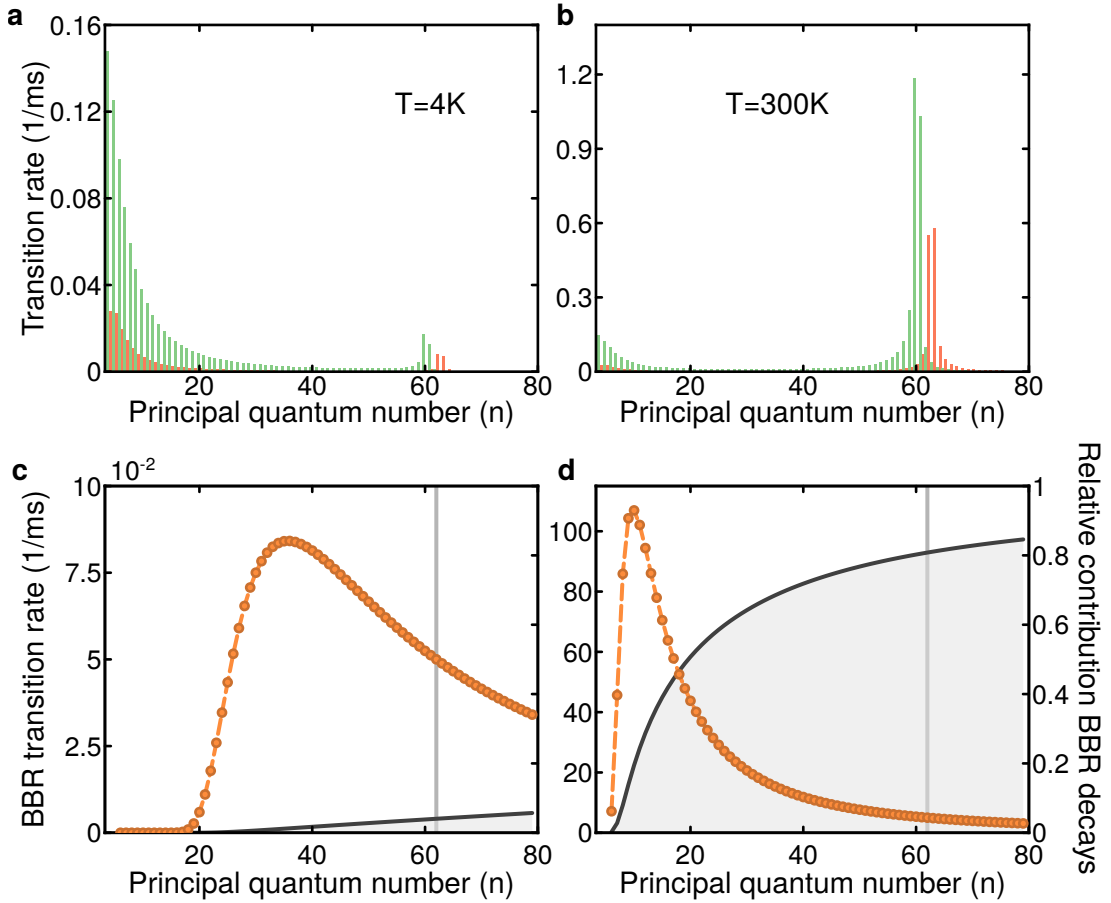
Figure 4.9: Black-body induced transition as a function of the environment temperature. a-b Black-body induced transition rates at 4 K and 300 K for the Potassium39 Rydberg state $|62P_{1/2}\rangle$, to $|nS_{1/2}\rangle$ (red) and $|nD_{3/2}\rangle$ (green) states. Black-body radiation induce transitions both to lower- and higher-lying states. **c-d** BBR induced transitions rates as a function of the principal quantum number n shown by the dots and the dashed line. The relative contribution to the Rydberg state lifetime at 4 K and 300 K of the BBR induced transitions, shown by the black line. The vertical line indicates the principal quantum number of the state that we use for the experiments reported in this thesis.

4.3.2 Facilitation channels

We will now show which interaction potentials we will consider in the analysis of facilitation in our data. We have explained in Section 4.1.2 about the facilitated excitation between Rydberg atoms. In our system, there may be one more facilitation channel coming from the possibility of ionizing a Rydberg atom from the trapping light. We will show that the ionization channel, in our conditions, is negligible.

Van-der-Waals potentials

To understand the facilitation mechanism that can induce excitations to Rydberg states, we have to consider the different pair-potentials formed by the $62P_{1/2}$,

with all the states coupled by black-body radiation. From the previous [Section 4.3.1](#) we have calculated all the depopulation rates induced by black-body radiation to close by Rydberg states. Now we have to calculate all the pair-potentials between the $62P_{1/2}$ state and the black-body radiation populated $|\bar{r}_i\rangle = |n', L'\rangle$ states.

For the calculation, we use the software Pairinteraction [205], which allows us to calculate the pair-potentials. The same calculation can also be performed with the ARC Rydberg software [204]. We show the result of the pair-potential calculation for the pair-state $\left|62P_{1/2}, m_J = -1/2, 62P_{1/2}, m_J = -1/2\right\rangle$ in [Fig. 4.10](#), with a magnetic field of $10\,G$ aligned parallel to the atomic pair. The interaction curve follows a $\propto C_6/d^6$ van-der-Waals interaction, where d is the distance between the two Rydberg atoms.
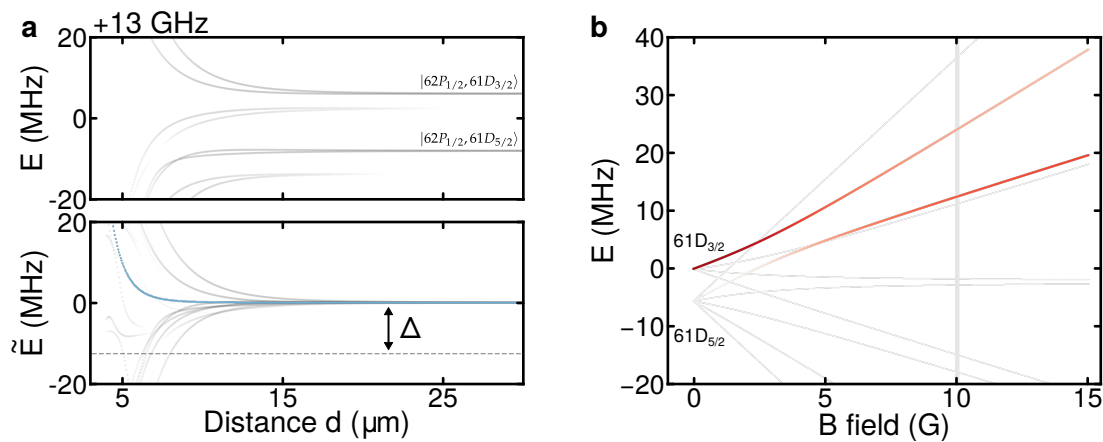
Figure 4.10: Construction of the dipolar facilitation potentials. a Top, the dipolar pair-potential plot of the pair-state $\left|62P_{1/2}, 61D_{3/2}\right\rangle$ is shown in a $10\,G$ magnetic field, in shades of grey. The shade of grey is proportional to the laser coupling rate. Bottom, the same pair-potential collapsed asymptotically onto the van-der-Waals pair-potential of the dressed pair-state $\left|62P_{1/2}, 62P_{1/2}\right\rangle$ (blue dots) is plotted. In a BBR induced transition to $|\bar{r}_i\rangle$, the energy difference between the two Rydberg states $|r_0\rangle = \left|62P_{1/2}, m_J = -1/2\right\rangle$ and $|\bar{r}_i\rangle$ is provided by the microwave photon. We can then collapse the pair-potential lines asymptotically from the couple BBR states $|\bar{r}_i\rangle$ onto $|r_0\rangle$, as shown in this single case. **b** Magnetic field map of the $61D_{3/2}$ state, We can see that the magnetic field mixes the $61D_{3/2}$ state with the $61D_{5/2}$ state due to the Paschen-Back effect. This explains the presence of several separate lines on the top left panel.

Now we can make the same calculation for the pair-state made up of $\left|62P_1/2, m_J = -1/2, 61D_3/2, m_J = -3/2\right\rangle$. We show the result in [Fig. 4.10](#). The interaction curves follow a $\propto C_3/d^3$ dipole-dipole interaction due to the opposite parity of the interacting Rydberg states.

In [Fig. 4.10](#) the potential curves are shown in the case of an atomic pair formed by two atoms in the $62P_{1/2}$ state and in the case with one atom being in the $61D_3/2$ state.

Besides the energy shift given by the interactions, in the plot, the color scale indicates the pair-state overlap

$$a_k = | \langle r_0 \bar{r}_i | \psi_k \rangle |^2 \tag{4.24}$$

with the initial unperturbed state $|r_0\bar{r}_i\rangle$ in the new eigenstate $|\psi_k\rangle$. The overlap a_k is automatically given in the output of the calculation made with the Pair-interaction software [205]. The new eigenstates come from the diagonalization of the interaction Hamiltonian taking into account all the possible pair-states which can be dipole coupled to the unperturbed state $|r_0\bar{r}_i\rangle$, with $\sum_k |\psi_k\rangle (d \to \infty) \to |r_0\bar{r}_i\rangle$. The overlap scales the resonant excitation rate $a_k \times \Omega^2/\Gamma$, which produces the rate for an atom in the ground state to be excited to the pair-state $|\psi_k\rangle$

Now we can consider the difference in energy between our starting pair-state and the one produced by the black-body radiation. We can subtract the unperturbed energy $E_{r_0\bar{r}_i,k}(d \to \infty)$ to each potential line. In this way, they will all fall to zero in the limit of large distances (asymptotically) where the zero energy point that we consider is the one given by the $E_{r_0r_0}(d \to \infty)$ of the pair-state $|62P_{1/2},62P_{1/2}\rangle$.

The two potential lines which present a not vanishing admixture with the unperturbed state at large distances are plotted in Fig. 4.10. The presence of two lines is due to the magnetic field that we apply to set the quantization axis in the experiment. The field mixes the two states because of the Paschen-Back effect. We show it affects the state admixing in the field map for the magnetic field in Fig. 4.10 for the $61D_3/2$ state.

Ion induced excitation

Rydberg atoms can be easily ionized using an electric field gradient or photons that provide enough energy to overcome the ionization threshold. We are interested in the ionization probability from the trapping light due to the DC shift exerted by the photo-ionized Rydberg atom on the surrounding atoms. Such a shift can produce a facilitation effect depending on the sign of the detuning also known as Coulomb facilitation, as shown in references [206, 207].
The energy shift created by an external electric field onto a Rydberg atom is calculated by the following Hamiltonian

$$H = H_0 + \epsilon \hat{z} \tag{4.25}$$

where H_0 is the unperturbed Hamiltonian, and ϵ is the electric field applied along the z-axis. In the case of low angular momentum states in a low field, the energy shift is dominated by the second-order perturbative term $\alpha_0\epsilon^2/2$, with α_0 the scalar polarizability

$$\alpha_0 \approx 2 \sum_{r_0 \neq r'} \frac{| \langle r_0 | \hat{z} | r' \rangle |^2}{E_{r'} - E_{r_0}}, \tag{4.26}$$

where the sum is applied over all the Rydberg state $|r'\rangle$ which are coupled to $|r_0\rangle$ state, for which we want to calculate the polarizability. The calculation is valid in the case of low fields and with low state admixing. In the other case, one needs to diagonalize the full Hamiltonian as in reference [208].

We can generate a Stark map for the level we are interested in for our experiment using Pairinteraction software [205], as we show in Fig. 4.11. The state $|62P, m_J = -1/2\rangle$ has a calculated scalar polarizability of $\alpha_0 = 435.51\,\text{MHz}\,\text{cm}^2/\text{V}^2$.

Now we can calculate the energy shift due to the electric field from a single charge for the state from

$$U_E = -\frac{1}{2}\alpha_0 \cdot \epsilon^2. \tag{4.27}$$

The result is shown in Fig. 4.11 compared to the pair-potential lines from Fig. 4.10. The stark shift can induce facilitation since it can move to resonance the Rydberg state for negative detunings Δ in our case.

To calculate the probability of having a photo-ionization event of our Rydberg atom, we follow this reference [209] which does a calculation and measurement in the case of Cesium Rydberg atoms in an optical dipole trap made with 1064 nm light. More calculations and measurements were made in references [50, 210]. In reference [209] the photo-ionization rate is estimated to be $\gamma_{PI} \approx 4\,\text{kHz}$ for Cesium atoms in a 1064 nm optical trap with 129 kWcm^{-2} peak intensity. Given that we use Potassium39 and not Cesium, we can use the estimated photo-ionization rate to calculate with which probability we photo-ionize from our traps. There will be a difference in rate between the two species which should be small. In our case we have a peak intensity of 716 kW cm^{-2} at a trap depth of 1 mK with a waist of 0.8 µm. We can scale the photo-ionization rate given for Cesium given our intensity. Then we have to consider the motion of the Rydberg atom. The atoms are expelled from the tweezer by the ponderomotive potential. In our case, the ponderomotive shift is almost equal to the trap potential but with the opposite sign. Moreover, we have to consider the thermal velocity of the trapped atom and the momentum transmitted by the absorption of a UV photon when excited to Rydberg. All the effects above reduce the amount of time passed by the Rydberg atoms in the trap, giving us an effective time to consider for the photo-ionization.

If we do not consider the spatial dependence of the trap's intensity, we can estimate the maximal probability for photo-ionizing event to occur. For the configuration that we use in the following experiments with 5 µK trap depth, we estimate a maximal photo-ionization probability of $\lesssim 10^{-3}$.

This estimate tells us that we do not expect any facilitation from the presence of ions in our sample.
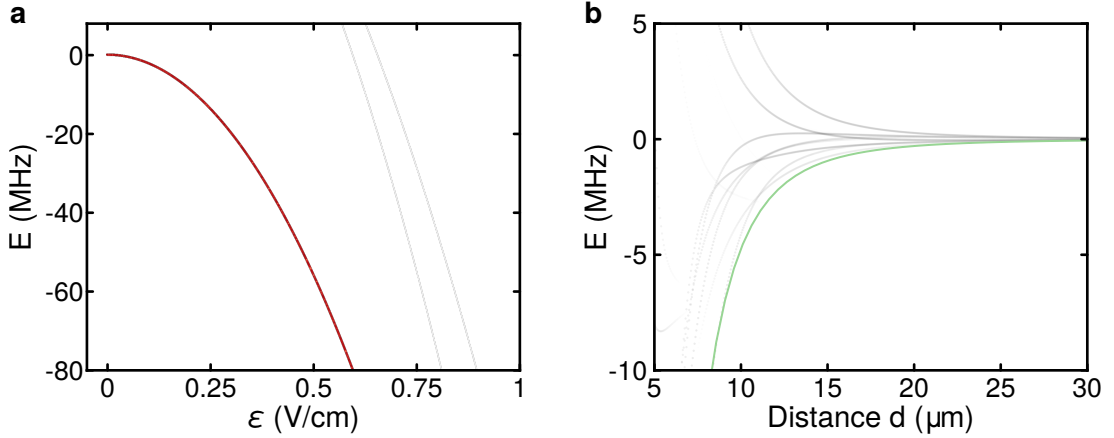
Figure 4.11: Stark map and Coulomb facilitation curve. **a** Stark map of the $\left|62P_{1/2},m_J = -1/2\right\rangle$ state from which we can calculate the electric polarizability of the state. **b** Pair potential plot of the $\left|62P_1/2,m_J = -1/2|61D_3/2,m_J = -3/2\right\rangle$ with the BBR energy subtracted as in Fig. 4.10, in grey shades. The green potential line shows the energy shift produced by an single charged ion to the $\left|62P_1/2,m_J = -1/2\right\rangle$ state as a function of distance. Both potential lines are close due to the similar scaling, $\propto 1/d^3$ for the dipole interaction and $\propto 1/d^4$ for the electric field shift.

4.3.3 Experimental observation of dipole-dipole facilitated losses

In Section 4.3.2 we have shown that the presence of contaminants, such as atoms in nearby Rydberg states with opposite parity, can lead to a strong dipole light shift for nearby atoms. In the limit of a small excitation fraction, we can consider facilitation as only a two-body process. We have shown that the process reduces the lifetime in our traps compared to the one for a single isolated atom. We can characterize more effectively the presence of this facilitation process by the evaluation of two-point correlations on the lost atoms with the function already used for the Rydberg dressing results defined in Eq. (4.17).

We give an example of the two-body correlation $g^{(2)}$ that we have evaluated for the case of $\Delta = -2\pi \cdot 4\,\text{MHz}$ in Fig. 4.12. If the losses were determined purely by off-resonant excitations from the coupling laser, no two-body correlation could be measured.

We evaluate the correlation at different illumination times of our atoms. As we can see, the amplitude of the two-body correlations grows in time while it is zero, as we expect, for zero illumination time.

To prove the connection between the two-body correlation with the dipole potential that we have calculated before in Section 4.3.2 we performed the following experiment. We illuminated our atoms with UV light at a fixed detuning. The Rabi coupling was adjusted to keep the theoretical admixture β to the coupled state constant. We fixed the value of β on the maximal coupling and detuning that we use $\Omega_{max} = 2\pi \cdot 400\,\text{kHz}$ and $\Delta_{max} = -2\pi \cdot 8\,\text{MHz}$. The coupling is then scaled accordingly depending on the detuning $\Omega = \Omega_{max}/\Delta_{max} \times \Delta$.

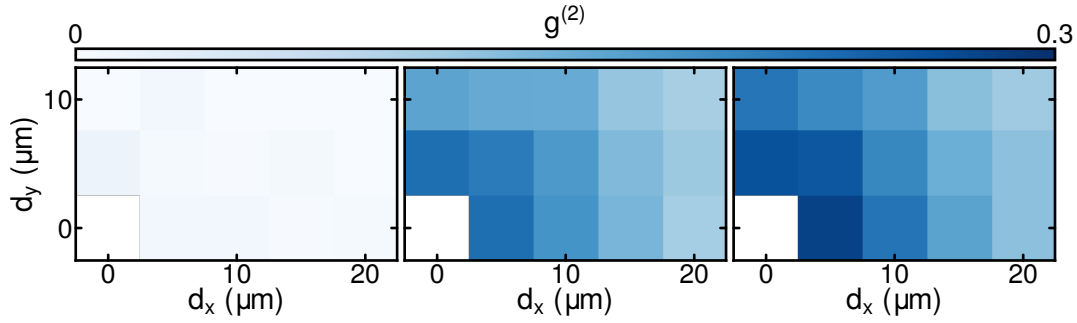The amplitude of the two-body correlation $g^{(2)}$ is strongly dependent on the il-

Figure 4.12: Two-body correlation $g^{(2)}$. The correlation is evaluated at different illumination times. The data was evaluated for the same configuration of the lifetime data shown in Fig. 4.8. The correlation was evaluated at $t = 0\,\text{ms}$, with no UV light, at $t = 1\,\text{ms}$ and $t = 3.6\,\text{ms}$ of illumination, from left to right. The correlation is plotted as a function of the distances d_x and d_y along the x- and y-axis directions.

lumination time τ. To assure compatibility of the amplitudes between different measurement settings, we chose the illumination time τ such that 60% of the initially loaded atoms are present. On the other hand, we find that the spatial dependence of the correlation is insensitive to the illumination time τ.

At this point, the length scale of the two-body correlations $g^{(2)}(d)$ can be compared to the interaction distance of the dipolar interaction potentials that we introduced before in Section 4.1. To extract the correlation length from the data, we do not have a theoretical model to predict its shape, so we use a simple exponential fit. We fit the data with a function of the form

$$g^{(2)}(d, \Delta) \propto \exp(-d/d_c(\Delta)), \tag{4.28}$$

with $d_c(\Delta)$ the typical length scale that we want to estimate. We have chosen to fit with an exponential function to extract a characteristic length since the empirical fit matched the data well, see inset Fig. 4.13.

We took measurements with two different tweezer patterns: in a 2D array of 3×16 tweezers and with a single line of 1×16 tweezers. In both cases, we have similar results.

To compare the measured correlation length scales $d_c(\Delta)$ to the dipolar potentials involved in the facilitation process, we plot in Fig. 4.13 the dipolar pair-potentials for all the relevant pair-states couple by black-body radiation as explained previously in Section 4.3.1. We color the potential lines by their relative predicted facilitation strength, which we define as the product of the overlap of the pair-state, see Eq. (4.24), and the normalized black-body coupling rate $\Gamma_{0i}/\Gamma_{0k}^{max}$. We normalize with respect to the strongest black-body radiation coupling with a rate Γ_{0k}^{max}. Then the relative facilitation rate for a pair-state $|r_0, \bar{r}_i\rangle$ takes the form:

$$\gamma_i^{rel} = a_i \times \frac{\Gamma_{0i}}{\Gamma_{0k}^{max}}. \tag{4.29}$$

In Fig. 4.13 we can see that the length scales from the fit $d_c(\Delta)$ reproduce

the shape of the dipolar interaction potentials fan, which is approximately symmetric around the single atom resonance. We can see that the measured $d_c(\Delta)$ matches the range of the dipolar pair-potentials and reproduces their symmetry. The difference between the result from the fit $d_c(\Delta)$ and the dipolar interaction fan is caused by the exponential function that we use for the fit that does not model perfectly the data and from the atomic motion that we are going to describe in the next section.
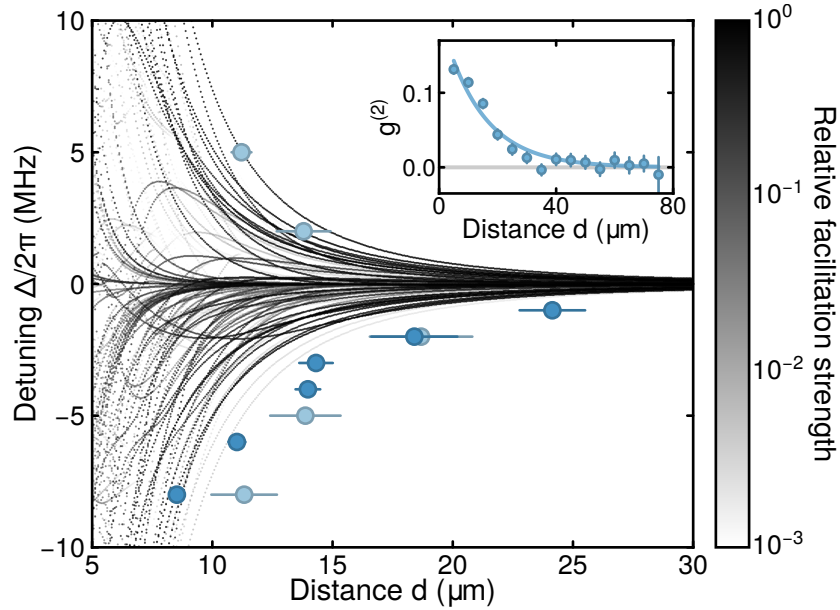
Figure 4.13: Dipolar facilitation range. The plot shows the extrapolated correlation distances $d_c(\Delta)$ in the case of a single line of atoms (light blue dots) and a 3×16 array (dark blue dots), both with spacing $5\,\mu m$. The $d_c(\Delta)$ are calculated from an exponential fit to the $g^{(2)}(d,\Delta)$. The gray shaded lines are the asymptotically collapsed dipolar pair-potentials with shading proportional to the expected logarithmic facilitation strength, as carried out in Fig. 4.10. In this case all the BBR coupled states are plotted with $n > 50$. **Inset** Example of the detected two-body correlations with the exponential fit (blue line) $g^{(2)}(d,\Delta) \propto \exp(-d/d_c(\Delta))$ to extract $d_c(\Delta)$ in the $\Delta = -2\pi \cdot 5\,\text{MHz}$. Error bars denote 1 s.e.m. in the inset and the fit errors in the main panel.

4.3.4 Effect of motion on the correlated losses

The previous section shows that the dipolar pair-potentials set the length scale of the observed correlations. However, we fail to reproduce the short distance behavior expected if we consider fixed positions for our atoms. To see that, we can calculate the rate for dipolar facilitation γ_i due to the i-th pair-potential in the low excitation fraction regime as a function of the detuning Δ and interatomic distance d. For the calculation of γ_i, we consider several factors,: the probability of an atom to be in $|r_0\rangle$, an effective Γ_{eff} rate that depends on the black-body transfer rate, the excitation rate for a resonant excitation to $|r_0\rangle$ and the lifetime of the impurity that defines the maximum time for facilitation events to occur.

The probability of an atom to be in the state $|r_0\rangle$ is given by $p_0 = \alpha(\Delta)\Omega^2/4\Delta^2$, where we include the laser phase noise factor $\alpha(\Delta)$ from Section 4.2.1.

The effective rate $\Gamma_{eff} = a_i(\Delta, d) \times \Gamma_{0i}$ incorporates the black-body radiation transfer rate Γ_{0i} for $|r_0\rangle \rightarrow |\bar{r}_i\rangle$ and the overlap of the pair-state $a_i(\Delta, d)$ defined in Eq. (4.24) as a function of the detuning and the distance. The distance dependence of the overlap comes from the pair-potential. The overlap is included to scale the resonant excitation rate.

The excitation rate to go from $|g\rangle \rightarrow |r_0\rangle$ in the resonant facilitation process is given by $\Omega^2 \times \tau_r$ where Ω is the coupling and τ_r the electronic lifetime of the Rydberg state.

We multiply by the electronic lifetime τ_r to take into account the impurity lifetime that we consider similar to the electronic lifetime of the state $|r_0\rangle$.

Combining all the parameters that we have mentioned, the facilitation rate γ_i is the following

$$\gamma_i(\Delta, d) = \Gamma_{eff}(\Delta, d)\, p_0\, \Omega^2\, \tau_r^2. \tag{4.30}$$

The total facilitation rate γ_{fac} is given then by the sum of the facilitation rates γ_i over all the black-body coupled pair-states

$$\gamma_{fac}(\Delta, d) = \sum_i \gamma_i(\Delta, d). \tag{4.31}$$

We calculate the facilitation rates in the case of two detunings $\Delta = -2\pi \cdot 2\,\text{MHz}$ and $\Delta = -2\pi \cdot 5\,\text{MHz}$ as a function of the distance d, see Fig. 4.14. The distance dependence is given by the landscape of the dipolar interaction curves. Additionally, the spatial dependence is convoluted with a Gaussian distribution with standard deviation $\sigma = 0.58\,\mu\text{m}$ to include the extent of the spatial wavefunction for the trapped atom at a temperature of $T = 200\,\text{nK}$ and at a trap depth of $3.7\,\mu\text{K}$.

The spatial dependence of the facilitation rate γ_{fac} is clearly non-exponential, contradicting our results shown in Fig. 4.13.

We can explain the discrepancy considering that the atoms are not fixed in position but are subjected to motion. The excited atoms can move since Rydberg states are not trapped by the dipole potential of the tweezer. The anti-trapping is due to the repulsive ponderomotive shift experienced by the nearly free electron. The ponderomotive force responsible for the anti-trapping has been used in the past to trap atoms in optical lattices [211]. Recently, it was used to trap both ground and excited states with a generated bottle beam trap [28]. We can calculate the repulsive ponderomotive shift in a light field of intensity $I(r)$ and angular frequency ω_L from the following formula [28]

$$U_P(r) = \frac{e^2 I(r)}{2m_e\, \epsilon_0\, c\, \omega_L^2} \tag{4.32}$$

with m_e the mass of the electron, e the electric charge, ϵ_0 the vacuum dielectric constant, c the speed of light.
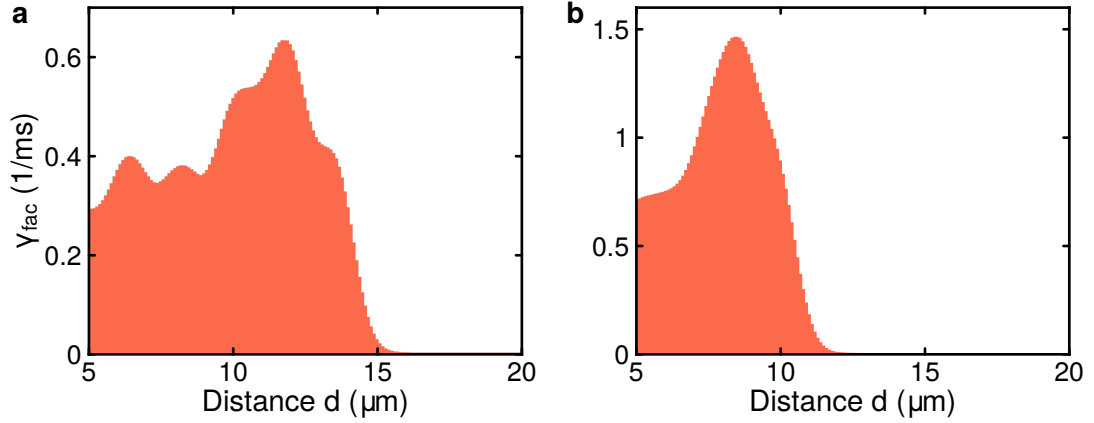
Figure 4.14: Facilitation rate as a function of distance. Calculated facilitation rate γ_{fac}, in the case of fixed distances between the atoms. **a** Facilitation rate for a detuning $\Delta = -2\pi \cdot 2\,\mathrm{MHz}$. **b** Facilitation rate for a detuning $\Delta = -2\pi \cdot 5\,\mathrm{MHz}$. The structures of both is given by the dipolar pair-potentials crossing at the selected detuning and the convolution with a Gaussian function with standard deviation $\sigma = 0.58\,\mu\mathrm{m}$ from the spatial distribution in the shallow traps.

In the case of our experiment where we use 1064 nm light for the traps, we have a ponderomotive shift of $U_P(\mathbf{r}) = 2\pi\hbar \cdot 26\,\mathrm{Hz\,cm^2/W} \cdot I(\mathbf{r})$. This shift is less then 10% different than the ground state shift.

Now we can consider all the contributions to the atomic motion. First of all, the recoil from the absorbed UV photon, with a wavelength $\lambda_{UV} = 286\,\mathrm{nm}$, transmit a velocity kick from the recoil v_{rec} to the Potassium39 atom with mass m

$$v_{rec} = \hbar \frac{k_{UV}}{m} = 36\,\mu\mathrm{m/ms}. \tag{4.33}$$

The second significant contribution is from the ponderomotive potential, which accelerates the atoms up to a velocity v_U of

$$v_U = \sqrt{2\hbar \frac{U}{m}} = 40\,\mu\mathrm{m/ms}. \tag{4.34}$$

While the thermal velocity at temperature $T = 200\,\mathrm{nK}$ is much smaller and equal to $v_T = \sqrt{k_B T/m} = 6.5\,\mu\mathrm{m/ms}$.
The different velocity contributions result in the direct motion of the Rydberg atom. The decay of the excited atoms to the ground state takes several hundred microseconds, allowing the anti-trapped Rydberg atoms to move by a few micrometers, invalidating any static picture. In Fig. 4.15 we show the classical simulation of the Rydberg atom motion in the case of a single trap. From the calculated velocities, we expect a maximal motion of $\approx 13\,\mu\mathrm{m}$ mostly parallel to the UV beam.
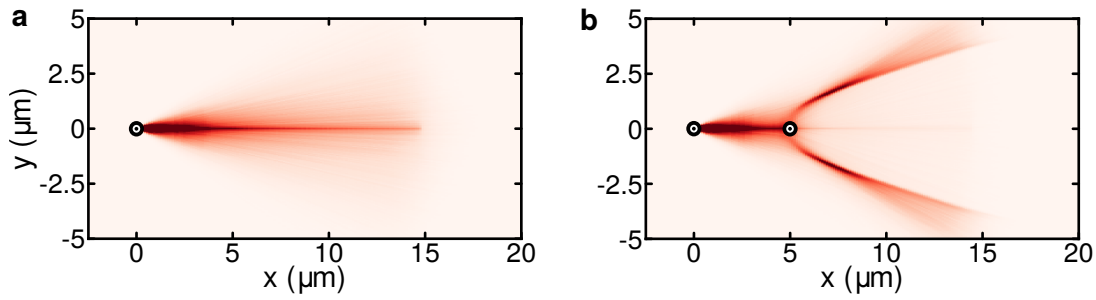
Figure 4.15: Simulation of Rydberg atom trajectories. Density plot of the trajectories obtained from a classical Monte-Carlo simulation for the motion of one Rydberg atom. The start position of the atom is marked by the circular symbol at position $(0,0)$ μm. Apparent lines in the plot are artifacts of the simulation. **a** Trajectories in the presence of only one ponderomotive potential at the start position of the atom. **b** An additional ponderomotive potential is added at $(5,0)$ μm, indicated by the second circular symbol.

The impact of the motion can be more effectively shown by the analysis of the trap lifetime locally. Taking the 3×16 pattern, we can analyze and extrapolate the trap lifetime column by column. Atoms in the first column of the array, to the UV propagation direction, have almost double the occupation lifetime compared to atoms on the other side of the array. The higher trap lifetime can be attributed to a lower effective facilitation rate as no atoms can approach from one direction. We show the results of the analysis by column in Fig. 4.16. This signal is absent without UV illumination.
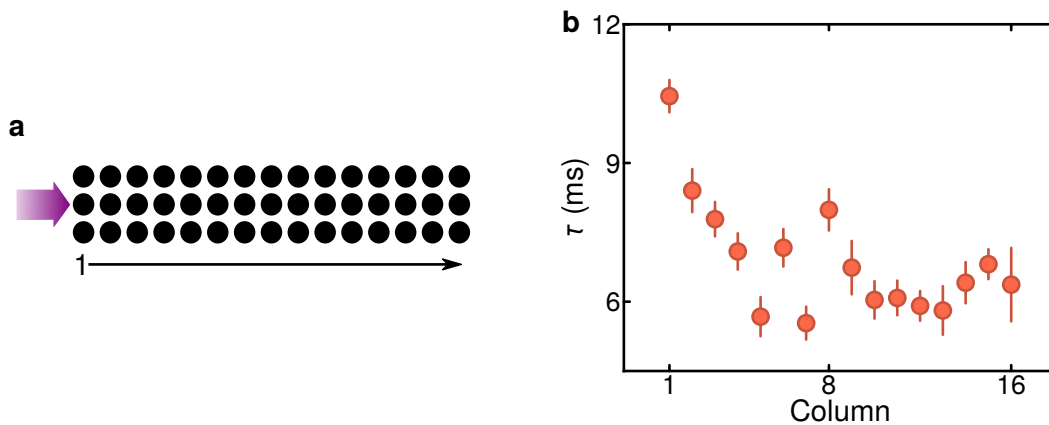
Figure 4.16: Position dependent lifetime. a Illustration of the geometry of the 3×16 array with the column numbering convention used relative to the UV propagation direction, shown by the purple arrow. **b** Plot of the lifetime for each column of the array, for a coupling $\Omega = 2\pi \cdot 2\,\text{MHz}$ and a detuning $\Delta = -2\pi \cdot 4\,\text{MHz}$. The lifetime dependence on the column position is shown.

To probe the effect of the motion to the nearest-neighbor correlations, we use arrays composed of a single line of traps and different spacings a. Then we compare the strength of the $g_{nn}^{(2)}(a)$ in the case of detunings $\Delta = -2\pi \cdot 2\,\text{MHz}$ and $\Delta = -2\pi \cdot 5\,\text{MHz}$, the results are shown in Fig. 4.17. In the case of these two

detunings, the maximal facilitation distance differs by almost a factor of two, as we show in Fig. 4.16. The experimental results, however, show that the observed distance dependence of $g_{nn}^{(2)}(a)$ for the two detunings is indistinguishable. The atomic motion samples the distances between two atoms, masking the spatial dependence of the dipolar pair-potential. The plateau shown by the nearest-neighbor correlations $g_{nn}^{(2)}(a)$ is generated by the typical flight distance of the Rydberg atoms within their electronic lifetime. We have to add the dipolar pair-potentials spatial dependence to the flight distance, increasing the possible facilitation and correlated loss range.
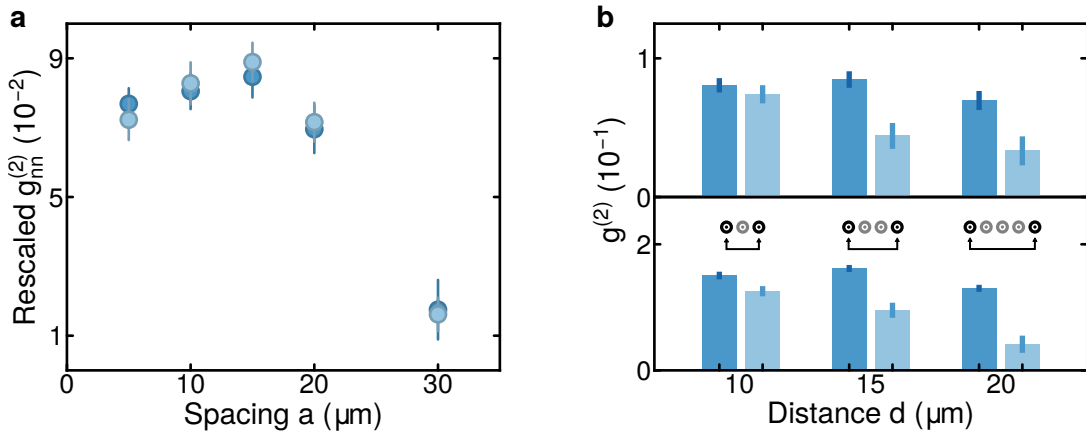
Figure 4.17: Two-body correlation as a function of the array spacing and with ponderomotive barriers. a Next-neighbour correlation $g_{nn}^{(2)}$ in a 1D chain of traps versus the spacing of the traps a. Measurement done for detuning $\Delta = -2\pi \cdot 2\,\mathrm{MHz}$ dark blue dots and $\Delta = -2\pi \cdot 5\,\mathrm{MHz}$ light blue dots. The correlation amplitude is scaled globally to the same average amplitude. **b** Histograms for $\Delta = -2\pi \cdot 2\,\mathrm{MHz}$ on top and $\Delta = -2\pi \cdot 5\,\mathrm{MHz}$ at the bottom, showing the effect of a ponderomotive barrier between two tweezers, see illustration in the figure. The dark blue bars correspond to the case of no ponderomotive barrier in between the tweezers at the respective distance. The light blue bars instead correspond to the case with at least one barrier in between. The correlation is calculated on a subset of the data through post-selection. The data in the light blue columns was postselected in a way that the tweezers in between the set distance were empty after the initial loading of the array. Error bars denote 1 s.e.m.

The previous results seem to contradict the observation made in Section 4.3.3. However, we have to take into account the presence of other tweezers. The recoil energy and the ponderomotive potential height are quite similar, respectively $\hbar k_{UV}/k_B = 3\,\mu\mathrm{K}$ and $U_P/k_B = 3.7\,\mu\mathrm{K}$. Then the next trap in the line of motion will repel a moving Rydberg atom with the result of an effective "shielding" for the next-nearest-neighbors atoms. The classical simulation in Fig. 4.15 confirms the "shielding" effect. Only a small fraction of the atoms can overcome the ponderomotive potential, in the case of the thermal velocity aligning them exactly on the axis of the other trap.

To confirm this idea also in terms of correlations with our data, we evaluated the

two-point correlation $g^{(2)}(d)$ for three different distances d for the two detunings taken into account. For each distance, we compare the correlation value for the nearest neighbor with the case when one or more potential barriers are present. We took the nearest-neighbor measurement with different pattern spacings a, while in the other case, we use a pattern spacing of $a = 5\,\mu$m. In evaluating the correlation amplitudes for the case with one or more potential barriers, empty traps, present in-betweens, we perform a post-selection over the measurements by selecting those cases where the traps in between the two positions are empty in the first image. In Fig. 4.17 are displayed the results of our evaluation. The correlation amplitude is almost independent of the distance for nearest-neighbors, without any potential barriers in between. In contrast, when at least one potential barrier is present, the correlation amplitude decreases with distance. The effect is stronger for the larger detuning, where we have a smaller dipolar range. The correlations prove that the motion and presence of traps make a difference since, from a static picture, we do not expect any dependence on empty traps between two positions for the correlation value.

The effect of motion could mask the spatial dependence of the facilitation if it were not for the "shielding" effect that we have shown. The distance dependence of the two-body correlations is smoothened but allows us to measure a distance dependence compatible with the dipole interaction curves in Fig. 4.13.

4.3.5 Avalanche losses

In the previous sections, we considered the case where the excitation fraction is relatively low and the avalanche effect of the facilitation is small. The avalanche effect is when a chain of facilitation events is triggered one after another. The already facilitated atom $|r_0\rangle$ is transferred to an opposite parity state $|\bar{r}_i\rangle$ by black-body radiation and triggers the facilitated excitation of other nearby atoms.

This avalanche mechanism has been observed before in the case of Rubidium atoms trapped in an optical lattice in a Mott insulator configuration with almost unit filling and illuminated with UV light, see reference [58]. The atom number histogram of several experimental realizations shows two bimodal peaks, one for the case of a triggered avalanche loss and one where the avalanche loss did not occur.

We do not have unity filling of our traps since we have only 50% loading probability. The low array filling reduces the avalanche effect since it can occur only for atoms within the dipolar range with the addition of atomic motion.

To test the presence of an avalanche mechanism we evaluate the two-point correlations in the 3×16 geometry with $a = 5\,\mu$m spacing for increasing Rabi frequency coupling at a fixed detuning $\Delta = -2\pi \cdot 3\,$MHz while fixing the total fraction of remaining atoms at 80%.

We show the measurements results in Fig. 4.18, we can see that both the range and the amplitude of the two-body correlations increase with the increase of the Rabi coupling. A noticeable effect is the comparable correlation amplitude between the two ends of the array (almost 80 μm apart) in the two extreme cases of Rabi coupling, the nearest-neighbor distance for the lowest Rabi coupling and the largest distance for the highest Rabi coupling.
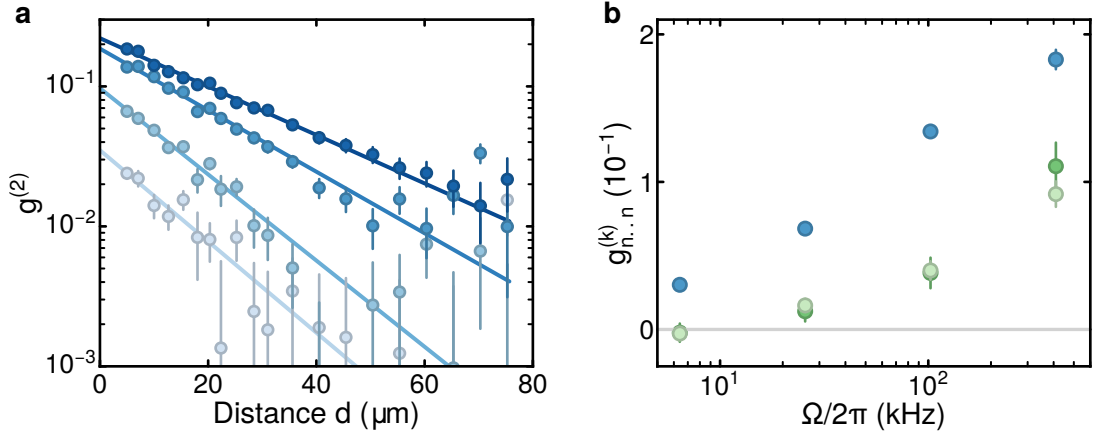
Figure 4.18: Avalanche facilitated excitation. a Two-point correlations $g^{(2)}$ vs. distance for different coupling strength in a 3×16 array with $5\,\mu m$ spacing. The Rabi coupling is increased from light to dark blue as $\Omega = 2\pi \cdot (6,25,102,410)\,kHz$ with the pulse time adjusted to fix the fraction of lost atoms at 20%. Exponential fits are shown as solid lines. **b** Multi-point correlations vs. coupling strength. The values are plotted for the shortest distance connected multi point correlations $g_{n..n}^{(k)}$ along the x-axis. The correlations are shown for $k = 2$ in blue, $k = 3$ in light green and $k = 4$ in dark green. Error bars denote 1 s.e.m.

Another test would be to check for higher-order correlations since we would expect several facilitations events. We can define a connected k-point correlation, where we consider k subsequent trap positions along the UV light propagation direction with the shortest possible array spacing that we use $a = 5\,\mu m$

$$g_{n..n}^{(k)} = \langle \prod_{j=0}^{k}(n_{x+ja} - \langle n_{x+ja}\rangle)\rangle \tag{4.35}$$

where n_{x+ja} is the occupation operator for the position $x + ja$ and the average is done over all the experimental realizations and the possible combination of the x value. In Fig. 4.18 the results are shown of the evaluation for three- and four-point connected correlations compare to with the two-point nearest-neighbour correlation values $g_{nn}^{(2)}$. With the increase of the Rabi coupling, the amplitude of the nearest-neighbor correlations increases in a quadratic way, as we expect from Eq. (4.30). At the same time, the amplitude of the higher-order connected correlations grows, certifying the presence of subsequent facilitation processes, an indication of the process's avalanche characteristic.

We can also evaluate the distribution of lost atoms for an illumination time with a loss fraction of 40%. The distributions are shown in Fig. 4.19. After an exposure time, the distribution is shifted towards higher values and is broadened. If we apply a post-selection on the data, we select only the measurements with an initially loaded atom number equal or higher than 26, corresponding to 54% of the tweezers loaded. The distribution is even broader and flatter, which hints at the start of the formation of the bimodality shown in previous experiments.

The difference with our experiment is the higher atomic density that allowed them to reach the avalanche regime fully, see references [58, 212].
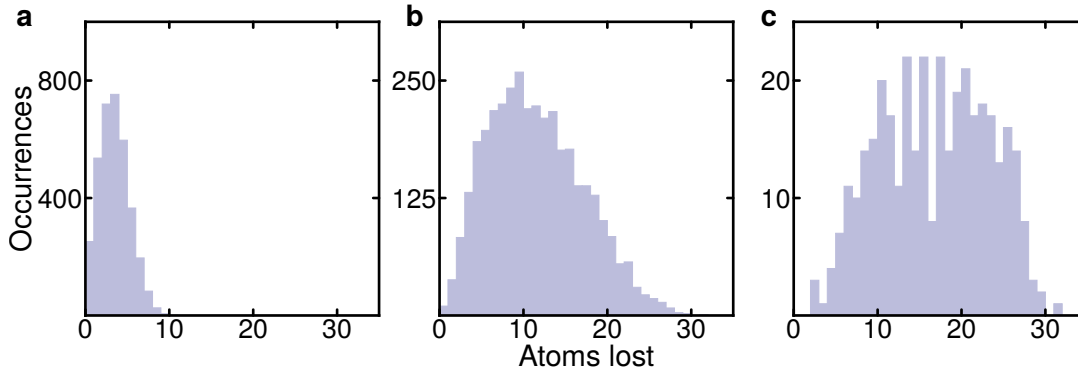

Figure 4.19: Atom loss distribution. Distribution of lost atoms in the case of strong coupling at $\Delta = -2\pi \cdot 3\,\mathrm{MHz}$ and $\Omega = 2\pi \cdot 420\,\mathrm{kHz}$. **a** Distribution without UV exposure, where the loss is only due to the imaging process. **b** Exposure time fixed in a way that 40% of the atoms are lost. **c** Same setting as for the center histogram, but with a data postselection where only the experimental realizations with more than 26 initially loaded atoms are taken into account.

4.4   Summary and Outlook

This chapter gives an outlook of the interaction between Rydberg atoms and how we can use them to implement interesting physical systems. We have shown the first realization of Rydberg dressed interaction with atoms trapped in optical tweezers in our experiment.

We have then investigated the reduction of the dressing lifetime due to the presence of contaminants generated by black-body radiation induced. The black-body radiation transfer excited atoms to nearby Rydberg states with opposite parity. Such an effect opens facilitation channels with characteristic facilitation distances given by the interaction strength and detuning $\propto \sqrt[3]{C_3/\Delta}$. With the evaluation of two-body correlations, we extracted a length scale that matched the calculated facilitation distances. We have also excluded the possibility of an important contribution by Coulomb facilitation due to the ionization of the initially excited Rydberg atom and the electric field generated by it. The photo-ionization probability from the trap light is negligible. We see that the correlation is non-zero for both negative and positive detunings. In the case of an electric field generated by an ion, we should see facilitation only for negative detunings. Moreover, we have shown the effect of the recoil triggered directed motion of the excited Rydberg atoms, which are no longer confined by the traps. Motion leads to a smoothening of the two-body correlation as a function of distance. However, it does not hinder the observation of the typical facilitation length thanks to an effective "shielding" effect.

Lastly, we have also estimated higher-order connected correlation functions that show the presence of a cascade effect for the facilitated excitations. We also note that the effect is more prominent when more traps are initially loaded, meaning that it is more detrimental in the case of a unitary filled array or optical lattice.

One technique proposed to reduce the detrimental effect of facilitation for Rydberg dressing is so-called stroboscopic dressing. This method relies on a Ramsey sequence where UV pulses of short length are followed by periods of time without any UV light to allow any possible atom excited to Rydberg to decay back to the ground state. The Rydberg admixture determines the length of the UV pulses. The black-body transition rate, together with the Rydberg states' lifetime, determines the length of the interval between two UV pulses. The technique has been already experimentally tested in references [60, 165].

Another approach that requires some experimental design effort would be to locate the experiment in a cryostat at a temperature $T = 4\,\mathrm{K}$. The design requires careful planning regarding the optical access since any aperture should be smaller than the wavelength of the black-body radiation that we want to block from entering the experimental volume. These kinds of experiments were already developed for ion-trapping as in reference [130], and recently one was also built specifically for a tweezer experiment, see reference [131]. An extra advantage is the improved vacuum quality, which significantly increases the occupation lifetime of the trapped atoms.

In the case of our experiment, a general improvement of the UV laser system will be implemented to reach the theoretical lifetime for a single dressed atom. Then a couple of techniques could be implemented to reduce or prevent dephasing from facilitated losses:

- **Removal of excited atoms:** The possibility to control the Rydberg atom motion by repulsive trapping potentials can be another solution to circumvent catastrophic avalanche dephasing in one- or two-dimensional Rydberg-dressed systems. One can implement a light-sheet potential at a wavelength chosen to trap the ground state atoms but repel the Rydberg atoms. In this configuration, the atoms excited to Rydberg are accelerated away from the atomic plane. The shift given by the anti-trapping potential should be strong enough to make the vertical motion dominant and minimize the one on the atomic plane. Moreover, the displacement should happen in a faster time than the BBR induced transition rate.
  We show in Fig. 4.20 the simulation of such anti-trapping potential, generated from an elliptical Gaussian beam with waist respectively $w_z = 3\,\mu\mathrm{m}$ and $w_x = 50\,\mu\mathrm{m}$. From the simulation, we can see that the atoms are expelled from the atomic plane and are not able to reach the nearest-neighbor at $5\,\mu\mathrm{m}$ distance. The histogram of the sampled distances shows that the atomic motion cannot significantly reduce the distance to the nearest neighbor within the simulation parameters. We can calculate from the simulation a time between $10 - 15\,\mu\mathrm{s}$ to reach again a distance of $5\,\mu\mathrm{m}$ from the nearest-neighbor position considering repulsive potentials with heights $U_{dip} = 2\pi\hbar \cdot 20\,\mathrm{MHz}$ and $U_{dip} = 2\pi\hbar \cdot 10\,\mathrm{MHz}$. The simulation shows that we can quickly eliminate the excited atoms from the atomic plane to avoid starting a facilitation process.
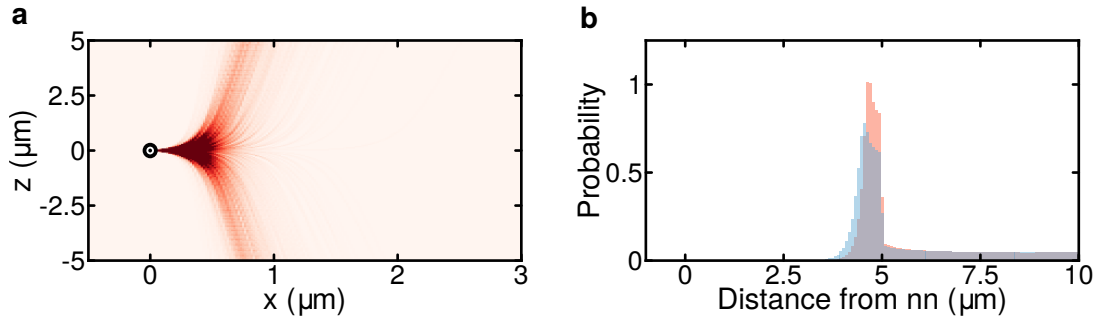
Figure 4.20: Removal of excited atoms. a Density plot of the trajectories obtained with a classical Monte-Carlo simulation for the motion of one Rydberg atom. In the simulation, we consider a single tweezer that propagates along the z-axis and an elliptical light beam with $w_z = 3\,\mu m$ and $w_x = 50\,\mu m$ that can be used as a dipole trap for the atoms in the ground state. The Rydberg atom sees a repulsive potential from the tweezer $U_{twe} = 2\pi\hbar \cdot 77\,kHz$ and one from the elliptical dipole trap beam of $U_{dip} = 2\pi\hbar \cdot 20\,MHz$. The atom receives a kick from the absorbed UV photon and has an initial velocity from its temperature as in the simulation in Section 4.3.4. We can see that the atoms are quickly accelerated away from the atomic plane in the vertical direction. If we consider an array spacing of $a = 5\,\mu m$ we can see that the atom is not able to reach its nearest neighbor compared to the simulations shown in Fig. 4.15. **b** We plotted the histogram of the normalized distribution of the sampled distances calculated between the moving atoms and the nearest-neighbor position. The atom starts at a 5 μm distance from the nearest neighbor. The red histogram is done with simulation for a repulsive potential of the dipole beam of $U_{dip} = 2\pi\hbar \cdot 20\,MHz$, the blue one is for $U_{dip} = 2\pi\hbar \cdot 10\,MHz$. In both cases, the atoms are not able to reach the neighbor position, and the distance increases quickly.

- **Depumping of contaminants:** Another method to consider would be to depump the states populated by the BBR transitions. The depumping must be done faster than the possible facilitated excitation rate. In the case of Potassium39 one could use 973 nm light to couple $|nS\rangle$ and $|nD\rangle$ states to the lower fast decaying $|5P\rangle$ state, a schematic is shown in Fig. 4.21. The states with the strongest black-body coupling are a few tens of GHz away from the $|62P\rangle$ state. Knowing their difference in energy, one can address them all using a fiber-coupled EOM to apply appropriately spaced sidebands to the depumping laser and address all the states. In terms of available laser power, it is possible to produce several hundreds of mW at 973 nm with amplification and reach depumping couplings on the order of one MHz easily. The technique could be particularly interesting in the event where a magic wavelength was chosen between the ground state and the Rydberg state [48, 213]. The atoms are not lost and can be reused for another experiment, while state-dependent imaging could solve the possible error in the detection due to mixing of states from the depumping [116, 123].
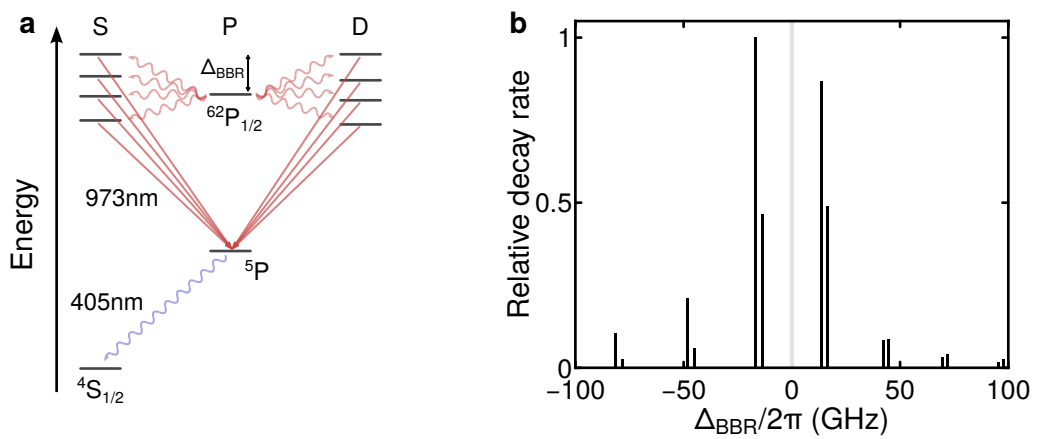
Figure 4.21: Depumping of contaminants. a Level scheme for the depumping. A ~ 973 nm laser with sidebands can depump the contaminants to the intermediate $5P$ state. From the $5P$ states the atoms can decay back to the ground state with the emission of a 405 nm photon. **b** The black bars mark the difference in energy $\hbar\Delta_{BBR}$ between the $|62P\rangle$ state and the black-body coupled states. The amplitude of the bar marks also the coupling strength. The x-axis of the plot has been restricted showing the most significantly coupled states.

Chapter 5

Conclusions and Outlook

In this thesis, we described our novel experimental apparatus for the trapping of Potassium atoms in optical tweezers and their use for quantum simulation. The first part gives an overview of the experimental apparatus, focusing on the vacuum chamber and the cooling techniques to prepare cold atomic samples. Then, we provide an overview of the setup for the generation and handling of the UV light that we need for the coupling to Rydberg states.

In the second part, we describe how we generate arrays of optical tweezers through a holographic technique. It follows a detailed explanation of the method we implemented for loading and imaging the atoms into the tweezers. The technique consists of modulating the laser intensity for both trapping and cooling light to avoid the strong light shifts generated by the former.
We show that we can prepare single atoms into our traps and image them. We demonstrate a fidelity $> 99\%$ for the detection of trapped atoms through fluorescence imaging, which presents a low probability $\sim 3\%$ of losing an atom during the imaging process.
We report our attempt to increase the loading probability, which is limited to 50% by pair projection, through an optical shielding technique. We use the gray molasses technique, as also shown in [137], to cool atoms both in free space and inside the tweezers, and at the same time, we apply optical shielding. We demonstrate that we can load atoms into the traps using the gray molasses technique. As a result, we see an increase in the loading probability for single tweezers, with a measured maximum value of $\approx 70\%$, while the average loading probability for the array of $\approx 60\%$. The limited enhancement in loading probability is due to the strong light shift generated by the trapping light, making it challenging to well-define the conditions for the enhancement of the loading probability.

In the last part, we demonstrate the first result regarding off-resonant Rydberg dressed interactions with the application of the various techniques that we have described. We generated the interactions between atoms arranged in a one-dimensional array. We use Ramsey interferometry to detect the induced interactions. The result is the building up two-body correlations between the atoms. We can not see any coherent dynamics since the light shifts inhomogeneity generated by the traps limits us. The problem should be solved with the improved efficiency of the Raman sideband cooling that allows us to reduce the trap depth to a point where the inhomogeneities in the light shifts are negligible. We also see that the phase noise of the laser limits the dressed state lifetime by measuring with non-interacting atoms.

With the measurement of the dressed state lifetime, we can also distinguish two different regimes, depending on the distance between the atoms. With close distanced atoms, we observe a significant reduction of the dressed lifetime. We connect this lifetime reduction to a facilitated excitation mechanism started by combining an off-resonantly excited atom and black-body radiation-induced transfer to close by Rydberg state. The black-body radiation transfers the atom to a Rydberg state with opposite parity with regard to the initial one. This state determines a change in the interaction scaling, going from a van-der-Waals interaction $\propto 1/d^6$ to a dipole one $\propto 1/d^3$, shifting to resonance the dressed state. Such an effect has already been reported and visualized as a broadening effect in the excitation transition. To probe the length scaling, we evaluate two-body correlations over a closely spaced array.

Such correlations are present only due to the facilitated excitation process. From the correlation signal, we can extract a characteristic length scale that matches the predicted facilitation distances from the dipole interaction, considering all the possible states coupled by black-body radiation. In this way, we can explain the smooth correlation landscape through the motion of the excited atoms. The excited atoms are no longer confined by our traps and move in the same direction as the UV beam. The motion does not ultimately increase the facilitation length scale due to the traps' 'shielding' effect. The traps create repulsive ponderomotive potentials that make a kinetic barrier for the moving atoms, shielding the traps coming after. We evaluate connected correlations for chains of three and four atoms finding a non-zero correlation signal demonstrating a chain effect of the facilitation mechanism. Such an effect increases quadratically with the coupling strength as predicted. The increase is the onset of an avalanche mechanism seen with other systems, which is mitigated in our case by the initial random filling of the array.

We then discuss possible solutions to mitigate the problem for future Rydberg dressing experiments in the case of large-scale quantum many-body systems.

5.1 Outlook

Now we will discuss the future improvement and possible solutions to the limitations that we have found in our experiment:

- **Coherent interactions:** An essential parameter for the realization of quantum simulation experiments or quantum computing is the number of coherent interactions N that is possible to have. In our system, we can observe a maximum number of $N \approx 4$, limited by phase and intensity noise of the laser, in the case of resonant excitation. The state of the art of coherent interactions for Rydberg atoms in optical tweezers is $N \approx 50$ [45, 54, 55]. The high number of coherent interactions was achieved using Rabi frequencies in a few MHz range and reducing the phase noise of the laser. The improvement in phase noise can be attributed to filtering the driving laser with an optical cavity or using titanium-sapphire lasers with intrinsically low phase noise. We have designed a filter cavity for our UV laser seed. Details about the cavity can be found in the thesis of Joop Adema [214],

which will be a future update for our experiment.

- **Arrays inhomogeneities:** As we demonstrate, we have inhomogeneities in the light shift generated by each tweezer, with a variation of around $\approx 10\%$ to the mean shift. In our case, this is due to uncompensated aberrations. In the case of the Rydberg dressing technique, this uncontrolled light shift is a problem since it is in the order of the laser detuning used for the dressing. The available laser power limits such detuning, and it is not easy to increase. However, thanks to Raman sideband cooling, we can reduce the tweezers trap depth by a factor of 200. The reduction makes the absolute inhomogeneous shifts negligible for Rydberg dressing.
  Another possible solution is to implement feedback techniques with direct measurements from the atoms [92]. However, this requires a time effort since each optimization step requires measurements.
  An alternative solution is to transfer the initially loaded, and cooled atoms from the tweezers into an optical lattice [32]. The optical lattice provides a uniform light shift and a smaller spacing than the tweezer size, facilitating sideband cooling. This approach combines the advantage of fast cycle times of optical tweezers experiments with those of optical lattices.

- **Black-body radiation-induced facilitation:** Black-body radiation at room temperature reduces the long radiative lifetimes of Rydberg atoms. As we have shown, this is critical for off-resonant experiments due to the possibility of triggering an avalanche of excitations to Rydberg, reducing the dressed state lifetime. It has been shown that a large detuning can reduce this effect [186], but a strong coupling is required to keep the interaction constant.
  One proposed solution is to implement dressing in a stroboscopic way, turning on and off the dressing light to allow off-resonantly excited atoms to decay back to their ground state [60]. We propose two techniques that could help mitigate the effect. One requires the optical depumping of the states populated by the black-body radiation. We can perform depumping using one step of the two-photon inverted-ladder scheme to excite atoms to Rydberg states [69] and depump the black-body radiation populated states.
  The second technique exploits the ponderomotive force from a large optical trap made with an elliptic beam tight along the weak axis of the tweezers. A strong ponderomotive potential pushes the excited atoms along the vertical direction, away from the atomic plane. We can implement these two easily in our setup.
  An alternative solution would be to operate the experiment inside a cryostat at $4\,\mathrm{K}$ to suppress black-body radiation. However, a cryostat requires an engineering effort to plan the optical access and dampen the vibrations from the cryostat. Another benefit is the increase of the occupational lifetime thanks to the improved vacuum quality as demonstrated in Reference [131] in a newly built tweezer experiment.

- **Sorting of atoms and deterministic loading:** Reliable sorting of atoms in optical tweezers arrays broadened their scope in the study of quantum

many-body systems and quantum computing. Problems arise with the scaling up of systems when the sorting time becomes quite long. New sorting techniques have already been developed to solve these problems [92, 215]. We are also going to implement sorting with our arrays using AODs and enhanced sorting techniques. A description of the technique can be found in the thesis of Robin Eberhard [125].
Deterministic loading could be another strategy to speed up the sorting increasing the loading probability and reducing the sorting times [137].

- **State-selective imaging and repetition rate:** At the time of writing, experiments with tweezers and Rydberg atoms are an order of magnitude faster than standard ultra-cold atom experiments. The reduced duty cycle is thanks to the fast preparation of the system and the strong interaction between Rydberg atoms. Usually, the atoms excited to Rydberg are identified by a loss from a previously filled tweezer since the tweezer light does not trap them. The mapping of spins on different ground states allows for the imaging of both states without loss of the atoms [116, 123], concerning what we described in this thesis. The technique would make it possible to initialize the system again to perform a second experiment. We can potentially repeat the process many times, limited by the occupation lifetime and loss during imaging. The possibility to reinitialize the sample can improve the $\sim 1\,\mathrm{Hz}$ repetition rate of current experiments, possibly up to a factor of ten. Other experiments have shown negligible loss during imaging and resulted in the first test of such an idea [123].

In our experimental apparatus, the next step to be implemented is the sorting of the atoms in the traps for the preparation of unitary filled arrays [125], with the possibility to try again to deterministically load atoms into traps made by the AODs that we are going to use for the sorting.
The system is then ready to test the proposed techniques to reduce the black-body radiation induced facilitation mechanism for off-resonant Rydberg coupling.
After these improvements, the system is ready to start the realization of engineering of complex Hamiltonians thanks to the Rydberg dressing technique that presents tunable angular and distance-dependent interactions [53, 57, 63].

Optical tweezers combined with Rydberg atoms are a promising platform for new experiments for quantum simulation and quantum computation. They offer the possibility to realize configurable arrays of traps and the possibility of engineering interaction between the atoms. Our experiment is a good candidate for further investigating such problems and studying quantum many-body systems.

Appendix

A Error estimation for correlation measurements

To estimate the errors regarding the results of the two-, three- or four-body correlations that we have presented in this thesis we have used the bootstrap method to estimate their uncertainty. Depending on the size of the measurements one can use different methods to calculate uncertainty. A diffused bootstrap method is called the Jackknife sampling method [216, 217], which can be cumbersome in the case of large sets of data. I will begin by explaining the bootstrap method that we have implemented called re-sampling bootstrap.

Considering a sample of data $X_1, ..., X_n$ from a distribution P. From the data, we can define an empirical distribution P_n and the estimator evaluated on it $\hat{\theta}_n = g(X_1, ..., X_n)$. We want to find the variance of the estimator $\text{Var}_P(\hat{\theta}_n)$. For the estimation of the variance, we can follow these steps. One extract a sample from P, the sample is given by drawing n observations. Once the sampling is done one can calculate the estimator value on the data and repeat this N times.

$$
\begin{aligned}
\text{draw} \quad & X_1, ..., X_n \\
\text{compute} \quad & \hat{\theta}_n^{(1)} = g(X_1, ..., X_n) \\
\text{draw} \quad & X_1, ..., X_n \\
\text{compute} \quad & \hat{\theta}_n^{(2)} = g(X_1, ..., X_n) \\
& \vdots \\
\text{draw} \quad & X_1, ..., X_n \\
\text{compute} \quad & \hat{\theta}_n^{(N)} = g(X_1, ..., X_n)
\end{aligned}
$$

Then the sample variance s^2 can be calculated over the N evaluations $\hat{\theta}_n^{(1)}, ..., \hat{\theta}_n^{(N)}$

$$
s^2 = \frac{1}{N} \sum_{j=1}^{N} (\hat{\theta}_n^{(j)})^2 - \left(\frac{1}{N} \sum_{j=1}^{N} \hat{\theta}_n^{(j)} \right)^2
$$

We can make N large enough so that $s^2 \approx \text{Var}_P(\hat{\theta}_n)$, the variance of is approximated by the repeated observations n from P. Since P is not known beforehand the observations can be taken from the empirical distribution P_n and it can be expected that $\text{Var}_P(\hat{\theta}_n) = \text{Var}_{P_n}(\hat{\theta}_n)$.
Now P_n is simulated by randomly sampling from the experimental realizations, also, by taking the same measurement several times and applying the algorithm shown before. The data is sampled N times and the estimator is evaluated $\hat{\theta}_n^* = g(X_1^*, ..., X_n^*)$. From the evaluated estimators the variance can be calculated

$$\hat{s}^2 = \frac{1}{N} \sum_{j=1}^{N} (\hat{\theta}^*_{n,j} - \bar{\theta})^2$$

with $\bar{\theta} = 1/N \sum_{j=1}^{N} \hat{\theta}^*_{n,j}$. The error on the estimation can be reduced by giving a large value to n and N.

In Fig. 1 an example of evaluation of the estimator $\hat{\theta}^*_n$ is shown which in our case corresponds to the two-body correlation $g^{(2)}$. This should produce a Gaussian distribution for an appropriately large N from which the variance can be calculated.

Applying this method to estimate the uncertainty for the correlations since the relative datasets we have been comprised of $10 - 20 \cdot 10^3$ experimental realizations. With the resampling method the estimation of uncertainty is faster then with the jackknife method, but still reliable with a number of resamplings $N = 10^3$.
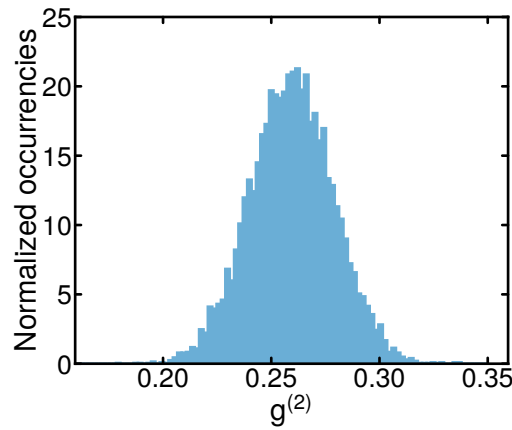
Figure 1: Re-sampling distribution. Distribution of the calculated two-body correlation $g^{(2)}$ from real experimental data with the application of the resampling method. The two-body correlation is calculated by randomly sampling the experimental data. Each sample has the same size of the experimental data and can contain several copies of the data. The sample is formed by selecting with a uniform random distribution the data. $N = 10^3$ resamplings were made to produce the histogram in the figure.

Bibliography

[1] J. Prodan, A. Migdall, W. D. Phillips, I. So, H. Metcalf, and J. Dalibard. *Stopping Atoms with Laser Light*. Physical Review Letters **54**, 992–995 (1985). (Cited on page **1**)

[2] S. Chu, L. Hollberg, J. E. Bjorkholm, A. Cable, and A. Ashkin. *Three-dimensional viscous confinement and cooling of atoms by resonance radiation pressure*. Physical Review Letters **55**, 48–51 (1985). (Cited on page **1**)

[3] K. B. Davis, M. O. Mewes, M. R. Andrews, N. J. van Druten, D. S. Durfee, D. M. Kurn, and W. Ketterle. *Bose-Einstein Condensation in a Gas of Sodium Atoms*. Physical Review Letters **75**, 3969–3973 (1995). (Cited on page **1**)

[4] M. H. Anderson, J. R. Ensher, M. R. Matthews, C. E. Wieman, and E. A. Cornell. *Observation of Bose-Einstein Condensation in a Dilute Atomic Vapor*. Science **269**, 198–201 (1995). (Cited on page **1**)

[5] B. DeMarco. *Onset of Fermi Degeneracy in a Trapped Atomic Gas*. Science **285**, 1703–1706 (1999). (Cited on page **1**)

[6] M. R. Andrews, C. G. Townsend, H.-J. Miesner, D. S. Durfee, D. M. Kurn, and W. Ketterle. *Observation of Interference Between Two Bose Condensates*. Science **275**, 637–641 (1997). (Cited on page **1**)

[7] I. Bloch, T. W. Hänsch, and T. Esslinger. *Atom Laser with a cw Output Coupler*. Physical Review Letters **82**, 3008–3011 (1999). (Cited on page **1**)

[8] A. G. Truscott, K. E. Strecker, W. I. McAlexander, G. B. Partridge, and R. G. Hulet. *Observation of Fermi Pressure in a Gas of Trapped Atoms*. Science **291**, 2570–2572 (2001). (Cited on page **1**)

[9] F. Schreck, L. Khaykovich, K. L. Corwin, G. Ferrari, T. Bourdel, J. Cubizolles, and C. Salomon. *Quasipure Bose-Einstein Condensate Immersed in a Fermi Sea*. Physical Review Letters **87**, 080403 (2001). (Cited on page **1**)

[10] C. A. Regal, M. Greiner, and D. S. Jin. *Observation of Resonance Condensation of Fermionic Atom Pairs*. Physical Review Letters **92**, 040403 (2004). (Cited on page **1**)

[11] M. Greiner, O. Mandel, T. Esslinger, T. W. Hänsch, and I. Bloch. *Quantum phase transition from a superfluid to a Mott insulator in a gas of ultracold atoms*. Nature **415**, 39–44 (2002). (Cited on page **1**)

[12] S. R. Jefferts, J. Shirley, T. E. Parker, T. P. Heavner, D. M. Meekhof, C. Nelson, F. Levi, G. Costanzo, A. D. Marchi, R. Drullinger, L. Hollberg, W. D. Lee, and F. L. Walls. *Accuracy evaluation of NIST-F1*. Metrologia **39**, 321–336 (2002). (Cited on page **1**)

[13] M. Takamoto, F.-L. Hong, R. Higashi, and H. Katori. *An optical lattice clock*. Nature **435**, 321–324 (2005). (Cited on page **1**)

[14] A. D. Ludlow, M. M. Boyd, T. Zelevinsky, S. M. Foreman, S. Blatt, M. Notcutt, T. Ido, and J. Ye. *Systematic Study of theSr87Clock Transition in an Optical Lattice*. Physical Review Letters **96**, 033003 (2006). (Cited on page **1**)

[15] W. S. Bakr, J. I. Gillen, A. Peng, S. Fölling, and M. Greiner. *A quantum gas microscope for detecting single atoms in a Hubbard-regime optical lattice*. Nature **462**, 74–77 (2009). (Cited on pages **1**, **38**, and **39**)

[16] J. F. Sherson, C. Weitenberg, M. Endres, M. Cheneau, I. Bloch, and S. Kuhr. *Single-atom-resolved fluorescence imaging of an atomic Mott insulator*. Nature **467**, 68–72 (2010). (Cited on pages **1**, **38**, and **39**)

[17] L. W. Cheuk, M. A. Nichols, M. Okan, T. Gersdorf, V. V. Ramasesh, W. S. Bakr, T. Lompe, and M. W. Zwierlein. *Quantum-Gas Microscope for Fermionic Atoms*. Physical Review Letters **114**, 193001 (2015). (Cited on pages **1**, **36**, and **39**)

[18] A. Omran, M. Boll, T. A. Hilker, K. Kleinlein, G. Salomon, I. Bloch, and C. Gross. *Microscopic Observation of Pauli Blocking in Degenerate Fermionic Lattice Gases*. Physical Review Letters **115**, 263001 (2015). (Cited on page **1**)

[19] M. F. Parsons, F. Huber, A. Mazurenko, C. S. Chiu, W. Setiawan, K. Wooley-Brown, S. Blatt, and M. Greiner. *Site-Resolved Imaging of Fermionic Li6 in an Optical Lattice*. Physical Review Letters **114**, 213002 (2015). (Cited on pages **1** and **39**)

[20] N. Schlosser, G. Reymond, I. Protsenko, and P. Grangier. *Sub-poissonian loading of single atoms in a microscopic dipole trap*. Nature **411**, 1024–1027 (2001). (Cited on pages **1**, **25**, **34**, **40**, and **55**)

[21] A. M. Kaufman, B. J. Lester, C. M. Reynolds, M. L. Wall, M. Foss-Feig, K. R. A. Hazzard, A. M. Rey, and C. A. Regal. *Two-particle quantum interference in tunnel-coupled optical tweezers*. Science **345**, 306–309 (2014). (Cited on pages **1** and **2**)

[22] S. Murmann, A. Bergschneider, V. M. Klinkhamer, G. Zürn, T. Lompe, and S. Jochim. *Two Fermions in a Double Well: Exploring a Fundamental Building Block of the Hubbard Model*. Physical Review Letters **114**, 080402 (2015). (Cited on pages **1** and **2**)

[23] M. Endres, H. Bernien, A. Keesling, H. Levine, E. R. Anschuetz, A. Krajenbrink, C. Senko, V. Vuletic, M. Greiner, and M. D. Lukin. *Atom-by-atom assembly of defect-free one-dimensional cold atom arrays*. Science **354**, 1024–1027 (2016). (Cited on pages **1**, **25**, **34**, **40**, **51**, **54**, and **55**)

[24] D. Barredo, S. de Léséleuc, V. Lienhard, T. Lahaye, and A. Browaeys. *An atom-by-atom assembler of defect-free arbitrary two-dimensional atomic arrays*. Science **354**, 1021–1023 (2016). (Cited on pages **1**, **25**, **34**, **40**, **51**, **54**, and **55**)

[25] H. Kim, W. Lee, H. gyeol Lee, H. Jo, Y. Song, and J. Ahn. *In situ single-atom array synthesis using dynamic holographic optical tweezers*. Nature Communications **7** (2016). (Cited on page **1**)

[26] W. Lee, H. Kim, and J. Ahn. *Defect-free atomic array formation using the Hungarian matching algorithm*. Physical Review A **95**, 053424 (2017). (Cited on pages **1** and **40**)

[27] F. Nogrette, H. Labuhn, S. Ravets, D. Barredo, L. Béguin, A. Vernier, T. Lahaye, and A. Browaeys. *Single-Atom Trapping in Holographic 2D Arrays of Microtraps with Arbitrary Geometries*. Physical Review X **4**, 021034 (2014). (Cited on pages **1**, **25**, and **29**)

[28] D. Barredo, V. Lienhard, P. Scholl, S. de Léséleuc, T. Boulier, A. Browaeys, and T. Lahaye. *Three-Dimensional Trapping of Individual Rydberg Atoms in Ponderomotive Bottle Beam Traps*. Physical Review Letters **124**, 023201 (2020). (Cited on pages **1**, **25**, **40**, **80**, and **94**)

[29] H. Sun, Y. Song, and J. Ahn. *Space-variant holographic imaging for 3D Rydberg quantum simulators*. In *Conference on Lasers and Electro-Optics*. OSA (2020). (Cited on pages **1**, **25**, and **40**)

[30] I. S. Madjarov, A. Cooper, A. L. Shaw, J. P. Covey, V. Schkolnik, T. H. Yoon, J. R. Williams, and M. Endres. *An Atomic-Array Optical Clock with Single-Atom Readout*. Physical Review X **9**, 041052 (2019). (Cited on page **1**)

[31] M. A. Norcia, A. W. Young, W. J. Eckner, E. Oelker, J. Ye, and A. M. Kaufman. *Seconds-scale coherence on an optical clock transition in a tweezer array*. Science **366**, 93–97 (2019). (Cited on page **1**)

[32] A. W. Young, W. J. Eckner, W. R. Milner, D. Kedar, M. A. Norcia, E. Oelker, N. Schine, J. Ye, and A. M. Kaufman. *Half-minute-scale atomic coherence and high relative stability in a tweezer clock*. Nature **588**, 408–413 (2020). (Cited on pages **1**, **62**, **65**, **68**, and **107**)

[33] A. Bergschneider, V. M. Klinkhamer, J. H. Becher, R. Klemt, L. Palm, G. Zürn, S. Jochim, and P. M. Preiss. *Experimental characterization of two-particle entanglement through position and momentum correlations*. Nature Physics **15**, 640–644 (2019). (Cited on pages **2** and **25**)

[34] J. Becher, E. Sindici, R. Klemt, S. Jochim, A. Daley, and P. Preiss. *Measurement of Identical Particle Entanglement and the Influence of Antisymmetrization*. Physical Review Letters **125**, 180402 (2020). (Cited on pages **2** and **25**)

[35] B. M. Spar, E. Guardado-Sanchez, S. Chi, Z. Z. Yan, and W. S. Bakr. *A Fermi-Hubbard Optical Tweezer Array*. (2021). (Cited on page **2**)

[36] T. F. Gallagher. *Rydberg Atoms*. Cambridge University Press (1994). ISBN 978-0-521-38531-2 978-0-521-02166-1 978-0-511-52453-0. (Cited on pages **2** and **73**)

[37] A. Browaeys, D. Barredo, and T. Lahaye. *Experimental investigations of*

dipole–dipole interactions between a few Rydberg atoms. Journal of Physics B: Atomic, Molecular and Optical Physics **49**, 152001 (2016). (Cited on pages **2**, **73**, and **74**)

[38] M. D. Lukin, M. Fleischhauer, R. Cote, L. M. Duan, D. Jaksch, J. I. Cirac, and P. Zoller. *Dipole Blockade and Quantum Information Processing in Mesoscopic Atomic Ensembles*. Physical Review Letters **87**, 037901 (2001). (Cited on pages **2** and **74**)

[39] E. Urban, T. A. Johnson, T. Henage, L. Isenhower, D. D. Yavuz, T. G. Walker, and M. Saffman. *Observation of Rydberg blockade between two atoms*. Nature Physics **5**, 110–114 (2009). (Cited on pages **2** and **74**)

[40] A. Gaëtan, Y. Miroshnychenko, T. Wilk, A. Chotia, M. Viteau, D. Comparat, P. Pillet, A. Browaeys, and P. Grangier. *Observation of collective excitation of two individual atoms in the Rydberg blockade regime*. Nature Physics **5**, 115–118 (2009). (Cited on pages **2** and **74**)

[41] H. Bernien, S. Schwartz, A. Keesling, H. Levine, A. Omran, H. Pichler, S. Choi, A. S. Zibrov, M. Endres, M. Greiner, V. Vuletić, and M. D. Lukin. *Probing many-body dynamics on a 51-atom quantum simulator*. Nature **551**, 579–584 (2017). (Cited on pages **2** and **65**)

[42] V. Lienhard, S. de Léséleuc, D. Barredo, T. Lahaye, A. Browaeys, M. Schuler, L.-P. Henry, and A. M. Läuchli. *Observing the Space- and Time-Dependent Growth of Correlations in Dynamically Tuned Synthetic Ising Models with Antiferromagnetic Interactions*. **8**, 021070 (2018). (Cited on page **2**)

[43] V. Lienhard, P. Scholl, S. Weber, D. Barredo, S. de Léséleuc, R. Bai, N. Lang, M. Fleischhauer, H. P. Büchler, T. Lahaye, and A. Browaeys. *Realization of a Density-Dependent Peierls Phase in a Synthetic, Spin-Orbit Coupled Rydberg System*. Physical Review X **10**, 021031 (2020). (Cited on page **2**)

[44] R. Samajdar, W. W. Ho, H. Pichler, M. D. Lukin, and S. Sachdev. *Quantum phases of Rydberg atoms on a kagome lattice*. Proceedings of the National Academy of Sciences **118**, e2015785118 (2021). (Cited on page **2**)

[45] P. Scholl, M. Schuler, H. J. Williams, A. A. Eberharter, D. Barredo, K.-N. Schymik, V. Lienhard, L.-P. Henry, T. C. Lang, T. Lahaye, A. M. Läuchli, and A. Browaeys. *Quantum simulation of 2D antiferromagnets with hundreds of Rydberg atoms*. Nature **595**, 233–238 (2021). (Cited on pages **2** and **106**)

[46] S. de Léséleuc, V. Lienhard, P. Scholl, D. Barredo, S. Weber, N. Lang, H. P. Büchler, T. Lahaye, and A. Browaeys. *Observation of a symmetry-protected topological phase of interacting bosons with Rydberg atoms*. **365**, 775–780 (2019). (Cited on page **2**)

[47] D. Jaksch, J. I. Cirac, P. Zoller, S. L. Rolston, R. Côté, and M. D. Lukin. *Fast Quantum Gates for Neutral Atoms*. Physical Review Letters **85**, 2208–2211 (2000). (Cited on pages **2** and **74**)

[48] M. Saffman and T. G. Walker. *Analysis of a quantum logic device based on*

dipole-dipole interactions of optically trapped Rydberg atoms. Physical Review A **72**, 022347 (2005). (Cited on pages **2**, **74**, and **102**)

[49] T. Wilk, A. Gaëtan, C. Evellin, J. Wolters, Y. Miroshnychenko, P. Grangier, and A. Browaeys. *Entanglement of Two Individual Neutral Atoms Using Rydberg Blockade.* **104**, 010502 (2010). (Cited on page **2**)

[50] M. Saffman, T. G. Walker, and K. Mølmer. *Quantum information with Rydberg atoms.* Reviews of Modern Physics **82**, 2313–2363 (2010). (Cited on pages **2**, **74**, and **90**)

[51] L. Isenhower, M. Saffman, and K. Mølmer. *Multibit C_k NOT quantum gates via Rydberg blockade.* Quantum Information Processing **10**, 755–770 (2011). (Cited on pages **2** and **74**)

[52] W. Lechner, P. Hauke, and P. Zoller. *A quantum annealing architecture with all-to-all connectivity from local interactions.* **1** (2015). (Cited on page **2**)

[53] A. W. Glaetzle, R. M. W. van Bijnen, P. Zoller, and W. Lechner. *A coherent quantum annealer with Rydberg atoms.* Nature Communications **8** (2017). (Cited on pages **2**, **76**, and **108**)

[54] H. Levine, A. Keesling, G. Semeghini, A. Omran, T. T. Wang, S. Ebadi, H. Bernien, M. Greiner, V. Vuletić, H. Pichler, and M. D. Lukin. *Parallel Implementation of High-Fidelity Multiqubit Gates with Neutral Atoms.* Physical Review Letters **123**, 170503 (2019). (Cited on pages **2**, **63**, **80**, and **106**)

[55] I. S. Madjarov, J. P. Covey, A. L. Shaw, J. Choi, A. Kale, A. Cooper, H. Pichler, V. Schkolnik, J. R. Williams, and M. Endres. *High-fidelity entanglement and detection of alkaline-earth Rydberg atoms.* Nature Physics **16**, 857–861 (2020). (Cited on pages **2** and **106**)

[56] T. Keating, R. L. Cook, A. M. Hankin, Y.-Y. Jau, G. W. Biedermann, and I. H. Deutsch. *Robust quantum logic in neutral atoms via adiabatic Rydberg dressing.* Physical Review A **91**, 012337 (2015). (Cited on page **2**)

[57] B. Swingle, G. Bentsen, M. Schleier-Smith, and P. Hayden. *Measuring the scrambling of quantum information.* Physical Review A **94**, 040302 (2016). (Cited on pages **2** and **108**)

[58] J. Zeiher, R. van Bijnen, P. Schauß, S. Hild, J. yoon Choi, T. Pohl, I. Bloch, and C. Gross. *Many-body interferometry of a Rydberg-dressed spin lattice.* Nature Physics **12**, 1095–1099 (2016). (Cited on pages **2**, **63**, **79**, **84**, **98**, and **100**)

[59] J. Zeiher, J. yoon Choi, A. Rubio-Abadal, T. Pohl, R. van Bijnen, I. Bloch, and C. Gross. *Coherent Many-Body Spin Dynamics in a Long-Range Interacting Ising Chain.* Physical Review X **7**, 041063 (2017). (Cited on pages **2**, **63**, **79**, and **84**)

[60] V. Borish, O. Marković, J. Hines, S. Rajagopal, and M. Schleier-Smith. *Transverse-Field Ising Dynamics in a Rydberg-Dressed Atomic Gas.* Physical

Review Letters **124**, 063601 (2020). (Cited on pages **2**, **63**, **79**, **81**, **84**, **101**, and **107**)

[61] Y.-Y. Jau, A. M. Hankin, T. Keating, I. H. Deutsch, and G. W. Biedermann. *Entangling atomic spins with a Rydberg-dressed spin-flip blockade.* Nature Physics **12**, 71–74 (2015). (Cited on pages **2**, **63**, **77**, **79**, and **84**)

[62] N. Lorenz. *A Rydberg tweezer platform with potassium atoms.* PhD thesis, LMU München: Faculty of Physics (2021). (Cited on pages **2**, **7**, **9**, **10**, **13**, **19**, **27**, **45**, **63**, **64**, **66**, **79**, and **83**)

[63] A. W. Glaetzle, M. Dalmonte, R. Nath, C. Gross, I. Bloch, and P. Zoller. *Designing Frustrated Quantum Magnets with Laser-Dressed Rydberg Atoms.* Physical Review Letters **114**, 173002 (2015). (Cited on pages **2**, **76**, and **108**)

[64] M. Duda. *A laser system for cooling and trapping of Potassium-39.* PhD thesis, LMU München: Faculty of Physics (2017). (Cited on pages **7** and **8**)

[65] A.-S. Walter. *Design and characterization of an UV-lasersystem for Rydberg experiments with Potassium* (2018). (Cited on page **7**)

[66] C.-H. Wu. *Strongly interacting quantum mixtures of ultracold atoms.* PhD thesis, Massachusetts Institute of Technology (2013). (Cited on pages **7** and **8**)

[67] C. B. Alcock, V. P. Itkin, and M. K. Horrigan. *Vapour Pressure Equations for the Metallic Elements: 298–2500K.* **23**, 309–313 (1984). (Cited on page **7**)

[68] A. Omran. *A microscope for Fermi gases.* PhD thesis, LMU München: Faculty of Physics (2016). (Cited on page **8**)

[69] T.-L. Chen, S.-Y. Chang, Y.-J. Huang, K. Shukla, Y.-C. Huang, T.-H. Suen, T.-Y. Kuan, J.-T. Shy, and Y.-W. Liu. *Inverted-ladder-type optical excitation of potassium Rydberg states with hot and cold ensembles.* Physical Review A **101**, 052507 (2020). (Cited on pages **10** and **107**)

[70] R. S. Williamson and T. Walker. *Magneto-optical trapping and ultracold collisions of potassium atoms.* Journal of the Optical Society of America B **12**, 1393 (1995). (Cited on page **10**)

[71] M. Landini, S. Roy, L. Carcagní, D. Trypogeorgos, M. Fattori, M. Inguscio, and G. Modugno. *Sub-Doppler laser cooling of potassium atoms.* Physical Review A **84**, 043432 (2011). (Cited on pages **10**, **15**, **36**, and **38**)

[72] G. Salomon, L. Fouché, P. Wang, A. Aspect, P. Bouyer, and T. Bourdel. *Gray-molasses cooling of ^{39}K to a high phase-space density.* EPL (Europhysics Letters) **104**, 63002 (2013). (Cited on pages **10**, **15**, **37**, and **59**)

[73] J. Goodman. *Introduction to Fourier Optics.* WH Freeman (2017). (Cited on page **12**)

[74] L. Beguin. *Measurement of the van der Walls interaction between two Rydberg atoms*. PhD thesis, Istitut d'Optique graduate school (2013). (Cited on page **12**)

[75] S. Hannig, J. Mielke, J. A. Fenske, M. Misera, N. Beev, C. Ospelkaus, and P. O. Schmidt. *A highly stable monolithic enhancement cavity for second harmonic generation in the ultraviolet*. **89**, 013106 (2018). (Cited on page **18**)

[76] T. Preuschoff, M. Schlosser, and G. Birkl. *Digital laser frequency and intensity stabilization based on the STEMlab platform (originally Red Pitaya)*. **91**, 083001 (2020). (Cited on page **18**)

[77] N. Lorenz, L. Festa, L.-M. Steinert, and C. Gross. *Raman sideband cooling in optical tweezer arrays for Rydberg dressing*. SciPost Physics **10** (2021). (Cited on pages **21**, **65**, **67**, **68**, and **70**)

[78] P. Sompet, S. S. Szigeti, E. Schwartz, A. S. Bradley, and M. F. Andersen. *Thermally robust spin correlations between two 85Rb atoms in an optical microtrap*. Nature Communications **10** (2019). (Cited on page **25**)

[79] L. Reynolds, E. Schwartz, U. Ebling, M. Weyland, J. Brand, and M. Andersen. *Direct Measurements of Collisional Dynamics in Cold Atom Triads*. Physical Review Letters **124**, 073401 (2020). (Cited on page **25**)

[80] M. Weyland, S. Szigeti, R. Hobbs, P. Ruksasakchai, L. Sanchez, and M. Andersen. *Pair Correlations and Photoassociation Dynamics of Two Atoms in an Optical Tweezer*. Physical Review Letters **126**, 083401 (2021). (Cited on page **25**)

[81] M. Holten, L. Bayha, K. Subramanian, C. Heintze, P. M. Preiss, and S. Jochim. *Observation of Pauli Crystals*. Physical Review Letters **126**, 020401 (2021). (Cited on page **25**)

[82] N. Schlosser, G. Reymond, and P. Grangier. *Collisional Blockade in Microscopic Optical Dipole Traps*. Physical Review Letters **89**, 023005 (2002). (Cited on pages **25** and **55**)

[83] B. J. Lester, N. Luick, A. M. Kaufman, C. M. Reynolds, and C. A. Regal. *Rapid Production of Uniformly Filled Arrays of Neutral Atoms*. Physical Review Letters **115**, 073003 (2015). (Cited on pages **25**, **55**, **56**, and **61**)

[84] M. Schlosser, S. Tichelmann, J. Kruse, and G. Birkl. *Scalable architecture for quantum information processing with atoms in optical micro-structures*. Quantum Information Processing **10**, 907–924 (2011). (Cited on page **25**)

[85] S. Bergamini, B. Darquié, M. Jones, L. Jacubowiez, A. Browaeys, and P. Grangier. *Holographic generation of microtrap arrays for single atoms by use of a programmable phase modulator*. Journal of the Optical Society of America B **21**, 1889 (2004). (Cited on page **25**)

[86] J. Kruse, C. Gierl, M. Schlosser, and G. Birkl. *Reconfigurable site-selective manipulation of atomic quantum systems in two-dimensional arrays of dipole traps*. Physical Review A **81**, 060308 (2010). (Cited on page **25**)

[87] A. L. Gaunt and Z. Hadzibabic. *Robust Digital Holography For Ultracold Atom Trapping*. Scientific Reports **2** (2012). (Cited on page **25**)

[88] A. L. Gaunt, T. F. Schmidutz, I. Gotlibovych, R. P. Smith, and Z. Hadzibabic. *Bose-Einstein Condensation of Atoms in a Uniform Potential*. Physical Review Letters **110**, 200406 (2013). (Cited on page **25**)

[89] B. Mukherjee, Z. Yan, P. B. Patel, Z. Hadzibabic, T. Yefsah, J. Struck, and M. W. Zwierlein. *Homogeneous Atomic Fermi Gases*. Physical Review Letters **118**, 123401 (2017). (Cited on page **25**)

[90] J. L. Ville, T. Bienaimé, R. Saint-Jalm, L. Corman, M. Aidelsburger, L. Chomaz, K. Kleinlein, D. Perconte, S. Nascimbène, J. Dalibard, and J. Beugnon. *Loading and compression of a single two-dimensional Bose gas in an optical accordion*. Physical Review A **95**, 013632 (2017). (Cited on page **25**)

[91] H. Sun, Y. Song, A. Byun, H. Jeong, and J. Ahn. *Imaging three-dimensional single-atom arrays all at once*. Optics Express **29**, 4082 (2021). (Cited on page **25**)

[92] S. Ebadi, T. T. Wang, H. Levine, A. Keesling, G. Semeghini, A. Omran, D. Bluvstein, R. Samajdar, H. Pichler, W. W. Ho, S. Choi, S. Sachdev, M. Greiner, V. Vuletić, and M. D. Lukin. *Quantum phases of matter on a 256-atom programmable quantum simulator*. Nature **595**, 227–232 (2021). (Cited on pages **25**, **55**, **107**, and **108**)

[93] H. Kim, M. Kim, W. Lee, and J. Ahn. *Gerchberg-Saxton algorithm for fast and efficient atom rearrangement in optical tweezer traps*. Optics Express **27**, 2184 (2019). (Cited on pages **26** and **55**)

[94] P. Osterholz. *Freely Configurable Holographic Trap Arrays for the Trapping of Single Atoms* (2020). (Cited on pages **26**, **28**, **30**, **32**, and **33**)

[95] A. Jesacher, A. Schwaighofer, S. Fürhapter, C. Maurer, S. Bernet, and M. Ritsch-Marte. *Wavefront correction of spatial light modulators using an optical vortex image*. Optics Express **15**, 5801 (2007). (Cited on page **29**)

[96] V. Lakshminarayanan and A. Fleck. *Zernike polynomials: a guide*. **58**, 545–561 (2011). (Cited on page **29**)

[97] N. Matsumoto, T. Inoue, T. Ando, Y. Takiguchi, Y. Ohtake, and H. Toyoda. *High-quality generation of a multispot pattern using a spatial light modulator with adaptive feedback*. Optics Letters **37**, 3135 (2012). (Cited on page **29**)

[98] R. W. Gerchberg and W. O. Saxton. *Practical algorithm for determination of phase from image and diffraction plane pictures*. OPTIK **35**, 237–& (1972). ISSN 0030-4026. (Cited on page **29**)

[99] R. D. Leonardo, F. Ianni, and G. Ruocco. *Computer generation of optimal holograms for optical trap arrays*. Optics Express **15**, 1913 (2007). (Cited on page **31**)

[100] D. Kim, A. Keesling, A. Omran, H. Levine, H. Bernien, M. Greiner, M. D. Lukin, and D. R. Englund. *Large-scale uniform optical focus array generation with a phase spatial light modulator*. Optics Letters **44**, 3178 (2019). (Cited on page **32**)

[101] R. Grimm, M. Weidemüller, and Y. B. Ovchinnikov. *Optical Dipole Traps for Neutral Atoms*. In *Advances In Atomic, Molecular, and Optical Physics*, pages 95–170. Elsevier (2000). (Cited on pages **35** and **52**)

[102] J. D. Thompson, T. G. Tiecke, A. S. Zibrov, V. Vuletić, and M. D. Lukin. *Coherence and Raman Sideband Cooling of a Single Atom in an Optical Tweezer*. Physical Review Letters **110**, 133001 (2013). (Cited on pages **35**, **36**, and **65**)

[103] A. M. Kaufman, B. J. Lester, and C. A. Regal. *Cooling a Single Atom in an Optical Tweezer to Its Quantum Ground State*. Physical Review X **2**, 041014 (2012). (Cited on pages **36** and **65**)

[104] N. R. Hutzler, L. R. Liu, Y. Yu, and K.-K. Ni. *Eliminating light shifts for single atom trapping*. New Journal of Physics **19**, 023007 (2017). (Cited on page **36**)

[105] E. Haller, J. Hudson, A. Kelly, D. A. Cotta, B. Peaudecerf, G. D. Bruce, and S. Kuhr. *Single-atom imaging of fermions in a quantum-gas microscope*. Nature Physics **11**, 738–742 (2015). (Cited on pages **36** and **39**)

[106] A. Neuzner, M. Körber, S. Dürr, G. Rempe, and S. Ritter. *Breakdown of atomic hyperfine coupling in a deep optical-dipole trap*. Physical Review A **92**, 053842 (2015). (Cited on page **36**)

[107] H. J. Metcalf and P. van der Straten. *Laser Cooling and Trapping*. Springer New York (1999). (Cited on page **36**)

[108] T. Walker, D. Sesko, and C. Wieman. *Collective behavior of optically trapped neutral atoms*. Physical Review Letters **64**, 408–411 (1990). (Cited on page **36**)

[109] T. A. Savard, K. M. O'Hara, and J. E. Thomas. *Laser-noise-induced heating in far-off resonance optical traps*. Physical Review A **56**, R1095–R1098 (1997). (Cited on pages **36**, **47**, and **52**)

[110] J. Ang'ong'a, C. Huang, J. P. Covey, and B. Gadway. *Gray molasses cooling of ^{39}K atoms in optical tweezers*. (2021). (Cited on pages **38**, **45**, and **62**)

[111] C. Weitenberg. *Single-Atom Resolved Imaging and Manipulation in an Atomic Mott Insulator*. PhD thesis, LMU München: Faculty of Physics (2011). (Cited on pages **38** and **56**)

[112] G. J. A. Edge, R. Anderson, D. Jervis, D. C. McKay, R. Day, S. Trotzky, and J. H. Thywissen. *Imaging and addressing of individual fermionic atoms in an optical lattice*. Physical Review A **92**, 063406 (2015). (Cited on page **39**)

[113] M. Miranda, R. Inoue, Y. Okuyama, A. Nakamoto, and M. Kozuma. *Site-resolved imaging of ytterbium atoms in a two-dimensional optical lattice.* Physical Review A **91**, 063414 (2015). (Cited on page **39**)

[114] R. Yamamoto, J. Kobayashi, T. Kuno, K. Kato, and Y. Takahashi. *An ytterbium quantum gas microscope with narrow-line laser cooling.* New Journal of Physics **18**, 023016 (2016). (Cited on page **39**)

[115] C. J. Picken, R. Legaie, and J. D. Pritchard. *Single atom imaging with an sCMOS camera.* Applied Physics Letters **111**, 164102 (2017). (Cited on pages **40** and **41**)

[116] A. Bergschneider, V. M. Klinkhamer, J. H. Becher, R. Klemt, G. Zürn, P. M. Preiss, and S. Jochim. *Spin-resolved single-atom imaging of Li6 in free space.* Physical Review A **97**, 063613 (2018). (Cited on pages **40**, **102**, and **108**)

[117] A. Cooper, J. P. Covey, I. S. Madjarov, S. G. Porsev, M. S. Safronova, and M. Endres. *Alkaline-Earth Atoms in Optical Tweezers.* Physical Review X **8**, 041055 (2018). (Cited on pages **40**, **41**, **51**, and **62**)

[118] M. Norcia, A. Young, and A. Kaufman. *Microscopic Control and Detection of Ultracold Strontium in Optical-Tweezer Arrays.* Physical Review X **8**, 041054 (2018). (Cited on pages **40** and **51**)

[119] J. P. Covey, I. S. Madjarov, A. Cooper, and M. Endres. *2000-Times Repeated Imaging of Strontium Atoms in Clock-Magic Tweezer Arrays.* Physical Review Letters **122**, 173201 (2019). (Cited on pages **40** and **41**)

[120] S. Saskin, J. Wilson, B. Grinkemeyer, and J. Thompson. *Narrow-Line Cooling and Imaging of Ytterbium Atoms in an Optical Tweezer Array.* Physical Review Letters **122**, 143002 (2019). (Cited on page **40**)

[121] K. D. Nelson, X. Li, and D. S. Weiss. *Imaging single atoms in a three-dimensional array.* Nature Physics **3**, 556–560 (2007). (Cited on page **40**)

[122] L. Anderegg, L. W. Cheuk, Y. Bao, S. Burchesky, W. Ketterle, K.-K. Ni, and J. M. Doyle. *An optical tweezer array of ultracold molecules.* Science **365**, 1156–1158 (2019). (Cited on page **40**)

[123] K. Barnes, P. Battaglino, B. J. Bloom, K. Cassella, R. Coxe, N. Crisosto, J. P. King, S. S. Kondov, K. Kotru, S. C. Larsen, J. Lauigan, B. J. Lester, M. McDonald, E. Megidish, S. Narayanaswami, C. Nishiguchi, R. Notermans, L. S. Peng, A. Ryou, T.-Y. Wu, and M. Yarwood. *Assembly and coherent control of a register of nuclear spin qubits.* (2021). (Cited on pages **40**, **102**, and **108**)

[124] I. S. Madjarov. *Entangling, controlling, and detecting individualstrontium atoms in optical tweezer arrays.* PhD thesis, Caltech (2021). (Cited on pages **41**, **42**, and **43**)

[125] R. Eberhard. *Preparing next generation tweezer systems for quantum simulation of spin models* (2020). (Cited on pages **44**, **62**, and **108**)

[126] S. de Léséleuc. *Quantum simulation of spin models with assembled arrays of Rydberg atoms*. PhD thesis, Université Paris Saclay (2019). (Cited on page **48**)

[127] L. Rayleigh. *XXV. On copying diffraction-gratings, and on some phenomena connected therewith*. The London, Edinburgh, and Dublin Philosophical Magazine and Journal of Science **11**, 196–205 (1881). (Cited on page **48**)

[128] M. Schlosser, S. Tichelmann, D. Schäffner, D. O. de Mello, M. Hambach, and G. Birkl. *Large-scale multilayer architecture of single-atom arrays with individual addressability*. (2019). (Cited on page **49**)

[129] C. Makrides, D. S. Barker, J. A. Fedchak, J. Scherschligt, S. Eckel, and E. Tiesinga. *Elastic rate coefficients for Li+H2 collisions in the calibration of a cold-atom vacuum standard*. Physical Review A **99**, 042704 (2019). (Cited on page **51**)

[130] P. Micke, J. Stark, S. A. King, T. Leopold, T. Pfeifer, L. Schmöger, M. Schwarz, L. J. Spieß, P. O. Schmidt, and J. R. C. López-Urrutia. *Closed-cycle, low-vibration 4 K cryostat for ion traps and other applications*. Review of Scientific Instruments **90**, 065104 (2019). (Cited on pages **51**, **54**, and **101**)

[131] K.-N. Schymik, S. Pancaldi, F. Nogrette, D. Barredo, J. Paris, A. Browaeys, and T. Lahaye. *Single atoms in optical-tweezers arrays at cryogenic temperatures with 6000-second trapping lifetimes*. (2021). (Cited on pages **51**, **54**, **101**, and **107**)

[132] Y. Wang, K. Wang, E. F. Fenton, Y.-W. Lin, K.-K. Ni, and J. D. Hood. *Reduction of laser intensity noise over 1 MHz band for single atom trapping*. Optics Express **28**, 31209 (2020). (Cited on page **52**)

[133] A. Farré, M. Shayegan, C. López-Quesada, G. A. Blab, M. Montes-Usategui, N. R. Forde, and E. Martín-Badosa. *Positional stability of holographic optical traps*. Optics Express **19**, 21370 (2011). (Cited on page **52**)

[134] D. O. de Mello, D. Schäffner, J. Werkmann, T. Preuschoff, L. Kohfahl, M. Schlosser, and G. Birkl. *Defect-Free Assembly of 2D Clusters of More Than 100 Single-Atom Quantum Systems*. Physical Review Letters **122**, 203601 (2019). (Cited on page **55**)

[135] D. Sesko, T. Walker, C. Monroe, A. Gallagher, and C. Wieman. *Collisional losses from a light-force atom trap*. Physical Review Letters **63**, 961–964 (1989). (Cited on page **55**)

[136] T. Grünzweig, A. Hilliard, M. McGovern, and M. F. Andersen. *Near-deterministic preparation of a single atom in an optical microtrap*. Nature Physics **6**, 951–954 (2010). (Cited on pages **55** and **56**)

[137] M. Brown, T. Thiele, C. Kiehl, T.-W. Hsu, and C. Regal. *Gray-Molasses Optical-Tweezer Loading: Controlling Collisions for Scaling Atom-Array Assembly*. Physical Review X **9**, 011057 (2019). (Cited on pages **55**, **58**, **60**, **61**, **105**, and **108**)

[138] B. Bussery and M. Aubert-Frécon. *Multipolar long-range electrostatic, dispersion, and induction energy terms for the interactions between two identical alkali atoms Li, Na, K, Rb, and Cs in various electronic states.* **82**, 3224–3234 (1985). (Cited on pages **55** and **56**)

[139] J. Weiner, V. S. Bagnato, S. Zilio, and P. S. Julienne. *Experiments and theory in cold and ultracold collisions.* Reviews of Modern Physics **71**, 1–85 (1999). (Cited on page **55**)

[140] K. M. Jones, E. Tiesinga, P. D. Lett, and P. S. Julienne. *Ultracold photoassociation spectroscopy: Long-range molecules and atomic scattering.* Reviews of Modern Physics **78**, 483–535 (2006). (Cited on page **55**)

[141] H. Wang, P. L. Gould, and W. C. Stwalley. *Long-range interaction of the 39K(4s)+39K(4p) asymptote by photoassociative spectroscopy. I. The 0g- pure long-range state and the long-range potential constants.* The Journal of Chemical Physics **106**, 7899–7912 (1997). (Cited on page **56**)

[142] S. Falke, H. Knöckel, J. Friebe, M. Riedmann, E. Tiemann, and C. Lisdat. *Potassium ground-state scattering parameters and Born-Oppenheimer potentials from molecular spectroscopy.* Physical Review A **78**, 012503 (2008). (Cited on page **56**)

[143] P. Julienne. *Cold binary atomic collisions in a light field.* Journal of Research of the National Institute of Standards and Technology **101**, 487 (1996). (Cited on page **56**)

[144] A. Fuhrmanek, R. Bourgain, Y. R. P. Sortais, and A. Browaeys. *Light-assisted collisions between a few cold atoms in a microscopic dipole trap.* Physical Review A **85**, 062708 (2012). (Cited on page **56**)

[145] P. Sompet, A. V. Carpentier, Y. H. Fung, M. McGovern, and M. F. Andersen. *Dynamics of two atoms undergoing light-assisted collisions in an optical microtrap.* Physical Review A **88**, 051401 (2013). (Cited on page **56**)

[146] A. V. Carpentier, Y. H. Fung, P. Sompet, A. J. Hilliard, T. G. Walker, and M. F. Andersen. *Preparation of a single atom in an optical microtrap.* Laser Physics Letters **10**, 125501 (2013). (Cited on page **61**)

[147] M. M. Aliyu, L. Zhao, X. Q. Quek, K. C. Yellapragada, and H. Loh. *D1 magic wavelength tweezers for scaling atom arrays.* (2021). (Cited on page **62**)

[148] M. S. Safronova, U. I. Safronova, and C. W. Clark. *Magic wavelengths for optical cooling and trapping of potassium.* Physical Review A **87**, 052504 (2013). (Cited on page **62**)

[149] D. C. McKay, D. Jervis, D. J. Fine, J. W. Simpson-Porco, G. J. A. Edge, and J. H. Thywissen. *Low-temperature high-density magneto-optical trapping of potassium using the open4S→5Ptransition at 405 nm.* Physical Review A **84**, 063420 (2011). (Cited on page **62**)

[150] T. G. Walker and M. Saffman. *Entanglement of Two Atoms Using Rydberg*

Blockade. In *Advances In Atomic, Molecular, and Optical Physics*, pages 81–115. Elsevier (2012). (Cited on page **63**)

[151] A. Kaufman. *Laser cooling atoms to indistinguishability: Atomic Hong-Ou-Mandel interference and entanglement through spin exchange*. PhD thesis, University of Colorado Boulder (2015). (Cited on pages **63** and **65**)

[152] A. Browaeys and T. Lahaye. *Many-body physics with individually controlled Rydberg atoms*. Nature Physics **16**, 132–142 (2020). (Cited on page **65**)

[153] C. Monroe, D. M. Meekhof, B. E. King, S. R. Jefferts, W. M. Itano, D. J. Wineland, and P. Gould. *Resolved-Sideband Raman Cooling of a Bound Atom to the 3D Zero-Point Energy*. Physical Review Letters **75**, 4011–4014 (1995). (Cited on page **65**)

[154] S. E. Hamann, D. L. Haycock, G. Klose, P. H. Pax, I. H. Deutsch, and P. S. Jessen. *Resolved-Sideband Raman Cooling to the Ground State of an Optical Lattice*. Physical Review Letters **80**, 4149–4152 (1998). (Cited on page **65**)

[155] A. J. Kerman, V. Vuletić, C. Chin, and S. Chu. *Beyond Optical Molasses: 3D Raman Sideband Cooling of Atomic Cesium to High Phase-Space Density*. Physical Review Letters **84**, 439–442 (2000). (Cited on page **65**)

[156] Y. Yu, N. R. Hutzler, J. T. Zhang, L. R. Liu, J. D. Hood, T. Rosenband, and K.-K. Ni. *Motional-ground-state cooling outside the Lamb-Dicke regime*. Physical Review A **97**, 063423 (2018). (Cited on page **65**)

[157] C. Tuchendler, A. M. Lance, A. Browaeys, Y. R. P. Sortais, and P. Grangier. *Energy distribution and cooling of a single atom in an optical tweezer*. Physical Review A **78**, 033425 (2008). (Cited on page **67**)

[158] S. de Léséleuc, D. Barredo, V. Lienhard, A. Browaeys, and T. Lahaye. *Analysis of imperfections in the coherent optical excitation of single atoms to Rydberg states*. Physical Review A **97**, 053803 (2018). (Cited on page **67**)

[159] C. R. C. Cordova. *Quantum liquid droplets in a mixture of Bose-Einstein condensates*. PhD thesis, ICFO - The Institute of Photonic Sciences (2018). (Cited on page **69**)

[160] L. Festa, N. Lorenz, L.-M. Steinert, Z. Chen, P. Osterholz, R. Eberhard, and C. Gross. *Black-body radiation induced facilitated excitation of Rydberg atoms in optical tweezers*. (2021). (Cited on page **73**)

[161] R. Löw, H. Weimer, J. Nipper, J. B. Balewski, B. Butscher, H. P. Büchler, and T. Pfau. *An experimental and theoretical guide to strongly interacting Rydberg gases*. Journal of Physics B: Atomic, Molecular and Optical Physics **45**, 113001 (2012). (Cited on page **74**)

[162] J. Zeiher, P. Schauß, S. Hild, T. Macrì, I. Bloch, and C. Gross. *Microscopic Characterization of Scalable Coherent Rydberg Superatoms*. Physical Review X **5**, 031015 (2015). (Cited on pages **74** and **81**)

[163] H. Labuhn, D. Barredo, S. Ravets, S. de Léséleuc, T. Macrì, T. Lahaye, and A. Browaeys. *Tunable two-dimensional arrays of single Rydberg atoms for realizing quantum Ising models*. Nature **534**, 667–670 (2016). (Cited on page **74**)

[164] P. Schauß, M. Cheneau, M. Endres, T. Fukuhara, S. Hild, A. Omran, T. Pohl, C. Gross, S. Kuhr, and I. Bloch. *Observation of spatially ordered structures in a two-dimensional Rydberg gas*. Nature **491**, 87–91 (2012). (Cited on page **74**)

[165] J. Zeiher. *Realization of Rydberg-dressed quantum magnets*. PhD thesis, LMU München: Faculty of Physics (2017). (Cited on pages **75**, **76**, and **101**)

[166] C. Ates, T. Pohl, T. Pattard, and J. M. Rost. *Antiblockade in Rydberg Excitation of an Ultracold Lattice Gas*. Physical Review Letters **98**, 023002 (2007). (Cited on page **75**)

[167] M. Marcuzzi, J. Minář, D. Barredo, S. de Léséleuc, H. Labuhn, T. Lahaye, A. Browaeys, E. Levi, and I. Lesanovsky. *Facilitation Dynamics and Localization Phenomena in Rydberg Lattice Gases with Position Disorder*. **118**, 063606 (2017). (Cited on page **75**)

[168] M. Gärttner, K. P. Heeg, T. Gasenzer, and J. Evers. *Dynamic formation of Rydberg aggregates at off-resonant excitation*. Physical Review A **88**, 043410 (2013). (Cited on page **76**)

[169] H. Schempp, G. Günter, M. R. de Saint-Vincent, C. S. Hofmann, D. Breyel, A. Komnik, D. W. Schönleber, M. Gärttner, J. Evers, S. Whitlock, and M. Weidemüller. *Full Counting Statistics of Laser Excited Rydberg Aggregates in a One-Dimensional Geometry*. Physical Review Letters **112**, 013002 (2014). (Cited on page **76**)

[170] A. Urvoy, F. Ripka, I. Lesanovsky, D. Booth, J. Shaffer, T. Pfau, and R. Löw. *Strongly Correlated Growth of Rydberg Aggregates in a Vapor Cell*. Physical Review Letters **114**, 203002 (2015). (Cited on page **76**)

[171] C. Carr, R. Ritter, C. G. Wade, C. S. Adams, and K. J. Weatherill. *Nonequilibrium Phase Transition in a Dilute Rydberg Ensemble*. Physical Review Letters **111**, 113901 (2013). (Cited on page **76**)

[172] N. Šibalić, C. G. Wade, C. S. Adams, K. J. Weatherill, and T. Pohl. *Driven-dissipative many-body systems with mixed power-law interactions: Bistabilities and temperature-driven nonequilibrium phase transitions*. Physical Review A **94**, 011401 (2016). (Cited on page **76**)

[173] N. R. de Melo, C. G. Wade, N. Šibalić, J. M. Kondo, C. S. Adams, and K. J. Weatherill. *Intrinsic optical bistability in a strongly driven Rydberg ensemble*. Physical Review A **93**, 063863 (2016). (Cited on page **76**)

[174] F. Letscher, O. Thomas, T. Niederprüm, M. Fleischhauer, and H. Ott. *Bistability Versus Metastability in Driven Dissipative Rydberg Gases*. Physical Review X **7**, 021020 (2017). (Cited on page **76**)

[175] I. Lesanovsky and J. P. Garrahan. *Kinetic Constraints, Hierarchical Relax-*

ation, and Onset of Glassiness in Strongly Interacting and Dissipative Rydberg Gases. Physical Review Letters **111**, 215305 (2013). (Cited on page **76**)

[176] M. M. Valado, C. Simonelli, M. D. Hoogerland, I. Lesanovsky, J. P. Garrahan, E. Arimondo, D. Ciampini, and O. Morsch. *Experimental observation of controllable kinetic constraints in a cold atomic gas*. Physical Review A **93**, 040701 (2016). (Cited on page **76**)

[177] J. E. Johnson and S. L. Rolston. *Interactions between Rydberg-dressed atoms*. Physical Review A **82**, 033412 (2010). (Cited on page **76**)

[178] R. van Bijnen and T. Pohl. *Quantum Magnetism and Topological Ordering via Rydberg Dressing near Förster Resonances*. Physical Review Letters **114**, 243002 (2015). (Cited on page **76**)

[179] G. Pupillo, A. Micheli, M. Boninsegni, I. Lesanovsky, and P. Zoller. *Strongly Correlated Gases of Rydberg-Dressed Atoms: Quantum and Classical Dynamics*. Physical Review Letters **104**, 223002 (2010). (Cited on page **76**)

[180] N. Henkel, R. Nath, and T. Pohl. *Three-Dimensional Roton Excitations and Supersolid Formation in Rydberg-Excited Bose-Einstein Condensates*. Physical Review Letters **104**, 195302 (2010). (Cited on page **76**)

[181] N. Henkel, F. Cinti, P. Jain, G. Pupillo, and T. Pohl. *Supersolid Vortex Crystals in Rydberg-Dressed Bose-Einstein Condensates*. Physical Review Letters **108**, 265301 (2012). (Cited on page **76**)

[182] F. Cinti, T. Macrì, W. Lechner, G. Pupillo, and T. Pohl. *Defect-induced supersolidity with soft-core bosons*. Nature Communications **5** (2014). (Cited on page **76**)

[183] A. Geißler, I. Vasić, and W. Hofstetter. *Condensation versus long-range interaction: Competing quantum phases in bosonic optical lattice systems at near-resonant Rydberg dressing*. Physical Review A **95**, 063608 (2017). (Cited on page **76**)

[184] A. Mitra, M. J. Martin, G. W. Biedermann, A. M. Marino, P. M. Poggi, and I. H. Deutsch. *Robust Mølmer-Sørensen gate for neutral atoms using rapid adiabatic Rydberg dressing*. Physical Review A **101**, 030301 (2020). (Cited on page **77**)

[185] R. Mukherjee, T. C. Killian, and K. R. A. Hazzard. *Accessing Rydberg-dressed interactions using many-body Ramsey dynamics*. Physical Review A **94**, 053422 (2016). (Cited on page **79**)

[186] E. Guardado-Sanchez, B. M. Spar, P. Schauss, R. Belyansky, J. T. Young, P. Bienias, A. V. Gorshkov, T. Iadecola, and W. S. Bakr. *Quench Dynamics of a Fermi Gas with Strong Nonlocal Interactions*. Physical Review X **11**, 021036 (2021). (Cited on pages **79**, **84**, and **107**)

[187] F. Riehle. *Frequency Standards*. Wiley (2003). (Cited on page **79**)

[188] X. Baillard, A. Gauguet, S. Bize, P. Lemonde, P. Laurent, A. Clairon, and P. Rosenbusch. *Interference-filter-stabilized external-cavity diode lasers*. Optics Communications **266**, 609–613 (2006). (Cited on page **79**)

[189] J. Alnis, A. Matveev, N. Kolachevsky, T. Udem, and T. W. Hänsch. *Subhertz linewidth diode lasers by stabilization to vibrationally and thermally compensated ultralow-expansion glass Fabry-Pérot cavities*. Physical Review A **77**, 053809 (2008). (Cited on page **80**)

[190] A. N. Matveev, N. N. Kolachevsky, J. Alnis, and T. W. Hänsch. *Semiconductor laser with the subhertz linewidth*. Quantum Electronics **38**, 895–902 (2008). (Cited on page **80**)

[191] A. N. Matveev, N. N. Kolachevsky, J. Alnis, and T. W. Hänsch. *Spectral parameters of reference-cavity-stabilised lasers*. Quantum Electronics **38**, 391–400 (2008). (Cited on page **80**)

[192] J. Alnis, A. Matveev, N. Kolachevsky, T. Wilken, R. Holzwarth, and T. W. Hänsch. *Stable diode lasers for hydrogen precision spectroscopy*. The European Physical Journal Special Topics **163**, 89–94 (2008). (Cited on page **80**)

[193] E. Goldschmidt, T. Boulier, R. Brown, S. Koller, J. Young, A. Gorshkov, S. Rolston, and J. Porto. *Anomalous Broadening in Driven Dissipative Rydberg Systems*. Physical Review Letters **116**, 113001 (2016). (Cited on page **84**)

[194] J. A. Aman, B. J. DeSalvo, F. B. Dunning, T. C. Killian, S. Yoshida, and J. Burgdörfer. *Trap losses induced by near-resonant Rydberg dressing of cold atomic gases*. Physical Review A **93**, 043425 (2016). (Cited on page **84**)

[195] B. J. DeSalvo, J. A. Aman, C. Gaul, T. Pohl, S. Yoshida, J. Burgdörfer, K. R. A. Hazzard, F. B. Dunning, and T. C. Killian. *Rydberg-blockade effects in Autler-Townes spectra of ultracold strontium*. Physical Review A **93**, 022709 (2016). (Cited on page **84**)

[196] C. Gaul, B. DeSalvo, J. Aman, F. Dunning, T. Killian, and T. Pohl. *Resonant Rydberg Dressing of Alkaline-Earth Atoms via Electromagnetically Induced Transparency*. Physical Review Letters **116**, 243001 (2016). (Cited on page **84**)

[197] J. de Hond, N. Cisternas, R. J. C. Spreeuw, H. B. van Linden van den Heuvell, and N. J. van Druten. *Interplay between van der Waals and dipole–dipole interactions among Rydberg atoms*. Journal of Physics B: Atomic, Molecular and Optical Physics **53**, 084007 (2020). (Cited on page **84**)

[198] T. Boulier, E. Magnan, C. Bracamontes, J. Maslek, E. A. Goldschmidt, J. T. Young, A. V. Gorshkov, S. L. Rolston, and J. V. Porto. *Spontaneous avalanche dephasing in large Rydberg ensembles*. Physical Review A **96**, 053409 (2017). (Cited on page **84**)

[199] J. T. Young, T. Boulier, E. Magnan, E. A. Goldschmidt, R. M. Wilson, S. L. Rolston, J. V. Porto, and A. V. Gorshkov. *Dissipation-induced dipole blockade and antiblockade in driven Rydberg systems*. Physical Review A **97**, 023424 (2018). (Cited on page **84**)

[200] I. I. Beterov, I. I. Ryabtsev, D. B. Tretyakov, and V. M. Entin. *Quasiclassical calculations of blackbody-radiation-induced depopulation rates and effective lifetimes of RydbergnS,nP, andnDalkali-metal atoms withn≤80.* Physical Review A **79,** 052504 (2009). (Cited on page **85**)

[201] W. E. Cooke and T. F. Gallagher. *Effects of blackbody radiation on highly excited atoms.* Physical Review A **21,** 588–593 (1980). (Cited on page **85**)

[202] W. P. Spencer, A. G. Vaidyanathan, D. Kleppner, and T. W. Ducas. *Temperature dependence of blackbody-radiation-induced transfer among highly excited states of sodium.* Physical Review A **25,** 380–384 (1982). (Cited on page **85**)

[203] T. F. Gallagher and W. E. Cooke. *Interactions of Blackbody Radiation with Atoms.* Physical Review Letters **42,** 835–839 (1979). (Cited on page **85**)

[204] N. Šibalić, J. Pritchard, C. Adams, and K. Weatherill. *ARC: An open-source library for calculating properties of alkali Rydberg atoms.* Computer Physics Communications **220,** 319–331 (2017). (Cited on pages **86** and **88**)

[205] S. Weber, C. Tresp, H. Menke, A. Urvoy, O. Firstenberg, H. P. Büchler, and S. Hofferberth. *Calculation of Rydberg interaction potentials.* Journal of Physics B: Atomic, Molecular and Optical Physics **50,** 133001 (2017). (Cited on pages **88**, **89**, and **90**)

[206] D. Weller, A. Urvoy, A. Rico, R. Löw, and H. Kübler. *Charge-induced optical bistability in thermal Rydberg vapor.* Physical Review A **94,** 063820 (2016). (Cited on page **89**)

[207] A. D. Bounds, N. C. Jackson, R. K. Hanley, E. M. Bridge, P. Huillery, and M. P. A. Jones. *Coulomb anti-blockade in a Rydberg gas.* New Journal of Physics **21,** 053026 (2019). (Cited on page **89**)

[208] M. L. Zimmerman, M. G. Littman, M. M. Kash, and D. Kleppner. *Stark structure of the Rydberg states of alkali-metal atoms.* Physical Review A **20,** 2251–2275 (1979). (Cited on page **90**)

[209] J. Tallant, D. Booth, and J. P. Shaffer. *Photoionization rates of Cs Rydberg atoms in a 1064-nm far-off-resonance trap.* Physical Review A **82,** 063406 (2010). (Cited on page **90**)

[210] R. M. Potvliege and C. S. Adams. *Photo-ionization in far-off-resonance optical lattices.* New Journal of Physics **8,** 163–163 (2006). (Cited on page **90**)

[211] S. E. Anderson, K. C. Younge, and G. Raithel. *Trapping Rydberg Atoms in an Optical Lattice.* Physical Review Letters **107,** 263001 (2011). (Cited on page **94**)

[212] N. Thaicharoen, S. A. Miller, and G. Raithel. *Expansion behavior and pair correlations in continuously excited Rydberg systems.* Physical Review A **98,** 023402 (2018). (Cited on page **100**)

[213] L. Li, Y. O. Dudin, and A. Kuzmich. *Entanglement between light and an optical atomic excitation.* Nature **498,** 466–469 (2013). (Cited on page **102**)

[214] J. Adema. *A low noise Laser system for high fidelity Rydberg atom manipulation* (2019). (Cited on page **106**)

[215] K.-N. Schymik, V. Lienhard, D. Barredo, P. Scholl, H. Williams, A. Browaeys, and T. Lahaye. *Enhanced atom-by-atom assembly of arbitrary tweezer arrays*. Physical Review A **102**, 063107 (2020). (Cited on page **108**)

[216] B. Efron and R. Tibshirani. *An Introduction to the Bootstrap*. Chapman and Hall/CRC (1994). (Cited on page **109**)

[217] J. L. Rodgers. *The Bootstrap, the Jackknife, and the Randomization Test: A Sampling Taxonomy*. **34**, 441–456 (1999). (Cited on page **109**)

Acknowledgments

I like to thank all the people that have been part of my life in these years as a PhD student, for the help and support that they gave me or only for the time that we have spent together.

I want to thank Professor Immanuel Bloch for the opportunity to do my PhD studies in his group in this exciting field of research.

My gratitude and thanks goes to Christian for the opportunity to work on this new experiment. Thank you for your support, the constructive discussions, your energetic curiosity towards physics and the hands-on approach to the problems that made possible the realization of the experiment.

I want to thank the members of the Potassium lab: Nikolaus Lorenz with which I started together the construction of the this nice experiment, Vielen Dank!

Marcel Duda for the good time in the laboratory.

Lea for her support in the laboratory, positive vibes and good working energy, thank you!

Thank you and good luck to the new generation of PhD students Robin and Philip. And also thank you to all the people that worked in the lab over the years Zaijun, Jens, Anne-Sophie, Sarah, Joop, Rebecca, Ina, Florian and Anton.

A special thank you goes to Anton Mayer for his patience and help in the design and construction of the experimental setup with countless technical solutions.

Thank you to the team in the MPQ workshop.

Many thanks to Karsten for all the insight regarding all the electronics related problems and the development of new solutions.

Thank you Olivia for the production of the electronics needed to run the experiment.

I want to thank also Kristina, Doreen and Ildiko for the efficient administrative support and the patience that they have with us.

I would like to thank all the members of the Bloch group for the discussions, the journal clubs and the sharing of laboratory equipment. In particular I want to thanks a few that I met over the year Antonio Rubio, Annie Jihyun Park, Jayadev Vijayan, Johannes Zeiher, Simon Hollerith, Andre Heinz, Joannis Koepsel, Monika Aidelsburger, Pranjal Bordia and Giulio Pasqualetti.

I want to thank for critical reading of the thesis and Jayadev Vijayan, Lea, Robin and Christian Gross.

Of course I am very grateful to my family and specially to my parent for the continuous support and the possibility to rely on them. I thank also my in-laws for their support and help.

Finally, I like to thank my wife Dalila for her support, patience with me and your push to do more. Thank you for all the years that we have and will spend together!